International Journal of

Thermodynamics

Editor-in-Chief
L. Kuddusi

Honorary Editors
A. Bejan
M. J. Moran
J. Szargut
G. Tsatsaronis
A. Valero
M. R. von Spakovsky

International Centre for Applied Thermodynamics

CONTENTS

Research article

Dissociation Constant Studies of 2-Substituted 4-Formylbenzoic Acid based on Conductometric Parameters using Fuoss-Hsia Theories

[1]K. N. Kaka ⓘD , [1]S. G. Taher ⓘD , [1]W. M. Hamad ⓘD , [2*]R. A. Omer ⓘD

[1,2]Koya University, Faculty of Science & Health, Department of Chemistry, Koya KOY45, Kurdistan Region – F.R., Iraq
E-mail: [2*]rebaz.anwar@koyauniversity.org

Abstract

The dissociation constant is a quantitative measure of the strength of an acid in solution. This study examines dissociation constant for the series substituted acids like Ortho-alkoxy-4-formylbenzoic acid. The use of (2-methoxy ethanol) as a solvent contributed to the study expected to form free ions or solvent separated ion pair which has been studied with the use conductometric method at different temperatures ranged from 293.15 to 318.15K. The study aims at figuring out dissociation constant, equivalent conductance at infinity dilution, and Walden product by minimization technique using Fuoss-Hsia for both (Modified and Complete) equations. It has been found in the results that the calculated values based on statistical sum square (different between practical and theoretical values) is equivalent conductance at infinity dilution and dissociation constant. It has also been observed that increase the temperature leads to the increase of the molar conductance at infinity dilution, and the increase in association. Moreover, the substituted alkoxy group also affected dissociation of compounds. In this study, the thermodynamic parameters (ΔH^o, ΔG^o and ΔS^o) have also been evaluated and discussed. Finally, the effect of substituent groups on rate of dissociation was studied and explained with agreement to the principles of mesomeric(M) and Inductive effect(I) of substituent groups on dissociation constant.

Keywords: *Conductometric; dissociation constant; fuoss-Hsia theories; minimization technique; thermodynamic parameters.*

1. Introduction

Many studies on thermodynamics and dissociation constant have been conducted in connection with conductometry with the use of many equations [1-6]. Friedrich Kohlrausch (1840–1910), a German chemist, initially proposed the Kohlrausch equation as the outcome of extensive experimental effort.

$$\Lambda = \Lambda_0 - K\sqrt{C} \qquad (1)$$

where Λ is the molar conductance, Λ_0 is molar conductance in the limit of zero concentration when the ions do not interact with each other, K is a coefficient related to the stoichiometry of the electrolyte, and C is the concentration of the electrolyte [7]. The inductive effect of the substituent is transmitted to the carboxyl group in two rather different ways. Most frequently, the substituent is regarded as causing shifts in the average distributions of the bonding electrons along the chain of atoms in the carboxyl proton. This produces a succession of electron shifts along the chain of atoms which leads to electron-attracting substituent that increases the acid strength by making it more energetically feasible for the –OH [8]. The equations:

$$\Lambda = \Lambda_0 - S\sqrt{C} + E' c\ln c + Jc - K_A\Lambda_{0c} \qquad (2)$$

Can be used to calculate dissociation constant

$$(K_d = 1/K_A) \qquad . \qquad (3)$$

where Λ, Λ_0 are equivalent conductance, equivalent conductance at infinity dilutions respectively, E' is constant factor, Jc is a term from long-range interaction and $K_A\Lambda_{0c}$ term from pair formation near in concentration (c)[9].

According to Arrhenius's original definition, an acid is a substance that dissociates in aqueous solution, releasing the hydrogen ion H^+ (a proton):

$$[HA \rightleftharpoons A^- + H^+] \qquad (4)$$

The equilibrium constant for this dissociation reaction is known as dissociation constant [10-12]. The stability of substitution in 4- position of benzoic acid, and stability of the mentioned compound at different solvent was estimated [13, 14]. The conductometric study of benzoic acid has been studied with the use of many equations for finding dissociation constant, thermodynamic parameters and equivalent conductance at infinity dilution [15, 16]. The other studies show that the temperature, type of electrolytes, solvents and conductometric equations play an important role in shaping conductometric curve at different solvents [17, 18]. The study of dissociation constant with thermodynamic parameters in a mixture solvent illustrates that the increase of pK values causes solvation stabilization of a proton greater than others [19]. The molar conductance

at infinity dilution(Λ_o), dissociation constants (Kd) were determined with using theoretical conductance equations of the complete and modified forms of Fuoss-Hsia [20-22].

2. Materials and Methods

The measurements are made at a range of temperature between 283.15-318.15K with the instrument named OKATON conductometer type CON 510 BENCHTOP METER audio frequency, and all the stock solutions are prepared by weight and measurements with the manipulation of the weight dilution technique. The Table 1 shows the experimental conductance for compounds 1, 2, 3 and 4 (Aladdin). The instrument accuracy for conductivity measurements is about ±0.05%. The cell constant (as determined by standard solutions of purified potassium chloride (Sigma-Aldrich)) is 0.9993. The method used for measuring cell constant and conductance has been described in [23]. The compounds 1, 2, 3 and 4 in (Figure 1) that is used in this study is prepared by Sigma-Aldrich Company. This study aims at finding dissociation constant of weak electrolytes 1, 2 and 3 compared with compound number 4. Then it extends to estimate thermodynamics parameters to prove the interaction between the ion and solvent to produce ion pair or solvent separate ion pair consequently conductometric study results in finding Walden product depending on the increase of temperature and viscosity, and this attributes to the dielectric friction constant for the compounds with viscosity, the high viscosity showed the low value of conductivity.

2.1 Computational Study

Example of minimization program (Figure 2). In the present work, all program was written in Fortran power station 4, worked under windows 10, used to minimize the measure conductance data which is fed in as N pair of C_i/Λ_i values, the best fitted values of the two parameters K_A ($K_A=1/K_d$) and Λ_o which are usually obtained as follows: K_A runs from an initial value of KA to KMAX in steps of DKA and Λ_o runs from an initial value of L0 to L0MAX in steps of DL0, with

respect to complete Fuoss-Hsia (Fuoss and Hsia, 1967) given as an example here, and the input is needed in the following order: ETA (Viscosity of solvent), D (Dielectrical constant of solvent), T (absolute temperature) Z (valency of electrolyte), L0 (Initial $\Lambda_{o\ value)}$, K_A (Initial K_A value), N (C_i/Λ_i pair numbers) and C(I, J) (N pairs of C and Λ data). The output consists of the sum square S^2, between calculated and measured conductances and the corresponding values of KA, Λ_o.

3. Results and Discussion

This work aims at examining the dissociation Constant of Some Ortho Substituted 4-Formylbenzoic Acid (where substituted are: $-OCH_3$, OCH_2CH_3, $-OCH_2CH_2CH_3$, $-OH$) Compounds based on Conductometric Parameters which is calculated with the use of Fuoss-Hsia Theories of both modified and complete at different temperatures. Molar conductance was measured, and it has been foundthat corresponding concentration in mol.dm^{-3} that the temperature ranges between 283.15-318.15K, as it is given in Table 1. The interpretation of the characteristic parameters of a weak electrolyte solution from conductance data using minimization technique is adopted to find dissociation constant (Kd), Molar conductance at infinity dilution (Λ_o).

For the data analysis, this study draws on C_i (Concentration), Λi (equivalent conductance) (i=1, 2,..,N) with the use of a Fortran power station-4X- computer program. The output results of minimization technique for the best fit values of the three parameters: K_d, Λ_o depending on sum square (S^2), standard deviation (σ) and Walden product as they are listed in Tables (2, 3, 4 and 5). In Figures (3, 4, 5 and 6), are curves of molar conductance versus square root of concentration at different temperature ranges between 283.15-318.15 K for these electrolytes. The measured Λ_0, K_d was obtained from Minimization technique, the temperature effect on the solvent solute interaction is shown in Table 1, as the temperature increased the molar conductance increased of at interval.
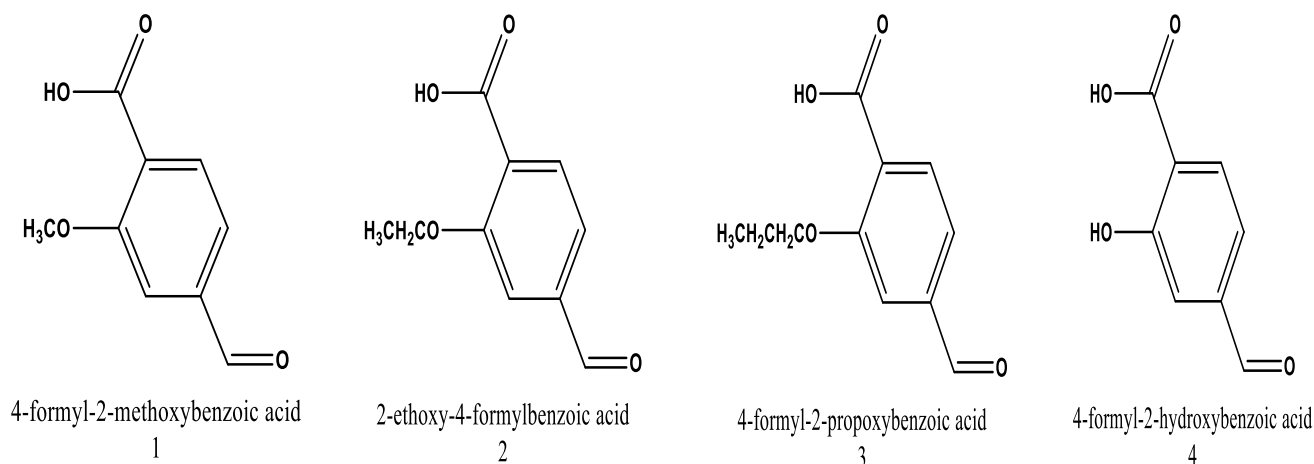

4-formyl-2-methoxybenzoic acid
1

2-ethoxy-4-formylbenzoic acid
2

4-formyl-2-propoxybenzoic acid
3

4-formyl-2-hydroxybenzoic acid
4

Figure 1. Structure of compounds under study.

```
PROGRAM ACH1
DOUBLE PRECISION SS,FREQ,H,X,R2,G1,G,E1,Y,BO,DL,P1,P2
DOUBLE PRECISION KAMAX,DOCL(50),P3,T0,F11,F12,F13,F14
DOUBLE PRECISION L0MAX,          AR(50),CL(50,2),L(50)
DOUBLE PRECISION KA,L0,LCALC,NAV,KAP,KAPA,N12,N21,KD
DOUBLE PRECISION FACT1,FACT2,TT1,TT2,F21,F1,F2,DX,S2
DOUBLE PRECISION ETA,D,T,B,DL0,DKA,Z
INTEGER A
DO 1211 IMG=1,5
READ (IMG,*)ETA,D,T
JMG=IMG+5
WRITE(JMG,1050)ETA,D,T
1050 FORMAT(1H,3(5X,D14.6))
2 READ(IMG,*)Z,L0,KA,DL0,DKA
READ(IMG,*)L0MAX,KAMAX
WRITE(JMG,1100)Z,L0,KA,DL0,DKA,L0MAX,KAMAX
1100 FORMAT(1H,3(2X,D14.6))
KD=1.0D0/KA
N12=L0
N21=KA
SS=0.0D0
3 READ(IMG,*)FREQ
IF(FREQ.EQ.5)GO TO 2
READ(IMG,*)M,N
WRITE(JMG,666)M,N
666 FORMAT(1H,3HM =,I6,3HN =,I6)
DO 400 A=1,M
READ(IMG,*)AR(A)
400 CONTINUE
DO 401 I=1,N
DO 401 J=1,2
READ(IMG,*)CL(I,J)
401 WRITE(JMG,1200)CL(I,J)
1200 FORMAT(1H,10X,D14.6)
WRITE(JMG,500)
500 FORMAT(1H,10X,8HTE SALTS)
WRITE(JMG,501)
501 FORMAT(1H,10X,21HCOMPLETE % FUOSS HISA)
WRITE(JMG,502)FREQ
502 FORMAT(1H,10X, 6HFREQ =,D14.6)
4 DO 402 A=1,M
H=1.0D0
NAV=123456.0D0
WRITE(JMG,503)KA,A,AR(A)
503 FORMAT(1H,3HKA=,D16.6,2HAR,I2,1H=,D16.8)
5 H=1.0D0
DO 403 I=1,N
GO TO 6
7 H=G
6 FACT1=-2.303D0*0.5092D0*Z**3*DSQRT(CL(I,1)*H)
FACT2=1.0D0+0.3286D0*AR(A)*Z*DSQRT(CL(I,1)*H)
FACT=DEXP(FACT1/FACT2)
X=DEXP(-DSQRT(6.66D05*CL(I,1)*H*Z**6/D**3))
R2=DSQRT(KD**2+4.0D0*CL(I,1)*FACT**2*KD)-KD
IF(R2.LT..0D0)WRITE(JMG,504)
504 FORMAT(1H,5HR2NEG)
G1=DSQRT(KD**2+4.0D0*CL(I,1)*X**2*KD)-KD
G=G1/(2.0D0*CL(I,1)*X*X)
IF(DABS(G-H).GT.0.0001D0)GO TO 7
R2=1.0D0/DSQRT(2.0D0)
H=1.0D0
KAP=DSQRT(CL(I,1)*G)*Z*2.913D0*1.0D08/DSQRT(D)
E1=Z**6*1.11D0*1.0D05/D**3
KAPA=KAP*AR(A)*1.0D-08
Y=0.0D0
```

Continued…

Figure 2. Fuoss Hsia program for finding Kd.

Table 1. Experimental conductance data for compounds.

conc. M	Temp. K	Molar Conductance (Λ) mol^{-1} cm^2 ohm^{-1}			
		Compound 1	Compound 2	Compound 3	Compound 4
0.0030	283.15	0.917	0.577	0.517	0.280
	288.15	1.012	0.677	0.593	0.347
	293.15	1.230	0.787	0.627	0.447
	298.15	1.250	0.833	0.680	0.503
	303.15	1.400	1.030	0.713	0.663
	308.15	1.483	1.123	0.807	0.720
	313.15	1.850	1.167	1.033	0.817
	318.15	1.917	1.477	1.117	0.980
0.0015	283.15	1.220	0.620	0.553	0.287
	288.15	1.282	0.787	0.720	0.387
	293.15	1.353	0.933	0.893	0.473
	298.15	1.467	1.000	0.920	0.527
	303.15	1.613	1.160	0.947	0.793
	308.15	1.700	1.380	0.990	0.947
	313.15	2.000	1.533	1.100	1.067
	318.15	2.212	1.730	1.167	1.103
0.0008	283.15	1.270	0.667	0.587	0.467
	288.15	1.372	0.840	0.760	0.607
	293.15	1.470	1.067	0.960	0.693
	298.15	1.747	1.333	1.147	0.800
	303.15	1.920	1.520	1.213	1.120
	308.15	2.227	1.693	1.333	1.293
	313.15	2.400	2.133	1.467	1.403
	318.15	2.520	2.200	1.667	1.633
0.0004	283.15	1.523	0.880	0.683	0.587
	288.15	2.347	1.013	0.880	0.720
	293.15	2.573	1.173	1.073	0.800
	298.15	3.013	1.600	1.280	0.960
	303.15	3.467	1.840	1.340	1.307
	308.15	3.653	2.133	1.547	1.407
	313.15	3.733	2.533	1.680	1.593
	318.15	3.920	2.720	1.973	1.867
0.0002	283.15	1.607	0.963	0.695	0.607
	288.15	2.667	1.027	0.963	0.767
	293.15	2.855	1.235	1.103	0.833
	298.15	3.497	1.865	1.390	0.997
	303.15	3.849	1.998	1.497	1.333
	308.15	4.016	2.303	1.711	1.633
	313.15	4.230	2.763	1.925	1.700
	318.15	4.385	2.941	2.096	2.000

Table 2. Best fit results for compound-1.

Temp. K	Fuoss-Hsia Modified					Fuoss-Hsia Complete				
	K_d /10^{-4}	Λ_o	S^2	σ	Walden Product	K_d /10^{-4}	Λ_o	S^2	σ	Walden Product
283.15	2.222	1.0	0.05	0.014142	2.182	2.381	1.23	0.45	0.304056	2.68386
288.15	1.587	1.3	0.04	0.021213	2.5467	1.923	1.40	0.32	0.39598	2.7426
293.15	1.190	1.9	0.03	0.028284	3.3611	1.408	2.0	0.27	0.431335	3.538
298.15	0.909	2.0	0.02	0.035355	3.214	1.111	2.3	0.07	0.572756	3.6961
303.15	0.714	2.7	0.01	0.042426	3.9663	0.909	3.3	0.17	0.502046	4.8477
308.15	0.606	3.0	0.05	0.014142	4.023	0.800	4.0	0.88	0	5.364
313.15	0.508	4.7	0.02	0.035355	5.7904	0.667	4.5	0.33	0.388909	6.0368
318.15	0.357	6.0	0.07	0	6.822	0.556	7.0	0.07	0.572756	7.959

Table 3. Best fit results for compound-2.

Temp. K	Fuoss-Hsia Modified					Fuoss-Hsia Complete				
	K_d /10^{-5}	Λ_o	S^2	σ	Walden Product	K_d /10^{-5}	Λ_o	S^2	σ	Walden Product
283.15	0.649	1.1000	0.24	0.141421	2.4002	2.273	1.3000	0.22	0.438406	2.8366
288.15	0.556	1.3000	0.16	0.19799	2.5467	2.128	1.4000	0.17	0.473762	2.7426
293.15	0.417	1.4000	0.08	0.254558	2.4766	1.961	1.7000	0.84	0	3.0073
298.15	0.333	1.7000	0.44	0	2.7319	1.802	1.9000	0.57	0.190919	3.0533
303.15	0.286	1.8000	0.21	0.162635	2.6442	1.695	2.0000	0.38	0.325269	2.938
308.15	0.250	4.0000	0.24	0.141421	5.364	1.613	4.2000	0.75	0.06364	5.6322
313.15	0.218	5.0000	0.17	0.190919	6.16	1.538	5.3000	0.16	0.480833	6.5296
318.15	0.185	7.0000	0.04	0.282843	7.959	1.449	8.8000	0.26	0.410122	10.0056

Table 4. Best fit results for compound-3.

Temp. K	Fuoss-Hsia Modified					Fuoss-Hsia Complete				
	K_d /10^{-6}	Λ_o	S^2	σ	Walden Product	K_d /10^{-6}	Λ_o	S^2	σ	Walden Product
283.15	0.385	1.3000	0.1300	0.537401	2.8366	0.508	1.5000	0.1100	0.360624	3.273
288.15	0.370	2.0000	0.5400	0.247487	3.918	0.485	2.4000	0.6200	0	4.7016
293.15	0.351	2.6000	0.0100	0.622254	4.5994	0.452	3.2000	0.4000	0.155563	5.6608
298.15	0.333	3.0000	0.2000	0.487904	4.821	0.432	3.6000	0.3000	0.226274	5.7852
303.15	0.318	3.5000	0.8900	0	5.1415	0.419	4.4000	0.2100	0.289914	6.4636
308.15	0.305	4.0000	0.1400	0.53033	5.364	0.403	5.0000	0.4800	0.098995	6.705

Continued

| 313. 15 | 0.294 | 6.6000 | 0.1200 | 0.544472 | 8.1312 | 0.390 | 7.2000 | 0.1100 | 0.360624 | 8.8704 |
| 318.15 | 0.286 | 9.7000 | 0.1100 | 0.551543 | 11.0289 | 0.378 | 10.2000 | 0.3000 | 0.226274 | 11.5974 |

Table 5. Best fit results for compound-4.

	Fuoss-Hsia Modified					Fuoss-Hsia Complete				
Temp. K	K_d /10^{-3}	Λ_o	S^2	σ	Walden Product	K_d /10^{-3}	Λ_o	S^2	σ	Walden Product
283.15	0.244	1.5000	0.0200	0.388909	1.09	1.670	1.8000	0.0030	0.358503	2.18
288.15	0.200	2.2000	0.1000	0.33234	1.18	1.250	2.7000	0.1000	0.289914	7.84
293.15	0.161	3.0000	0.0500	0.367696	1.42	0.950	3.8000	0.0400	0.33234	8.85
298.15	0.122	3.5000	0.5000	0.049497	1.61	0.769	4.5000	0.0900	0.296985	11.20
303.15	0.099	4.1000	0.1800	0.275772	1.62	0.625	5.0000	0.1100	0.282843	11.80
308.15	0.070	6.8000	0.2900	0.19799	1.88	0.500	7.8000	0.2600	0.176777	12.10
313.15	0.050	7.2000	0.5700	0	2.3	0.400	8.5000	0.5100	0	12.30
318.15	0.043	9.8000	0.1000	0.33234	11.0	0.333	11.1000	0.1000	0.289914	14.80

Figure 3. Molar conductance vs square root of concentration for compound 1 at different temperature.
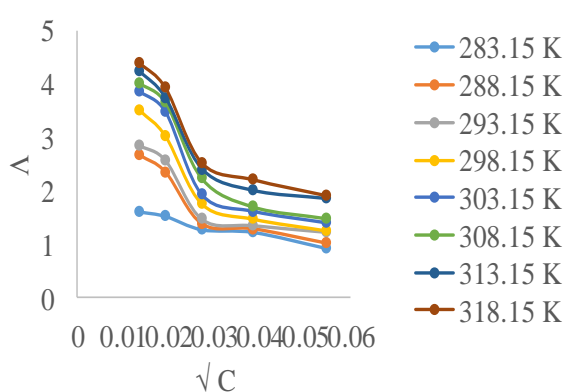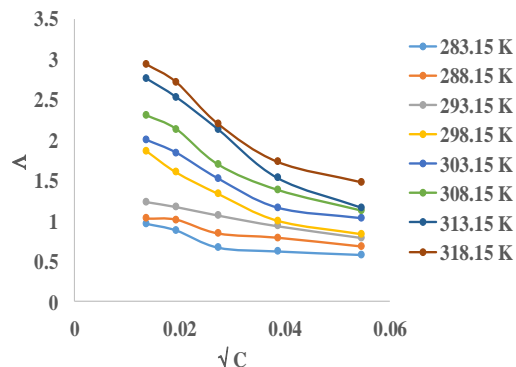

Figure 4. Molar conductance vs square root of concentration for compound 2 at different temperature.
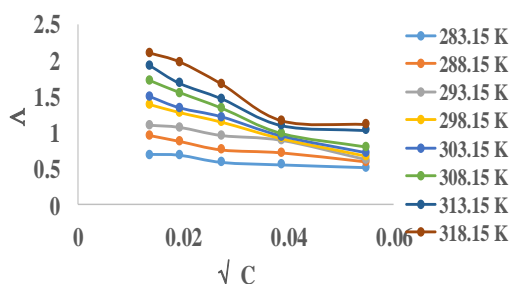

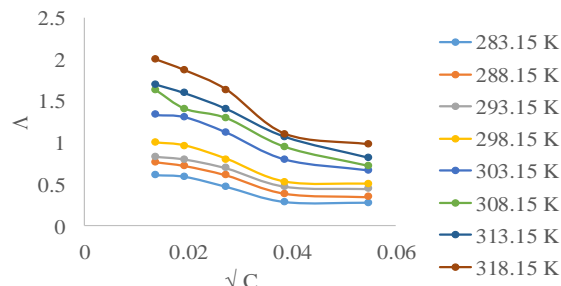*Figure 5. Molar conductance vs square root of concentration for compound 3 at different temperature.*

Figure 6. Molar conductance vs square root of concentration for compound 4 at different temperature.

The thermodynamic parameters for the dissociation reaction are obtained from temperature dependence of dissociation constant (Kd). The standard enthalpy (ΔH^o) is determined from slope of the logarithm (Kd) vs 1/T with (ΔG^o and ΔS^o). The slope is equal to ($-\Delta H/R$) to find Enthalpy, the intercept equal to ($\Delta S/R$) for finding entropy and then to calculate Gibbs free energy used [24, 25].

$$\Delta G = \Delta H - T\Delta S \quad (5)$$

Walden product (previously known the product of viscosity (η) and conductivity at infinite dilution of a solution (Λo) it provides a measurement of the solvent-structuring activity of the solute) estimate as a function of temperature by:

$$\Lambda o(T)\, \eta(T) = \text{constant.} \quad (6)$$

where $\eta(T)$ is a viscosity depends on temperature. The minimization of Λo and K_d values of complete and modified Fuoss-Hsia equations is estimated for compounds (1-3) then compared with compound 4 in 2-methoxy ethanol as a solvent. The results show that the increase of alkyl group chain leads to the decrease of the conductivity. The kinetics (osmotic) terms contributed to the increase in velocity of the ion. It is obvious from the minimization technique that the parameter Λo is expected to have the greatest effect on the values of S^2 during the variation of the two parameters K_d and Λo. Thus, Λo is the leading term in all the conductance equations. However, Λo is relatively insensitive to the values of K_d at the corresponding of minimum of S^2. Dissociation constants that are given in Tables (2, 3, 4 and 5) at different temperatures can therefore anticipate that these compounds do not behave as strong electrolyte and that their dissociations are far from complete. It can observe ion-pair (IP) or solvent separate ion pair (SSIP) formation according to the quantitative conductance data. For understanding the thermodynamic of the dissociation reactions it is useful to consider the enthalpic and entropic contribution to these dissociation and Gibbs free energy. This proves that dissociation for compound is true for compared (as showed in appendix). The standard enthalpy, free energy and entropy changes are determined by using [23] at different temperatures. The summary at this point gives the conductometric dissociation constant K_d to determine the standard free energy change for the postulated equilibrium. This opens the way to search for correlation between ΔG^o, ΔH^o and ΔS^o on the one hand , and to solutes and solvents on the other hand. According to minimization technique used here, the best K_d and Λ_o show an expected trend with temperature. Tables 2, 3, 4 and 5 clearly shows the temperature dependence of the Λ_o value. The increase of temperature leads to the increase of Λ_o and decrease of K_d, as a consequence the association of the compounds increases. As it is mentioned above, there is no literature value of Kohlrausch's law (independent migration of ions) for compounds 1, 2, 3 and 4 compared with the practical finding of Λ_o, therefore the formed results calculated based on statistical S^2. The above Figures from 7, 8, 9 and 10 show the good agreement for the thermodynamic parameters.

Table 6. Thermodynamic data for compound 1 using both equations.

Temperature K	Fuoss-Hsia Modified			Fuoss-Hsia Complete		
	$-\Delta H^o$ kJ mol^{-1}	ΔG^o kJ mol^{-1}	$-\Delta S^o$ J K^{-1} mol^{-1}	$-\Delta H^o$ kJ mol^{-1}	ΔG^o kJ mol^{-1}	$-\Delta S^o$ J K^{-1} mol^{-1}
283.15		52.57			47.06	
288.15		53.57			47.96	
293.15		54.58			48.85	
298.15	4.661	55.59	201.4	3.378	49.75	179.4
303.15		56.59			50.65	
308.15		57.60			51.54	
313.15		58.61			52.44	
318.15		59.61			53.34	

Table 7. Thermodynamic data for compound 2 using both equations.

Temperature K	Fuoss-Hsia Modified			Fuoss-Hsia Complete		
	$-\Delta H^o$ kJ mol^{-1}	ΔG^o kJ mol^{-1}	$-\Delta S^o$ J K^{-1} mol^{-1}	$-\Delta H^o$ kJ mol^{-1}	ΔG^o kJ mol^{-1}	$-\Delta S^o$ J K^{-1} mol^{-1}
283.15		52.01			33.72	
288.15		52.99			34.33	
293.15		53.96			34.95	
298.15	3.260	54.94	195.2	1.166	35.57	123.2
303.15		55.91			36.18	
8.15		56.89			36.80	
313.15		57.87			37.41	
318.15		58.84			38.03	

Table 8. Thermodynamic data for compound 3 using both equations.

Temperature K	Fuoss-Hsia Modified			Fuoss-Hsia Complete		
	$-\Delta H^o$ kJ mol^{-1}	ΔG^o kJ mol^{-1}	$-\Delta S^o$ J K^{-1} mol^{-1}	$-\Delta H^o$ kJ mol^{-1}	ΔG^o kJ mol^{-1}	$-\Delta S^o$ J K^{-1} mol^{-1}
283.15		40.39			39.72	
288.15		41.12			40.44	
293.15		41.84			41.15	
298.15	0.750	42.57	145.3	0.748	41.86	142.9
303.15		43.30			42.58	
308.15		44.02			43.29	
313.15		44.75			44.01	
318.15		45.48			44.72	

Generally, the thermodynamic functions (ΔH give information about energy, ΔS give information about disorder in given system and (ΔG give information about spontaneous in the forward and backward directions and equilibrium in this case may be positive or negative depending on temperature). The good agreement for the Walden product is the interpretation of the high viscosity of the medium [17, 26] while the K_d and Λ_o are showing the direct proportional sign minimization technique depending on the sum squire (S^2) or standard deviation (σ) which is a different between theoretical and practical values. However, the thermodynamic parameters are given good results about the interpretation between solute and solvent in non-aqueous

solvent. Concerning the ΔH, it is determined from the slope of lnKd versus 1/T as shown in Figures (7, 8, 9 and 10) in which the negative values of enthalpy reflects weak interaction between cation and anion for all compounds. Therefore, the solvation is weak.

Table 9. Thermodynamic data for compound 4 using both equations.

Temperature K	Fuoss-Hsia Modified			Fuoss-Hsia Complete		
	$-\Delta H^{\circ}$ kJ mol^{-1}	ΔG° kJ mol^{-1}	$-\Delta S^{\circ}$ J K^{-1} mol^{-1}	$-\Delta H^{\circ}$ kJ mol^{-1}	ΔG° kJ mol^{-1}	$-\Delta S^{\circ}$ J K^{-1} mol^{-1}
283.15		53.49			45.16	
288.15		54.52			46.03	
293.15		55.55			46.90	
298.15	4.670	56.57	205.4	4.107	47.77	199.0
303.15		57.60			48.64	
308.15		58.63			49.51	
313.15		59.66			50.38	
318.15		60.68			51.25	

The existence of intermolecular hydrogen bonding between –OH group with oxygen atom of –COOH group in compound-1 restricts the ionization of hydroxyl group, which leads to the decrease in conductivity.

The ΔS decreases by the increase of temperature due to different changes between solute and solvent, or may be the consequence of attribution to formation of ion-pair or solvent separated ion pair interactions. The negative value of entropy is never spontaneous and the effect is produced by the charge species (ion and ion-pair) on the neighbored solvent molecules and its usefulness in investigating the media properties. However, ΔH and ΔS values proves the useful structural information of solute species and solute-solvent interaction [17]; therefore the entropy asserts that the investigating of media, and the negative value of entropy is important for the opposite effect produced by charge species (ion, IP, SSIP) on the neighbor solvent molecule. For the Gibbs, free energy values are never shown spontaneous reaction as they are observed in the solute and solvent interaction for the all compound compared with compound 4, i.e. the reaction needs temperature, stirring or pressure for the complex reaction to happen. The Walden product depends on temperature showed that the information could be obtained on ion solvent interactions as they are stated in Tables (2, 3, 4 and 5). The dissociation constant sequences of the compounds (1, 2, 3, and 4) are illustrated below:
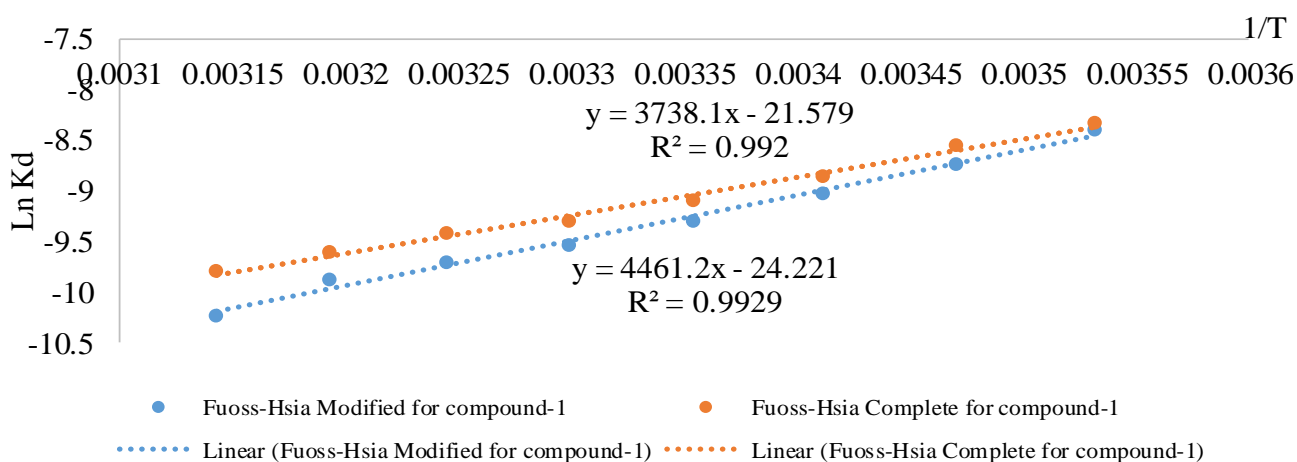

$y = 3738.1x - 21.579$
$R^2 = 0.992$

$y = 4461.2x - 24.221$
$R^2 = 0.9929$

- Fuoss-Hsia Modified for compound-1
- Fuoss-Hsia Complete for compound-1
- Linear (Fuoss-Hsia Modified for compound-1)
- Linear (Fuoss-Hsia Complete for compound-1)

Figure 7. logarithm dissociation constant vs inverse temperature for compound 1.

$y = 1166.2x - 14.817$
$R^2 = 0.9946$

$y = 3260.8x - 23.48$
$R^2 = 0.9901$

- Fuoss-Hsia Modified for compound-2
- Fuoss-Hsia complete for compound-2
- Linear (Fuoss-Hsia Modified for compound-2)
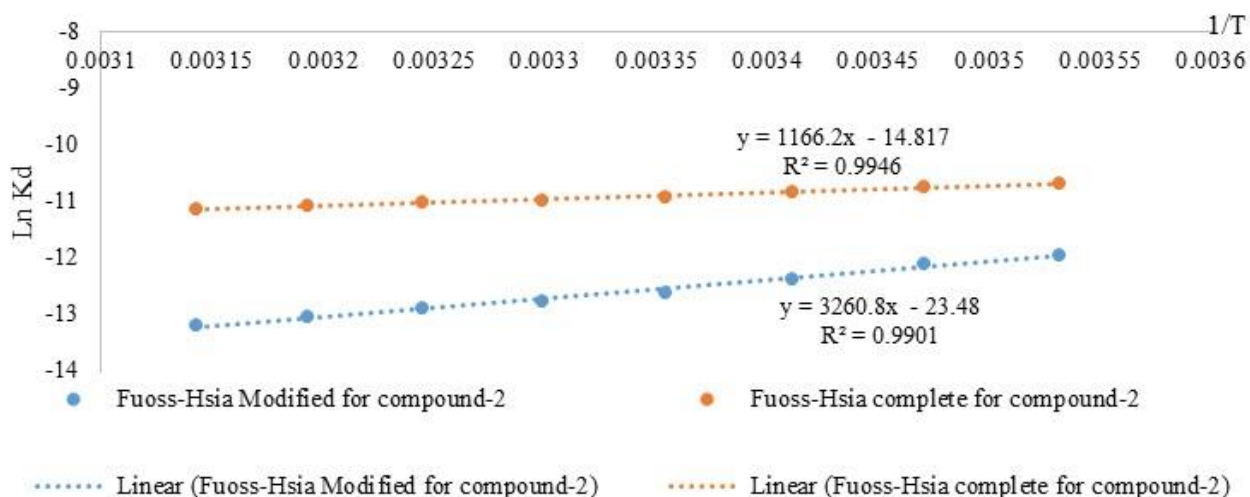- Linear (Fuoss-Hsia complete for compound-2)

Figure 8. logarithm dissociation constant vs inverse temperature for compound 2.
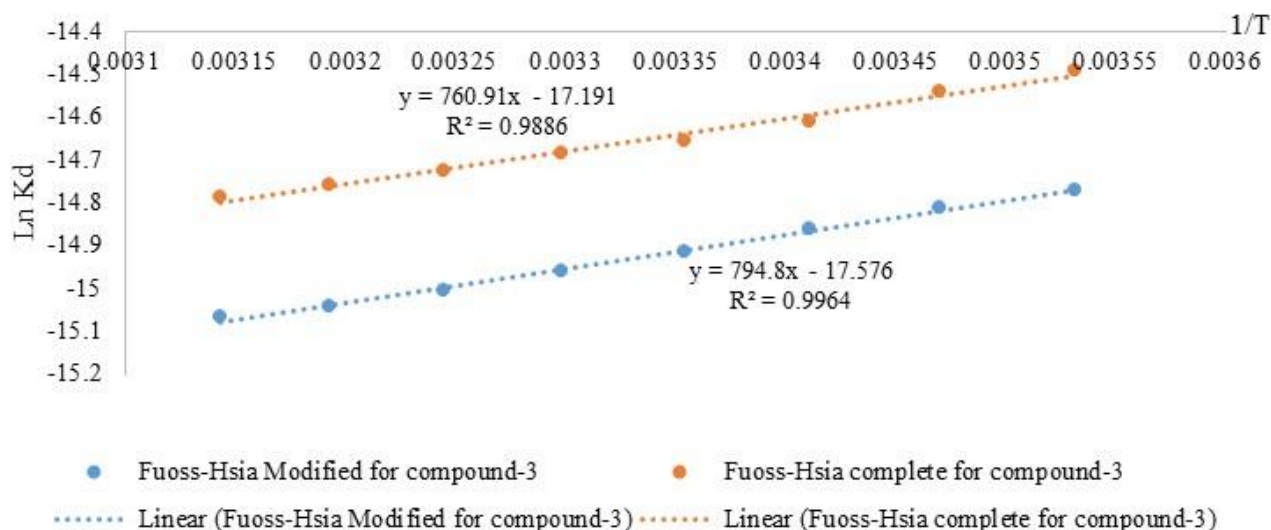
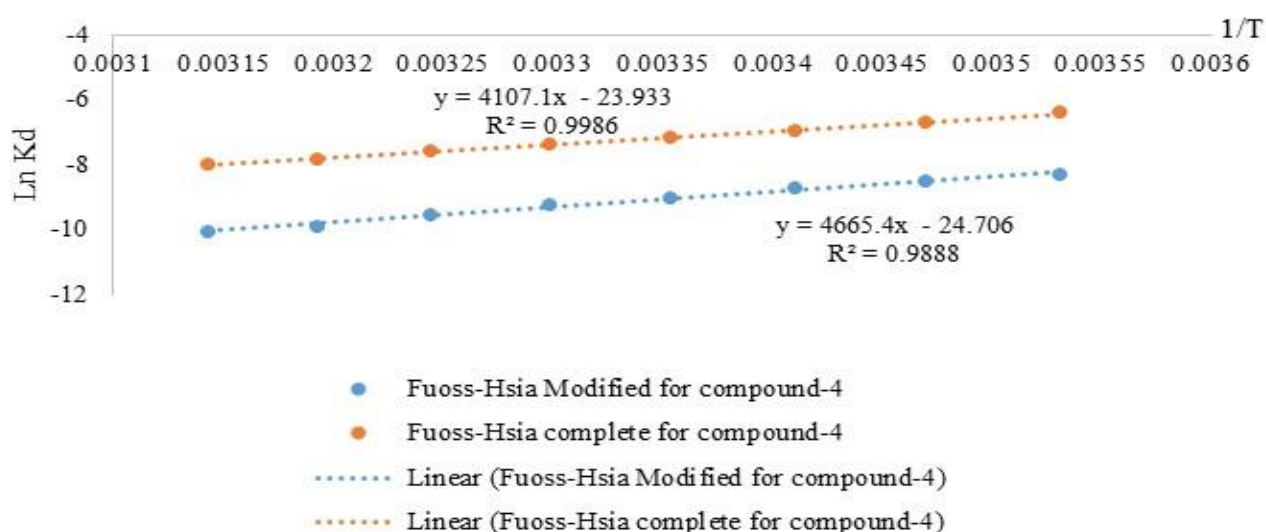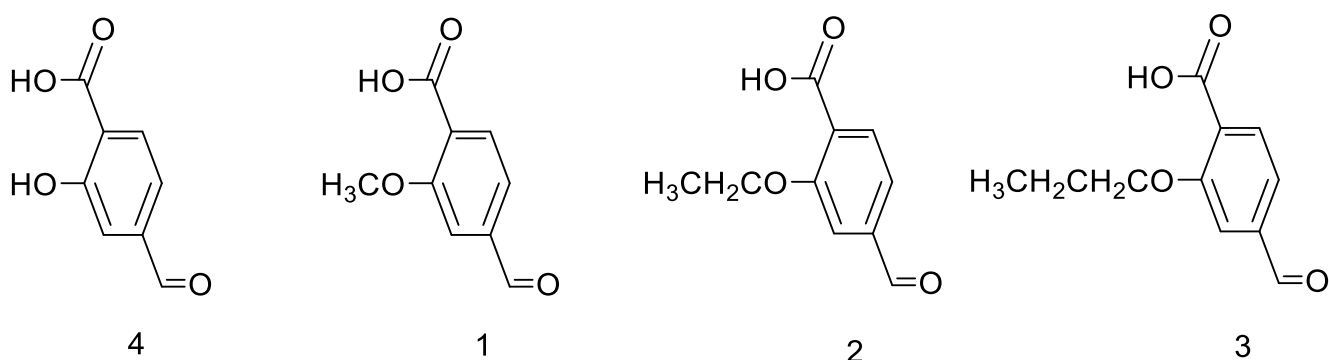*Figure 9. logarithm dissociation constant vs inverse temperature for compound 3*

Figure 10. logarithm dissociation constant vs inverse temperature for compound 4.

Decrease of Kd

Figure 11. K_d scal for all compounds.

Both $-OCH_3$ and $-OH$ groups have exhibited two effects on the aromatic ring: (1) Electron donates resonance or mesomeric effect (+M), and (2) Electron withdraws inductive effect (-I). For both acids, the electron withdrawing inductive effect (-I) is almost the same since both $-OCH_3$ and $-OH$ groups are 4 carbons away from the acid center. However, when $-OH$ group is attached to ortho-position, it has a more tendency to delocalize its lone pair electrons towards the aromatic ring than that of $-OCH_3$ group (Order of activating: $-O- > -OH > -OCH_3$). As a result, the electron density on the carbon ortho to $-OH$ substitution group increases more than that on the carbon ortho to $-OCH_3$ substitution group. Another explanation, due to steric reasons, the C(benzene)−O−C(alkyl group) bond angle of

OCH$_3$ is going to be more than the C(benzene)−O−H bond angle of the -OH. Hence, the percent s-character is going to go up for the central oxygen atom in OCH$_3$ relatively (to rationalize this, think of the bond angles associated with sp3, sp2 and sp hybridization and their respective s-characters). Due to increased s-character on both sides of the OCH$_3$ oxygen, it can achieve an overall more electronegative substituent for the ring compared to OH, as the electrons displaced towards the oxygen from the methyl in OCH$_3$ in which it would still experience a lowering in the energy of the σ(O−CH$_3$) bond. Hence, as compared to OH, the ring will be activated less by OCH$_3$. The steric effect also plays a role within the different chain length alkoxy compounds, as a result thee dissociation order is (-OCH$_3$> - OCH$_2$-CH$_3$> - OCH$_2$-CH$_2$-CH$_3$) see Figure 11.

4. Conclusion

In conclusion, compounds of 1, 2, 3 are analyzed and compared with compound 4 with the use of conductometric methods in 2-methoxy ethanol as a solvent at different temperatures ranged between 283.15K-318.15K, evaluated by audio frequency conductance using both Fuoss-Hsia equations (modified and complete). A minimization technique is used here to estimate dissociation constant and molar conductance at infinity dilution with different temperatures. When the Λ_0 increases, the dissociation decreases at increased temperature, due to more ions formation in a solution, and greater conductance is reached. In addition of that, it was clearly observed that (CIP and SSIP) have their impact on conductivity. The Walden product also substantially increases with temperature. Finally, the standard thermodynamic parameters have been calculated deriving from mentioned temperature depending on dissociation constant, the thermodynamic functions (ΔG^o, ΔH^o and ΔS^o) showed a good indication on solute-solvent interaction. It was also concluded that mesomeric effect and the inductive effect also have their role on this study.

Nomenclature

-OCH$_3$	Methoxy group,
-OCH$_2$-CH$_3$	Methoxymethane
-OCH$_2$-CH$_2$-CH$_3$	Methoxyethane
-OH	Hydroxyl group
-COOH	Carboxyl acid group)
Λ	Molar conductance (S m^2 mol^{-1})
Λ_0	Molar conductance in the limit of zero concentration
K	Coefficient related to the stoichiometry of the electrolyte
C	Concentration of the electrolyte (mEq/L)
E	Constant factor,
Jc	Long-range interaction
K$_A$Λ$_{0c}$	Pair formation near in concentration
H$^+$	Proton
Kd	Dissociation constants (M)
KA	KMAX in steps of DKA
L0	L0MAX in steps of DL0
η	Viscosity of solvent (kg·m^{-1}·s^{-1})
D	Dielectrically constant of solvent
T	Absolute temperature (K)
Z	Valence of electrolyte
K$_A$	Initial K$_A$ value
N	C$_i$/Λ$_i$ pair numbers
C	(I, J) (N pairs of C and Λ data)
ΔH^o	Standard enthalpy (kJ mol^{-1})
ΔG^o	Gibbs free energy (J or KL)
ΔS^o	Standard entropy (J/K·mol)

References:

[1] O. Owoyomi, J. Ige, and O.J.C.S.J. Soriyan, "Thermodynamics of micellization of n-alkyltriphenylphosphonium bromides: a conductometric study," *Chem Sci J*, *25*, 1-13. 2011.

[2] A. Mehrdad and M.J.T.J.o.C.T. Hajikarimi, "Conductometric investigation of ceftriaxone disodium in aqueous solutions of 1-propanol and 2-propanol," *J Chem Thermodyn, 142*, 105972. 2020.

[3] Y. O Al-Allaf, M. Y Al-Tamer, and M.J.R.J.o.S. N Abdulfattah, "Conductometric studies for association reaction of some amino acid complexes in water," *Raf. J. Sci.*, *24*, 45-60. 2013.

[4] V. Sokol, R. Tomaš, M. Višić, and I.J.J.o.s.c. Tominić, "Conductometric study of potassium bromide in 2-butanol+ water mixtures," *J Solution Chem, 35*, 1687-1698. 2006.

[5] F.M.J.T.E.P.O.S.T.E. Al-Healy and Mathematics, "Electrical Conductance Study of Glutamic Acid Complex with [Mn (II)] in Different Solvents and Temperatures," *EPSTEM, 11*, 20-28. 2020.

[6] D.M. Murad, A.Z. Al-Rubaie, and A.A. Al-Najar. (2019). Conductametric studies of some organotellurium (IV) trihalides. in *J Phys: Conference Series*. IOP Publishing.

[7] R. Thakur, R. Sharma, and A. Sharma. (2020). Molecular interactions analysis of some aluminium salts in binary aqueous solutions of tetrahydrofuran (THF): Acoustic and Conductometric approach. in *J Phys: Conference Series*. IOP Publishing.

[8] R.T.Morrison and R.N. BoYd, (2002). *Organic Chemistry*, Asoke K. Ghosh, Prentice-Hall of India Private Limited, M-97, Connaught Circus, New DelhF110001 and Printed by Jay Print Pack Private Limited, New Delhi-10015, India

[9] R.M. Fuoss and K.-L.J.P.o.t.N.A.o.S. Hsia, "Association of 1-1 salts in water," *Pnas, 57*, 1550-1557. 1967.

[10] M. Haisa, S. Kashino, F. Ikejiri, T. Ohno, and K. Teranishi, "Topochemical studies. VIII. The crystal and molecular sturtures of two polymorphs of 4-formylbenzoic acid," *Acta. Crystallogr. B. Struct. Sci. Cryst. Eng. Mater.*, *32*, 857-860. 1976.

[11] M. Nandi, J. Mondal, K. Sarkar, Y. Yamauchi, and A. Bhaumik, "Highly ordered acid functionalized SBA-15: a novel organocatalyst for the preparation of xanthenes," *Chem comm*, *47*, 6677-6679. 2011.

[12] N. Sunsandee, M. Hronec, M. Štolcová, N. Leepipatpiboon, and U. Pancharoen, "Thermodynamics

of the solubility of 4-acetylbenzoic acid in different solvents from 303.15 to 473.15 K," *J. Mol. Liq.*, *180*, 252-259. 2013.

[13] W. Sun, W. Qu, and L. Zhao, "Solubilities of 4-Formylbenzoic Acid in Ethanoic Acid, Water, and Ethanoic Acid/Water Mixtures with Different Compositions from (303.2 to 473.2) K," *J. Chem. Eng. Data.*, *55*, 4476-4478. 2010.

[14] N. Sunsandee, S. Suren, N. Leepipatpiboon, M. Hronec, and U. Pancharoen, "Determination and modeling of aqueous solubility of 4-position substituted benzoic acid compounds in a high-temperature solution," *Fluid Ph. Equilibria*, *338*, 217-223. 2013.

[15] H. Kabir, R.K. Nath, K. Hossain, and M.M.Z. Hyder, "Conductimetric Properties of Benzoic Acid in Water and 1-Propanol Mixtures at the Temperatures from 298.15 to 313.15 K," *Orient. J. Chem.*, *34*, 196-202. 2018.

[16] N. Raghavendra, "Conductometric study on the benzoic acid in water+ methanol systems at different solution temperatures," *Asian J. Nanosci. Mater*, *2*, 350-355. 2019.

[17] G. Franchini, E. Ori, C. Preti, L. Tassi, and G. Tosi, "A conductometric study of dissociation of picric acid in 2-methoxyethanol and 1, 2-ethanediol from− 10 to 80° C," *Can. J. Chem.*, *65*, 722-726. 1987.

[18] M.W. Farrar and R. Levine, "The oxidation of certain ketones to acids by alkaline hypochlorite solution," *J. Am. Chem. Soc. 71*, 1496-1496. 1949.

[19] N.K.R. Shekhani, "Dissociation constants of Proline and Valine in solvent mixture," *Indian J. Chem,* 80-82. , 2000.

[20] R.M. Fuoss and K.-L. Hsia, "Association of 1-1 salts in water," *PNAS, 57*, 1550. 1967.

[21] R. Fernandez-Prini, "Conductance of electrolyte solutions. A modified expression for its concentration dependence," *J. Chem. Soc. Faraday Trans.*, *65*, 3311-3313. 1969.

[22] K.N. Kaka, A.A. Al-Najar, and W.M. Hamad, "The Audio Frequency Conductance Study of Some Metal Succinate Salts in Aqueous Medium at Different Temperatures (Part Ii: Zinc, Nickel and Cobalt Succinates)," *Sjuoz*, *1*, 780-790. 2013.

[23] K.N.K. Baban, (2008). *AFC study of some metal succinate salts in aqueous medium at different temperature*, *Koya Universuty*. Ph.D. thesis, College of Science, Chemistry department

[24] V. Sokol, I. Tominić, R. Tomaš, and M. Višić, "Thermodynamics of the Association Reaction of Li+ and Br–Ions in 2 Butanol+ Water Mixtures from Conductivity Measurements," *Croatica chemica acta*, *78*, 43-47. 2005.

[25] A. Sepsey, É. Horváth, M. Catani, and A.J.J.o.C.A. Felinger, "The correctness of van't Hoff plots in chiral and achiral chromatography," *1611*, 460594. 2020.

[26] M.F. Bakr, "Investigation of magnesium (II), calcium (II) and barium (II) complexes in Aqueous solution." 2005.

Research Article

Solubility Prediction of Lornoxicam in Different Pure Solvents Using Semi-Empirical Correlations and Thermodynamic Models

[1]*R. Kumar [ID], [2]A. K. Thakur [ID], [3]A. Kulabhi [ID], [4]A. Mishra [ID]

[1,2,3] Department of Chemical Engineering, Energy Cluster, University of Petroleum & Energy Studies, Dehradun, India, 248007
[4] Department of Chemical Engineering, BTKIT, Dwarahat, India, 263653
E-mail: [1]*rahul.iitrahul@gmail.com

Abstract

The solubility data of Active Pharmaceutical Ingredients in organic solvents is an essential for pharmaceutical crystallization and drug formulation. In this work, two semi-empirical correlations- the Yaws model and λ-h model- and two thermodynamic models – Wilson Model and the Non-random two-liquid model- are used to estimate the solubility of lornoxicam in ethanol and water. The model parameters and correlations coefficients are calculated by optimizing the average relative deviation. The values of these parameters will be helpful to estimate the solubility of lornoxicam at different temperatures where the experimental solubility data is not available. The predicted solubility data of lornoxicam can be further utilized in the pharmaceutical crystallization and drug formulation.

Keywords: Solubility; crystallization; lornoxicam; thermodynamic model; mixing property.

1. Introduction

Lornoxicam is a non-steroidal anti-inflammatory drug (NSAID) having low aqueous solubility and high permeability through biological membranes leading to low bioavailability [1]. Several approaches such as complexation with cyclodextrins, solid dispersion, emulsion and co-crystallization are employed to enhance the solubility and subsequently bioavailability of active pharmaceutical ingredients (APIs). The low aqueous solubility of lornoxicam leads to a slow dissolution rate as evident by Noyes –Whitney equation [2]. Nanoparticles exhibited higher saturation solubility as compared to bulk particles which can be described by the Ostwald-Freundlich equation [3]. Several particle engineering based approaches such as solid-lipid particles, nanocrystals and nano-emulsion have been explored recently to enhance the dissolution rate of lornoxicam [4–7].

Noyes-Whitney's equation:

$$\frac{dW}{dt} = \frac{DA(C_s - C)}{L} \tag{1}$$

where $\frac{dW}{dt}$ is the dissolution rate, A is the surface area of the particles, C_s is the drug's saturation solubility, C is the drug's concentration in the dissolution medium, D is the diffusion coefficient, and L is the thickness of the diffusion layer.

Ostwald-Freundlich's equation:

$$\log \frac{C_s}{C_\infty} = \frac{2\sigma V}{2.303 RT \rho r} \tag{2}$$

where C_s is the saturation solubility, C_∞ is the solubility of the large particles of the drug, V is the molar volume, σ is the interfacial tension, R is the universal gas constant, T is the absolute temperature, r is the radius of the drug particle and ρ is the density of the drug.

Liquid antisolvent crystallization (LASC) is emerging as a promising approach to prepare the nanoparticles of APIs having poor aqueous solubility. In the liquid antisolvent process, a drug is first dissolved in a suitable solvent followed by its mixing with the antisolvent. To carry out LASC, the solubility of a drug must be known in different solvents. The solubility is measured experimentally at different temperatures which is time-consuming and expensive. Therefore, the prediction of solubility via semi-correlations and thermodynamic models is desirable at different temperatures. Yarraguntla et al. prepared the nanocrystals of lornoxicam via the antisolvent precipitation method [8]. The dissolution rate of the nano-sized drug is substantially increased, from 30.62 % for the raw drug to 60.44 % for the processed drug in 60 minutes. They reported that the average particle size reduced from 3.04 μm to 149 nm.

In this work, the solubility of lornoxicam in different pure solvents using semi-empirical correlations and thermodynamic models has been carried out. The experimental values have been compared with the model predictions. This study will be helpful for the drug formulation techniques to improve the dissolution rate and bioavailability of lornoxicam.

2. Semi-empirical Correlations and Thermodynamic Models

The equilibrium solubility data of lornoxicam is correlated with the Yaws model, Buchowski-Ksiazaczak (λh) model, Wilson model and NRTL model. The description of these models is given in this section.

2.1 Yaws Model

The solubility data of API can be fitted as a function of temperature by the following semi-empirical correlation also known as the Yaws model [9].

$$\ln x_1 = C_1 + \frac{C_2}{T} + \frac{C_3}{T^2} \tag{3}$$

where C1, C2 and C3 are the model parameters which are estimated by fitting the solubility data with temperature. T is the temperature in Kelvin.

2.2 Buchowski-Ksiazaczak (λh) Model

The solubility of a drug is calculated by two parameters ($\lambda \ and \ h$) model described by the following semi-empirical correlation [10]. This model requires the melting temperature (T_m) of the drug which can be calculated by differential scanning calorimetry (DSC) analysis.

$$\ln \left[1 + \lambda \left(\frac{1 - x_1}{x_1} \right) \right] = \lambda h \left[\frac{1}{T} - \frac{1}{T_m} \right] \tag{4}$$

2.3 NRTL Model

The solubility of solute can be written as the following form by the NRTL thermodynamic model [11].

$$\ln x_1 = \frac{\Delta_{fus} H}{R} \left(\frac{1}{T_m} - \frac{1}{T} \right) - \ln \gamma_1 \tag{5}$$

where, γ_1 is the activity coefficient for lornoxicam in the mixture which can be computed by the NRTL model

$$\ln \gamma_1 = x_2^2 \left[\frac{\frac{\Delta g_{21}}{RT} \left(e^{-\alpha_{12} \frac{\Delta g_{21}}{RT}} \right)^2}{\left(x_1 + x_2 e^{-\alpha_{12} \frac{\Delta g_{21}}{RT}} \right)^2} + \frac{\frac{\Delta g_{12}}{RT} \left(e^{-\alpha_{12} \frac{\Delta g_{21}}{RT}} \right)^2}{\left(x_2 + x_1 e^{-\alpha_{12} \frac{\Delta g_{12}}{RT}} \right)^2} \right] \tag{6}$$

where, α_{12} represent the non-randomness of the mixture and the value of this lies between 0.2 to 0.47. Δg_{12} and Δg_{21} are adjustable energy interaction energy parameters.

2.4 Wilson Model

The Wilson equation is also widely used to describe the behavior of the solid-liquid phase equilibrium. The activity coefficient by the Wilson thermodynamic model is calculated by the following expression [12].

$$\ln \gamma_1 = -\ln \left(x_1 + \wedge_{12} x_2 \right) + x_2 \left[\frac{\wedge_{12}}{x_1 + \wedge_{12} x_2} - \frac{\wedge_{21}}{x_2 + \wedge_{21} x_1} \right] \tag{7}$$

$$\wedge_{12} = \frac{v_2}{v_1} \exp \left(-\frac{\Delta \lambda_{12}}{RT} \right) \tag{8}$$

$$\wedge_{21} = \frac{v_1}{v_2} \exp \left(-\frac{\Delta \lambda_{21}}{RT} \right) \tag{9}$$

v_1 and v_2 are the mole volume of lornoxicam and solvent respectively.

The model parameters are estimated using the non-linear regression method. To examine the applicability and accuracy of these models, the average relative deviation (ARD%) as shown by equation (10) has been optimized and calculated.

$$ARD\% = \frac{100}{N} \sum_{i=1}^{N} \left| \frac{x_i^{\exp} - x_i^{cal}}{x_i^{\exp}} \right| \tag{10}$$

where $x_i^{\exp}$ and x_i^{cal} represent the experimental and calculated solubility of lornoxicam respectively. N stands for the number of experimental points. Shakeel et al. reported the experimental data of the solubility of lornoxicam in ethanol and water [13].

2.5 Thermodynamic Function of Mixing

The mixing properties such as mixing enthalpy, mixing entropy and mixing Gibbs free energy for ideal binary solutions can be estimated by the given equations [14] :

$$\Delta_{mix} G^{id} = RT \sum_i^N x_i \ln x_i \tag{11}$$

$$\Delta_{mix} H^{id} = 0 \tag{12}$$

$$\Delta_{mix} S^{id} = -R \sum_i^N x_i \ln x_i \tag{13}$$

where x_i is the mole fraction of component i.

In the real binary system, the mixing properties can be calculated from the ideal ones given the known excess properties

$$\Delta_{mix} G = \Delta_{mix} G^{id} + G^E \tag{14}$$

$$\Delta_{mix} H = \Delta_{mix} H^{id} + H^E \tag{15}$$

$$\Delta_{mix} S = \Delta_{mix} S^{id} + S^E \tag{16}$$

where G^E, H^E, and S^E refers to the excess properties, which can be computed by the following equations:

$$G^E = RT \sum_i^N x_i \ln \gamma_i \tag{17}$$

$$G^E = RT (x_1 \ln \gamma_1 + x_2 \ln \gamma_2) \tag{18}$$

$$G^E = -RT [x_1 \ln(x_1 + x_2 \Lambda_{12}) + x_2 \ln(x_2 + x_1 \Lambda_{21})] \tag{19}$$

$$H^E = -T^2 \left[\partial (G^E / T) / \partial T \right] \tag{20}$$

$$H^E = x_1 x_2 \left[\frac{\Delta \lambda_{12} \Lambda_{12}}{(x_1 + \Lambda_{12} x_2)} + \frac{\Delta \lambda_{21} \Lambda_{21}}{(x_2 + \Lambda_{21} x_1)} \right] \tag{21}$$

$$S^E = \frac{H^E - G^E}{T} \tag{22}$$

3. Results and Discussions

In this work, the solubility of lornoxicam is predicted by different semi-empirical correlations and thermodynamics models. In table 1, the experimental data and model predictions are reported. Table 2 shows that coefficient of correlation (R^2) of these models. It is evident from Figure 1 that the Yaws model can accurately predict the solubility of lornoxicam in ethanol and water. The average relative error of Yaws models is found to be 1.67 % and 2.24 % for ethanol and water respectively. The values of A, B and C are found 5.5944, -5152.7, 1190.15 and 5.4293, -5427.08, 5074.63 for ethanol and water respectively. With these values of parameters, the solubility at any temperature can be calculated.
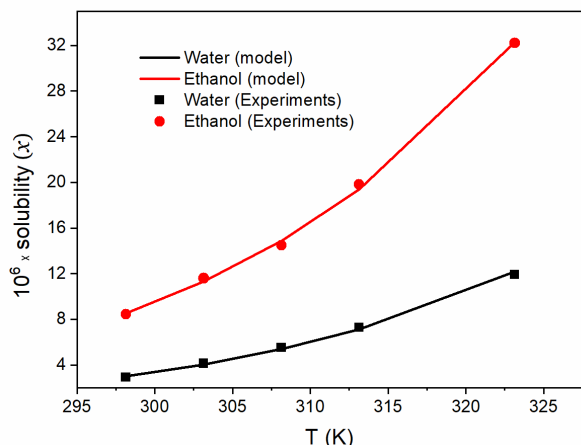

Figure 1: Solubility estimation by Yaws model for ethanol and water and comparison with experiments [13].

Table 1: A comparison between experimental data and model values.

T	Shakeel et al.	Yaws	$(\lambda - h)$	NRTL	Wilson
Solubility of lornoxicam in water, $x \times 10^6$					
298.15	2.91	3.002	1.53	2.59	2.47
303.15	4.12	4.05	2.61	3.72	3.62
308.15	5.52	5.4	4.37	5.28	5.22
313.15	7.27	7.14	7.22	7.41	7.45
323.15	11.9	12.17	18.8	12.46	14.69
Solubility of lornoxicam in ethanol, $x \times 10^6$					
298.15	8.43	8.51	5.73	7.41	6.72
303.15	11.6	11.3	8.95	10.46	9.85
308.15	14.5	14.9	13.8	14.60	14.27
313.15	19.8	19.4	20.88	20.17	20.42
323.15	32.2	32.3	46.24	33.37	40.47

Table 2: Coefficient of correlation value for different models.

API-solvent system	Coefficient of Correlation (R^2 value)			
	Yaws model	$(\lambda - h)$ model	NRTL model	Wilson model
Lornoxicam-water	0.9469	0.2526	0.8104	0.5230
Lornoxicam-ethanol	0.9972	0.3314	0.8301	0.4849

Buchowski-Ksiazaczak (λh) model is found to predict the solubility of lornoxicam in ethanol and water with the highest average relative error. To correlate the solubility data

with this model, the fusion temperature (T_m) is required. Kharwade et al. reported the fusion temperature of lornoxicam 479.8 K measured by differential scanning calorimetry [15]. Figure 2 shows the solubility of lornoxicam in ethanol and water. The average relative deviation of the predicted value from the experimental value is found to be 21.8 % and 32.66 % for ethanol and water respectively. The parameters value, λ and h to minimize the average relative deviation are found 0.1565, 51389 and 0.3262, 29629,55 for ethanol and water respectively.
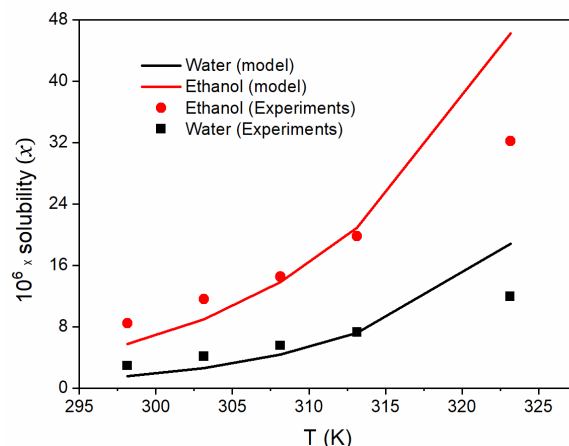

Figure 2: Solubility estimation by Buchowski-Ksiazaczak (λh) model for ethanol and water and comparison with experiments [13].

Wilson model is a thermodynamic model based upon activity coefficient to estimate the solid-liquid equilibria. The model parameters $\Delta\lambda_{12}$ and $\Delta\lambda_{21}$ are estimated to predict the solubility of lornoxicam at different temperatures. The ΔH_f value is required to estimate the solubility which is reported to be 54.3 kJ/mol [15]. The molar volume of lornoxicam is calculated by dividing the molar mass by the density at room temperature. The density of lornoxicam is estimated by the following expression

$$\rho = \frac{zM}{VN_A} \tag{23}$$

where z is the number of formula of lornoxicam in the crystal unit cell, M is the molar mass, V is the volume of the unit cell and N_A is Avogadro number. Nijhawan et al. reported the crystallographic parameters of lornoxicam [16]

The values of model parameters ($\Delta\lambda_{12}$ and $\Delta\lambda_{21}$) are 150.5255, 45333.59 for ethanol and 2767 .707, 47771.45 for water respectively. The average relative deviation is found 10.27 % and 11.73 % for ethanol and water respectively.

The NRTL model is derived from the concept of local composition and is commonly used to describe solid-liquid equilibria. As evident from figure 4, the NRTL model gives good fitting of the experimental solubility data of lornoxicam. The average relative deviation is found 8.11 % for ethanol and 9.23 % for water. The Δg_{12} and Δg_{21}, adjustable energy interaction parameters, are found 3374.12 and 43081.98 for ethanol and 5997.511 and 43209.33 for water. Figure 5 and Figure 6 show the comparison of experimental data with predicted values by each model for ethanol and water respectively.

Kui and Yajun [17] measured the solubility of 2-chlorobenzenesulfonamide in different solvents ad found that NRTL model gave the best fitting performance as

compared to $(\lambda - h)$ model and Wilson model. The authors did not correlate the solubility data with the Yaws model In our work also, NRTL model also gave better results as compared with $(\lambda - h)$ model and Wilson model. However, Yaws model, as it is a semicorrelation rather than based on the complete theoretical principle, gave best result.
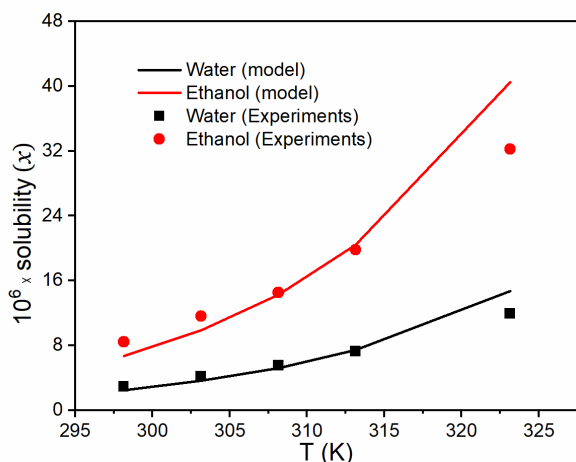

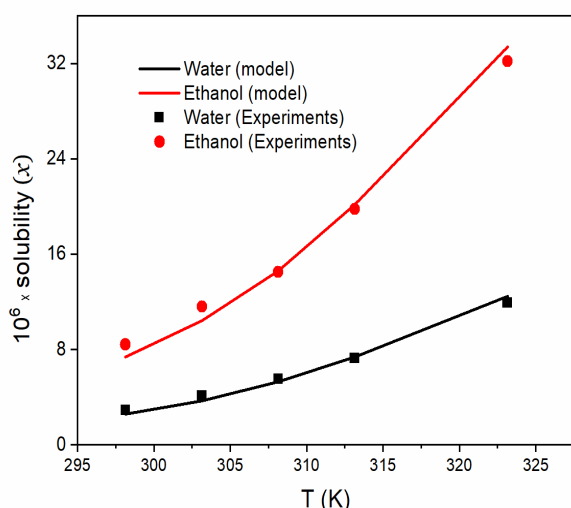*Figure 3: Solubility estimation by Wilson model for ethanol and for water and comparison with experiments [13].*

Figure 4: Solubility estimation by NRTL model and for ethanol and for water water and comparison with experiments [13].
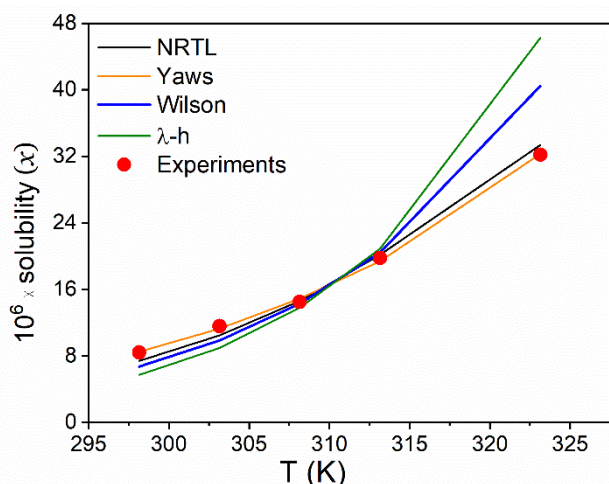

Figure 5: A comparison of experimental solubility data [13] of lornoxicam in ethanol with the predicted values from Yaws model, $\lambda - h$ model, Wilson and NRTL model.
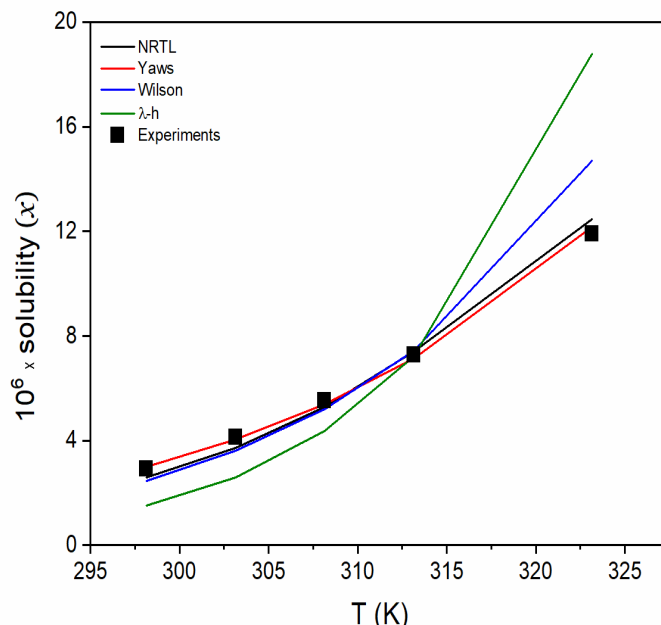

Figure 6: A comparison of experimental solubility data [13] of lornoxicam in water with the predicted values from Yaws model, $\lambda - h$ model, Wilson and NRTL model.

The enthalpy of mixing, entropy of mixing and Gibbs free energy of mixing in ethanol and water are estimated and shown in Table 3. The Gibbs free energy of mixing in all mono-solvents is negative indicating a spontaneous and favorable mixing process of lornoxicam in ethanol and water. The enthalpy of mixing of lornoxicam is positive which means that dissolution is an endothermic process.

Table 3: The thermodynamic properties of lornoxicam in ethanol and water.

T/K	$\Delta_{mix}G$ (kJ/mol)	$\Delta_{mix}H$ (kJ/mol)	$\Delta_{mix}S$ (kJ/mol.K)
Ethanol			
298.15	-0.1637	0.0011	5.528×10^{-4}
303.15	-0.2299	0.0015	7.6348×10^{-4}
308.15	-0.3189	0.0022	10.42×10^{-4}
313.15	-0.4371	0.0031	14.06×10^{-4}
323.15	-0.7945	0.0059	24.77×10^{-4}
Water			
298.15	-0.0570	0.0068	2.1403×10^{-4}
303.15	-0.0814	0.0100	3.0150×10^{-4}
308.15	-0.1148	0.0144	4.1945×10^{-4}
313.15	-0.1599	0.0206	5.7644×10^{-4}
323.15	-0.2999	0.0406	1.54×10^{-4}

4. Conclusion

In this work, the solubility of lornoxicam in ethanol and water has been modeled using two semi-empirical correlations- Yaws model, Buchowski-Ksiazaczak (λh) model - and two thermodynamic models – NRTL model and Wilson Model. The solubility data is required for antisolvent crystallization and different formulation techniques. Each model predicted the solubility increased monotonously with increasing temperature. The best prediction was given by the Yaws model followed by the NRTL model. Based upon the thermodynamic mixing properties, it can be concluded that dissolution of lornoxicam in ethanol and water is spontaneous, endothermic and entropy-driven.

Nomenclature:

A	Surface area of the particle (m^2)
C	Concentration of solute (-)
C_1, C_2, C_3	Constants in Yaws model (-)
C_s	saturation solubility (mol/m^3)
D	diffusion coefficient (m^2/s)
L	thickness of the diffusion layer (m)
C_∞	Solubility of large particles of drug (mol/m^3)
V	Molar volume (m^3)
T	Temperature (K)
R	Universal gas constant (J/mol K)
ρ	Density of drug (kg/m^3)
σ	Interfacial tension (N/m)
λ, h	Constants in Buchowski-Ksiazaczak model (-)
x_l	Drug mole fraction (-)
T_m	Melting temperature of drug (K)
γ_1	Activity coefficients (-)
$\Delta_{fus}H$	Fusion enthalpy (J/m)
x_2	Mole fraction of solvent (-)
$\Delta g_{12}, \Delta g_{21}$	adjustable energy interaction energy parameters in NRTL model (-)
α_{12}	non-randomness of the mixture (-)
$\Delta\lambda_{12}, \Delta\lambda_{21}$	adjustable energy interaction energy parameters in Wilson model (-)
$\Delta_{mix}G^{id}$	Gibbs free energy for ideal solution (J/mol)
$\Delta_{mix}H^{id}$	Enthalpy of mixing for ideal solution (J/mol)
$\Delta_{mix}S^{id}$	Entropy of mixing for ideal solution (J/mol K)
S^E, G^E, H^E	Excess Entropy, Gibbs Free Energy and Enthalpy

References

[1] A. Dadej, A. Woźniak-Braszak, P. Bilski, H. Piotrowska-Kempisty, M. Józkowiak, A. Pawełczyk, D. Dadej, D. Łażewska, A. Jelińska, "Improved solubility of lornoxicam by inclusion into SBA-15: Comparison of loading methods," *Eur J Pharm Sci*, 171, 106133, 2022.

[2] E. Merisko-Liversidge, G.G. Liversidge, E.R. Cooper, "Nanosizing: A formulation approach for poorly-water-soluble compounds," *Eur J Pharm Sci*, 18,113–120, 2003.

[3] W. Wu, L. Wang, S. Wang, "Amorphous silibinin nanoparticles loaded into porous starch to enhance remarkably its solubility and bioavailability in vivo," *Colloids Surf. B: Biointerfaces,* 198, 111474, 2021.

[4] R.U. Khan, S.U. Shah, S.A. Rashid, F. Naseem K.U. Shah, A. Farid, K.R. Hakeem, M.R. Kamli, E.H. Althubaiti, S.A. Alamoudi, "Lornoxicam-Loaded Chitosan-Decorated Nanoemulsion: Preparation and In Vitro Evaluation for Enhanced Transdermal Delivery," *Polymers*, 14, 1922, 2022.

[5] N.T. Tung, T.H.Y. Dong, C.S. Tran, T.K.T. Nguyen, S.C. Chi, D.S. Dao, D.H. Nguyen, "Integration of lornoxicam nanocrystals into hydroxypropyl methylcellulose-based sustained release matrix to form a novel biphasic release system," *Int. J. Biol. Macromol.*, 209 , 441–451, 2022.

[6] M.B. Zewail, G. F.Asaad, S.M. Swellam, S.M. Abdallah, S. K.Hosny, S.K. Sallah, J. E.Eissa, S. S.Mohamed, W.A. El-Dakroury, "Design, characterization and in vivo performance of solid lipid nanoparticles (SLNs)-loaded mucoadhesive buccal tablets for efficient delivery of Lornoxicam in experimental inflammation," *Int. J. Pharm.*, 624, 122006, 2022.

[7] H. Chen, J. Zhang, Q. Qiao, E. Hu, Y. Wei, Z. Pang, Y. Gao, S. Qian, J. Zhang, W. Heng, "A novel soluble lornoxicam-sodium chelate monohydrate with improved plasticity and tabletability," *Int. J. Pharm.,* 624, 122060 2022.

[8] S.R. Yarraguntla, V. Enturi, R. Vyadana, S. Bommala, "Formulation and evaluation of lornoxicam nanocrystals with different stabilizers at different concentrations," *Asian J. Pharm.,* 10, 198–207, 2016.

[9] P. Zhang, Y. Wan, C. Zhang, R. Zhao, J. Sha, Y. Li, T. Li, B. Ren, "Solubility and mixing thermodynamic properties of levamisole hydrochloride in twelve pure solvents at various temperatures," *J. Chem. Thermodyn,* 139, 105882, 2019.

[10] Y. Hu, Z. Cui, J. Ye, L. Yao, Z. Wang, T. Wang, "Determination and analysis of solubility of l-prolinamide in ten pure solvents and three binary solvent mixtures at different temperatures (T = 278.15-323.15 K)," *J. Chem. Eng. Data,* 66, 1172–1184, 2021.

[11] K. Wu, Y. Li, "Solubility and solution thermodynamics of p-toluenesulfonamide in 16 solvents from T = 273.15 to 324.75 K," *J. Mol. Liq.*, 293, 111577, 2019.

[12] C. Ren, Y. Bao, Y. Wang, H. Zhao, "Equilibrium Solubility of p-Nitroacetanilide in Fifteen Neat Solvents: Determination, Correlation, and Solvent Effect," *J. Chem. Eng. Data.*, 67, 267–275, 2022.

[13] F. Shakeel, N. Haq, F.K. Alanazi, I.A. Alsarra, "Solubility of anti-inflammatory drug lornoxicam in ten different green solvents at different temperatures," *J. Mol. Liq.*, 209 280–283, 2015

[14] B E Poling, J M Prausnitz, J P O'Connell, "The properties of gases and liquids," 5th ed., McGraw Hill, 2001.

[15] M. Kharwade, G. Achyuta, C.V.S. Subrahmanyam, P.R.S. Babu, "Solubility behavior of lornoxicam in binary solvents of pharmaceutical interest," *J. Solution Chem*, 41, 1364–1374, 2012.

[16] M. Nijhawan, A. Santhosh, P.R.S. Babu, C.V.S. Subrahmanyam, "Solid state manipulation of lornoxicam for cocrystals-physicochemical characterization," *Drug Dev. Ind. Pharm.*, 40 ,1163–1172, 2013.

[17] W. Kui, L. Yajun, "Solid-liquid phase equilibrium and solution thermodynamics of 2-chlorobenzenesulfonamide in 16 monosolvents at temperature ranging from 273.15 K to 324.65 K, " *J. Mol. Liq.*, 304, 112795, 2020

Research Article

Thermodynamic Studies on Sr₅Nb₄O₁₅

[1]*P. Samui [iD], [2]S.M. Bhojane [iD], [2]B.M. Singh [iD], [2]S.K. Rakshit [iD]

[1,2] Product Development Division, BARC, Trombay, Mumbai, India- 400 085
[1,2] Homi Bhabha National Institute, BARC, Mumbai-85
E-mail: [1]* pradeepsamui@gmail.com

Abstract

The SrO–Nb$_2$O$_5$ system, especially Sr$_5$Nb$_4$O$_{15}$ compound is of interest for their use as an electroceramics. In this work, Sr$_5$Nb$_4$O$_{15}$ compound was synthesized by solid-state reaction and characterised by XRD. Thermodynamic properties like heat capacity, enthalpy of formation and Gibbs energy of formation of Sr$_5$Nb$_4$O$_{15}$ have been measured. The standard molar enthalpy of formation of Sr$_5$Nb$_4$O$_{15}$(s) was determined using an oxide melt solution high temperature calorimeter. Based on these experimental data, a self-consistent thermodynamic function of this compound was also generated. This thermodynamic data is essential for the optimization of synthesis conditions for materials and for the evaluation of their stability under appropriate technological operating conditions.

Keywords: Heat capacity; dsc; high temperature calorimeter; enthalpy of formation; niobates.

1. Introduction

Strontium niobates in the binary system SrO–Nb$_2$O$_5$ are potential multifunctional materials with cation-deficient perovskite structure. They have high dielectric constant, less dielectric loss, and low temperature dependence of dielectric constant. They are promising materials for microwave ceramics [1-3]. They are also investigated as valuable crystal host for luminescent lanthanide ions [4]. Sr$_5$Nb$_4$O$_{15}$ is mainly interesting for their promising photocatalytic activity [5]. Furthermore, in the nuclear industry, ternary oxides of strontium and niobium may form as fission product compounds in an operating nuclear reactor with oxide fuels under certain oxygen potential. Evaluations of thermodynamic stability of these ternary oxides are therefore important for assessment of fission product interactions. Sr$_5$Nb$_4$O$_{15}$(s) is highest melting compound in the SrO-Nb$_2$O$_5$ system. Whiston and Smith have first reported the existence of Sr$_5$Nb$_4$O$_{15}$ compound which is a iso-structural with the tantalum analogue [6]. Earlier, crystal structure analysis of the Sr$_5$Nb$_4$O$_{15}$ compound was performed by Weiden et al. [7]. Recently, in-depth crystal structure analysis on Sr$_5$Nb$_4$O$_{15}$ point to that it crystallizes in the trigonal P-3c1 space group, which is considered to be a subsection of hexagonal structure [8]. The structure contents three inequivalent Sr^{2+} sites, two inequivalent Nb^{5+} sites and three inequivalent O^{2-} sites [8]. Phase relations in the binary system SrO–Nb$_2$O$_5$ were investigated by Carruthers and Grasso [9] and more recently by [10]. A thermodynamic assessment of the SrO–Nb$_2$O$_5$ system was accomplished by Yang et al. [11]. Thermodynamic functions of oxides reported in SrO–Nb$_2$O$_5$ system were assessed using Calphad technique. Leitner et al [12] measured heat capacities (20-350 K) and enthalpy increments (670-1370 K) of strontium niobates. The standard molar entropies at 298 K have been reported from low temperature heat capacity data. There is no experimentally determined heat capacity of this compound from 350-670 K. The Gibbs energy of formation and enthalpy of formation of the compound is not available in literature. Moreover, thermodynamic data of these oxides are also of relevance to compute phase diagram and phase stability of multicomponent systems. Hence, in the present study, Sr$_5$Nb$_4$O$_{15}$(s) was prepared and characterized first. Then heat capacity, Gibbs energy of formation and enthalpy of formation of the compound was determined employing differential scanning calorimetry, Knudsen effusion technique and high temperature oxide melt solution calorimeter, respectively. The thermodynamic table of this compound was also evaluated using heat capacity data.

2. Experimental Procedure
2.1. Synthesis of Compounds and Characterization

Sr$_5$Nb$_4$O$_{15}$(s) powder sample was prepared using conventional solid state reaction route using SrCO$_3$ (Alfa Aesar, mass fraction 0.9995) and Nb$_2$O$_5$ (Alfa Aesar, mass fraction 0.999). Prior to mixing, SrCO$_3$(s) and Nb$_2$O$_5$(s) were first dried under the flow of high purity Ar(g) at 873 K for 8 h and then cooled overnight under continuous flow of Ar(g). Stoichiometric amount of dried carbonate and Nb$_2$O$_5$ were properly mixed using an agate mortar and pestle and made into pellets. The pellet was then heated at 1000 K in a platinum boat for a period of 120 h with three intermediate grindings. Finally, the pellets were powdered and stored inside desiccator. Phase formation and lattice parameters of Sr$_5$Nb$_4$O$_{15}$(s) were determined using a Miniflex 600 X-ray diffractometer (Model: Rigaku, Japan) with graphite monochromatized Cu Kα$_1$ radiation (λ = 0.15406 nm).

2.2 Knudsen Effusion Quadruples Mass Spectrometry (KEQMS)

In this study, an indigenously developed Residual Gas Analyzer (RGA) (Model: Hiden HAL/3F 501, UK) based on quadruple mass spectrometer connected to a Knudsen effusion system was used for measurement of equilibrium partial pressures of permanent gases. The details of the experimental setup have been described by Rakshit et al. [13]. For the sake of clarity, schematic of KEQMS has been presented in Figure 1. The temperature near the Knudsen cell was measured using a pre-calibrated (ITS-90) chromel–alumel thermocouple. The Knudsen cell used was made of boron nitride (BN) with a knife edged orifice of diameter 0.8 mm at the centre of the upper lid. A Faraday cup detector is used to collect the ions generated which is proportional to ion intensity. The ion intensity of the ith ion is related to partial pressure and is represented as:

$$p_i = K_{inst} \cdot (I_i^+ \cdot T) / (\sigma_i \cdot a_i) \qquad (1)$$

Where, K_{inst} is the instrumental constant, I_i^+ is the measured ion current in ampere, T is the absolute temperature, σ_i is the electron impact cross-section and a_i is the isotopic abundance of the specific ion. Taking natural logarithm on both sides, the Eq. (1) can be written as:

$$\ln p_i = \ln K_{inst} + \ln(I_i^+ T) - \ln \sigma_i - \ln a_i \qquad (2)$$

For permanent gaseous species such as CO_2^+ (m/e =44), the value of $\ln \sigma_i$ is - 45.52 at 30 eV [14]. The isotopic abundance of CO_2 is taken as 100% ($\ln a_i = 0$). Thus, Eq. (2) becomes

$$\ln\{p(CO_2 / atm)\} = \ln K_{inst} + \ln(I^+ T) + 45.52 \qquad (3)$$

For Knudsen effusion quadruple mass spectrometry (KEQMS) experiment, a phase mixture of $\{Sr_5Nb_4O_{15}$ (s) + $Nb_2O_5(s) + SrCO_3(s)\}$ was prepared by homogenously mixing the individual compounds in their stoichiometric proportions under moisture free condition and made into pellet. The pellet was heated at 700 K and stored inside desiccators.
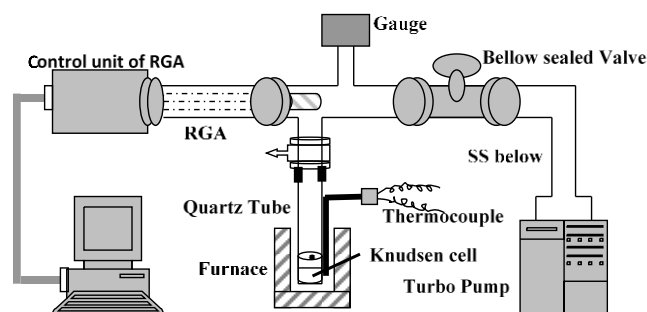

Figure 1. Schematic diagram of KEQMS setup.

2.3 Measurement of Heat Capacity using Differential Scanning Calorimeter

A standard three step method [15], blank-blank, blank-reference and blank-sample was followed for the measurement of the heat flow rate signal of base line, reference and sample, respectively. Heat capacity measurements of known amount of $Sr_5Nb_4O_{15}(s)$ were carried out in a platinum crucible with lids using Labsys Evo1600 simultaneous thermal analyzer system (Setaram Instrumentation, France). The flow rate of 30 mL·min^{-1} of dry argon (purity, 99.9999%) and a heating rate of 5 K·min^{-1} with continuous scanning mode was maintained during all measurements. The phase transition temperature of standard reference materials e.g. In, Sn, Pb, Al and Ag under the scanning rate of 2, 5 and 10 K·min^{-1} was measured for the temperature calibration of the DSC. A temperature correction factor as a function of heating rate was plotted and the value corresponding to zero heating rate was obtained. The corrected temperature was used for the heat capacity measurement of the compound. NIST synthetic sapphire (SRM-720, mass fraction purity 0.9999) was used as reference material with known heat capacity values obtained from the literature [16]. The values of heat capacity of Zirconia (Alfa Aesar, USA, mass fraction 0.99978) were measured in the same temperature range to check the accuracy of the calorimeter which was found to be within ±2% compared to the literature values [16].

2.4 High Temperature Solution Calorimetry

Standard molar enthalpy of formation of $Sr_5Nb_4O_{15}(s)$ was determined by measuring the enthalpy change for the dissolution of $Sr_5Nb_4O_{15}(s)$ and its starting materials such as $SrCO_3(s)$ and $Nb_2O_5(s)$ in liquid $\{PbO + B_2O_3\}$ solvent (in 2:1 molar ratio) at 966 K using Alexsys high temperature calorimeter (Setaram, France). The details of experimental set up and its working formulae has been reported in our earlier publication [17]. ~10g of $\{PbO + B_2O_3\}$ solvent (in 2:1 molar ratio) is taken inside a platinum crucible for each experiment. Three consecutive addition of solute in the solvent were carried out to check the reliability of the experimental data. Calibration of the calorimeter was performed by adding small pieces of synthetic sapphire [NIST SRM-720] [18] from 298 K into platinum crucible, maintained at 966 K. The weight of the sample and synthetic sapphire [NIST SRM-720] was in the range 20-50 mg, respectively. The accuracy of the instrument obtained using enthalpy increment values of molybdenum (99.997% purity) and NBS standard synthetic sapphire (SRM 720) was found to be better than ±2%.

3. Result and discussion
3.1 Characterization

The purity of $Sr_5Nb_4O_{15}(s)$ powder was established by using X-ray diffraction (XRD) analysis. The XRD pattern of the sample is shown in Figure 2 and are compared with that of diffraction line of compound given in the reference (JCPDS XRD file No. 00-048-0421) [19]. The compound crystallizes in the distorted hexagonal unit cell (*P3m*) with the cell parameters a = b = 5.6552(5) Å and c = 11.4557(8) Å. They are in good agreement with that of reported cell parameters such as a = b = 5.6576(6) Å and c = 11.4536(4) Å [20]. No diffraction line corresponding to starting material phases and other unwanted phases were found in the XRD pattern indicating pure form of compound.

3.2 Gibbs Energy of Formation of $Sr_5Nb_4O_{15}$(S) using KEQMS

The calibration of the mass spectrometer with Knudsen cell setup was carried out by measuring the ion intensities of CO_2^+ using the phase mixture of $\{SrCO_3(s) + SrO(s)\}$ at 30 eV ionization energy and keeping the other ion optic parameters constant for all sets of measurements. These ion

intensities and the partial pressure values of the CO_2 from the literature were used for the calculation of K_{inst}. The following equilibrium reaction was established inside the Knudsen cell.
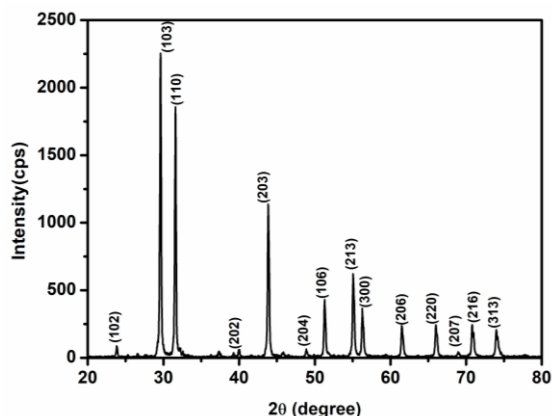
$$SrCO_3(s) = SrO(s) + CO_2(g) \qquad (4)$$

*Figure 2. Powder XRD pattern of $Sr_5Nb_4O_{15}(s)$.*

The individual ion intensities of CO_2^+ peak over the equilibrium phase mixture were recorded at different temperatures. The ion intensities of several runs are least square fitted as a function of temperature and is expressed as:

$$\ln\{I^+(CO_2).T\} = -29426\,(\pm494)\,/\,(T\,/\,K) + 13.5\,(\pm0.54)$$
$$(840 \le T\,/\,K \le 950) \qquad (5)$$

Values of instrument constant was determined by using Eq. (3) and values of partial pressure of $CO_2(g)$ from literature [16] and experimentally determined ion intensity of $CO_2(g)$ over the phase mixture $\{SrCO_3(s)+SrO(s)\}$. The calculated instrumental constant (K_{inst}) as a function of temperature is represented as:

$$\ln K_{inst}\,(\pm0.04) = -39.2 + 633/(T/K) \quad (840 < T/K < 950) \qquad (6)$$

Ion intensity of CO_2^+ over the phase mixture of $\{CaCO_3(s) + CaO(s)\}$ was also measured to check the accuracy of the measurements using the same experimental setup (Figure 1) after determining the partial pressures as a function of temperature. The corresponding equilibrium reaction was:

$$CaCO_3(s) = CaO(s) + CO_2(g) \qquad (7)$$
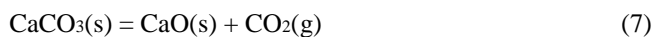
The values of $\ln\{p(CO_2\,/\,atm)\}$ for Eq.(7) was calculated from Eq.(3) and using instrumental constant, Eq.(6) and other values for CO_2^+ ion. The corresponding expression is given as:

$$\ln\{p(CO_2\,/\,atm)\} = -21576\,(\pm597)\,/\,(T/K) + 19.35\,(\pm0.74)$$
$$(690 \le T\,/\,K \le 865) \qquad (8)$$

The enthalpy change related to reaction (7) at the average experimental temperature ($T_{av} = 775$ K) was calculated using Eq. (8) and found to be $\Delta_r H^{\circ}_m\,(775\ K) = (179\pm5)$ kJ·mol^{-1}, which is in good agreement with that of literature (178.5 kJ·mol^{-1}) [16].

Prior to the actual experiment, the background signals were also monitored by heating the Knudsen chamber with empty Knudsen cell at different temperatures from ambient to 1160 K at a pressure level of 1×10^{-5} Pa. The background signals as a function of temperature are shown in Figure 3. It is evident from Figure 3 that the background signals corresponding to H_2^+, N_2^+, CO^+ and CO_2^+ do not change appreciably with change in temperature.
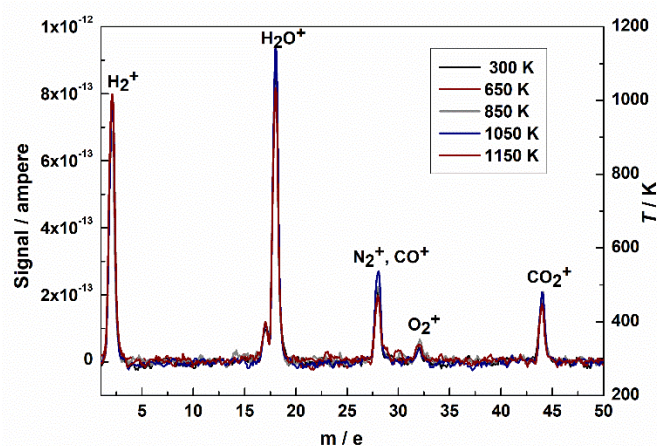

Figure 3: Background signal of KEQMS as a function of temperature.

During experiments, the actual signals were obtained by subtracting the ion intensities due to background. The ion intensities of CO_2^+ for $\{Sr_5Nb_4O_{15}(s) + 5SrCO_3(s) + 2Nb_2O_5(s)\}$ phase mixture was measured at 30 eV ionization energy in the temperature range 870–1055 K. The values of ion intensity of CO_2 over the phase mixture were tabulated in Table 1.

Table 1. Ion intensities of CO_2 peak over equilibrium phase mixture of $\{Sr_5Nb_4O_{15}(s) + 5SrCO_3(s) + 2Nb_2O_5(s)\}$ as a function of temperature.

T/K	I (CO_2^+)/A	T/K	$I^+(CO_2^+)$/A
871.6	4.00E-09	963.7	3.27E-08
887.6	5.49E-09	973.6	4.07E-08
903.2	7.92E-09	980.8	4.76E-08
919.0	1.22E-08	993.6	6.24E-08
934.2	1.66E-08	1013.6	9.73E-08
949.5	2.38E-08	1033.6	1.52E-07
951.6	2.58E-08	1054.7	2.34E-07

Partial pressures of CO_2, $p(CO_2)$, at different temperatures for three different runs were calculated using the measured ion intensities and the calibration constant from Eq. (6). Variation of $\ln p(CO_2)$ as a function of temperature is shown in Figure 4 which shows a linear trend and can be expressed as:

$$\ln\{p(CO_2\,/\,atm)\} = -20887\,(\pm260)\,/\,(T/K) + 18.5\,(\pm0.3)$$
$$(870 < T(K) < 1055) \qquad (9)$$

The following equilibrium reaction was established inside the Knudsen cell under experimental conditions,

$$5SrCO_3(s) + 2Nb_2O_5(s) = Sr_5Nb_4O_{15}(s) + 5CO_2(g) \qquad (10)$$
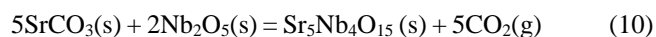
The enthalpy change associated with the above reaction at the average temperature of the measurement was

estimated to be $\Delta_r H^0_m$ (962 K) = 868 kJ mol^{-1}. The standard molar Gibbs energy of reaction, $\Delta_r G^0_m(T)$, was calculated from Eq. (6) using the relation

$$\Delta_r G^0_m(T) \text{ (kJ·mol}^{-1})(\pm 7)= (-RT \ln p_{CO2}) \times 0.001$$
$$= 868 + 0.8 \times T/K \quad (870 < T/K < 1055) \qquad (11)$$
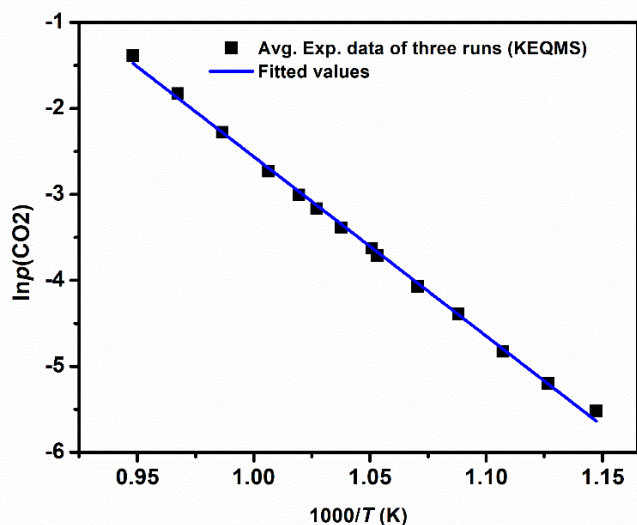

Figure 4: Variation of partial pressure of $CO_2(g)$ as a function of temperature over ternary phase mixture {$Sr_5Nb_4O_{15}$ (s)+5SrCO$_3$(s)+2Nb$_2$O$_5$(s)}.

The standard molar Gibbs energies of formation of $Sr_5Nb_4O_{15}$ from the elements were calculated from Eq.(8) and the values of $\Delta_f G^0_m$ (T) for CO$_2$(g), SrCO$_3$(s) and Nb$_2$O$_5$(s) given in Table 2.

Table 2. Standard molar Gibbs energy of formation, $\Delta_f G^0_m(T)$ of different compounds [16,18].

Compound	$\Delta_f G^0_m(T)$(kJ.mol^{-1})
CO$_2$(g)	-394-0.0016×T
SrCO$_3$(s)	-1223+0.263×T
Nb$_2$O$_5$(s)	-1899+0.180×T

The corresponding expression

$$\Delta_f G^0_m(Sr_5Nb_4O_{15}, s, T) \text{ (kJ.mol}^{-1})(\pm 8)$$
$$= -7075 + 1.3 \times T/K \quad (870 < T(K) < 1055) \qquad (12)$$

The enthalpy of formation of $Sr_5Nb_4O_{15}$(s) from their element at average temperature, 962 K, was -7075(±8) kJ·mol^{-1}.

3.3 Measurement of Heat Capacity

The molar heat capacities of $Sr_5Nb_4O_{15}$(s) were measured as a function of temperature from 300 K–1000 K and the values are presented in Table 3.

Variation of heat capacities of $Sr_5Nb_4O_{15}$(s) was plotted as a function of temperature and is shown in Figure 5. Low temperature heat capacity for this compound has been reported in literature [12] along with heat content of the compound from 670 K-1370 K. Authors have also assessed variation of $C_{p, m}$ function above room temperature by combining the data of heat capacity from DSC and the enthalpy increment from drop calorimetry. There is no direct measurement of high temperature heat capacity data reported in literature. The measured heat capacity data are compared with assessed C_p values in Figure 5.

Table 3. Variation of heat capacity of $Sr_5Nb_4O_{15}$(s) with Temperature. (T in K and $C_{p,m}$ in J·mol^{-1}·K^{-1}).

| T	$C_{p,m}$	T	$C_{p,m}$
300.0	482.5	665.2	583.6
308.5	485.4	673.1	585.1
317.0	488.8	680.8	586.6
325.5	491.9	688.4	588.0
334.0	496.3	696.2	589.5
342.5	499.7	703.9	591.0
350.9	503.6	711.6	592.4
359.4	506.6	719.3	593.8
367.9	509.4	727.1	595.3
375.9	512.6	734.7	596.7
384.4	515.2	742.3	598.1
392.1	518.0	750.0	599.5
400.4	521.0	757.7	600.8
408.7	523.9	765.3	602.2
417.2	526.7	773.1	603.6
425.2	528.6	788.4	606.3
433.7	530.5	796.1	607.7
442.0	533.0	803.7	609.0
450.3	535.5	811.4	610.3
458.7	537.9	819.0	611.7
466.6	540.1	826.6	613.0
474.8	542.4	834.2	614.3
483.0	544.6	841.9	615.6
491.1	546.7	849.5	616.9
499.3	548.8	857.0	618.2
507.3	550.8	864.7	619.5
515.4	552.8	872.1	620.8
523.4	554.8	879.7	622.1
531.4	556.7	887.2	622.6
539.5	558.6	894.8	623.1
547.4	560.4	902.2	624.4
555.5	562.3	909.7	625.6
563.5	563.3	917.4	626.1
571.3	565.0	924.8	627.4
579.1	566.7	932.4	627.9
587.0	568.4	939.9	629.7
594.9	569.4	947.3	630.9
602.8	571.8	955.0	632.1
610.6	573.4	962.4	633.3
618.5	575.0	969.9	635.3
626.3	576.6	977.3	636.3
634.1	578.2	984.9	636.9
642.1	579.1	992.3	638.1
649.6	580.6	999.8	638.6
657.4	582.1	1007.3	639.1
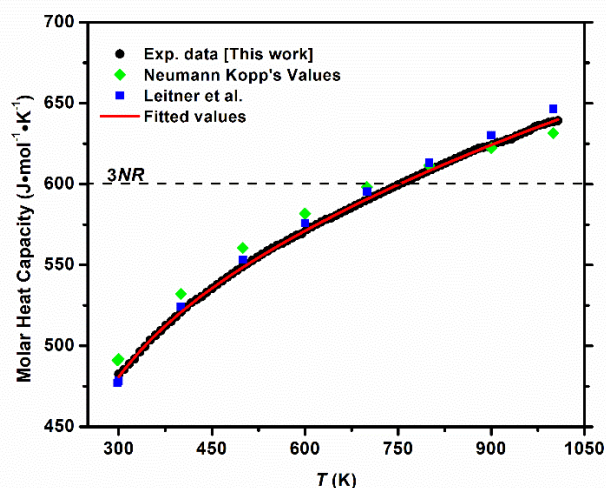
Figure 5: Variation of heat capacity with Temperature of $Sr_5Nb_4O_{15}$ (s) *compound*

The heat capacity data obtained in this study using DSC, is in good agreement with that of estimated one from Neumann Kopp's rule (NKR). The individual values of heat capacities were least square fitted as a function of temperature and the best fit is represented as

$C^o_{p, m}$ (J·mol^{-1}·K^{-1}) = (501.3±1.3)+(0.1438±0.0014)×(T/K)-(5928082±116602)/(T/K)^2 (300 ≤ T / K ≤ 1000)   (13)

The heat capacity values of SrO and Nb_2O_5 for Neumann Kopp's rule (NKR) estimation are taken from the literature [16]. The estimated values of heat capacity using NKR are plotted in Figure 5. It can be seen that the heat capacity values obtained from DSC is slightly lower than the values calculated using NKR up to 900 K. Beyond 900 K, the DSC values is slightly higher than NKR values. According to Dulong Petit Law, the 3NR values for $Sr_5Nb_4O_{15}$(s) is calculated to be 600 J·mol^{-1}·K^{-1}. The interception of experimental heat capacity values with 3NR values indicate the Debye temperature of the compound. The Debye temperature is calculated to be 750 K for $Sr_5Nb_4O_{15}$(s). The $C_{p,m}$ of $Sr_5Nb_4O_{15}$(s) at 298 K is compared in the Table 4. Table 4 indicates that all values are in good agreement with each other.

Table 4. Heat capacity of $Sr_5Nb_4O_{15}$(s) at 298 K.

Compound	$C_{p,m}$ (J·mol^{-1}·K^{-1}) at 298 K		
	Own data	Ref.[10]	NKR
$Sr_5Nb_4O_{15}$	477.8	478.5	491.1

3.4. Enthalpy of Formation using High Temperature Oxide Melt Solution Calorimetry

Standard molar enthalpy of formation of $Sr_5Nb_4O_{15}$(s) sample was derived from the enthalpy of dissolution data of the compound and its component oxides viz., SrO(s) and Nb_2O_5(s) in molten PbO+B_2O_3 (2:1 molar ratio) solvent maintained at 966 K.

The molar enthalpy of dissolution of SrO(s) was obtained indirectly using a separate thermochemical cycle employing enthalpy of dissolution of its carbonates $SrCO_3$(s).

The details of the experimental measurements have been described elsewhere [13]. For sake of clarity, a schematics of the calorimeter is given in the Figure 6.

Table 5 gives the thermochemical cycle for derivation of standard molar enthalpies of dissolution of SrO(s, 298 K).

The enthalpies of decomposition of $\Delta_{decom}H$($SrCO_3$) are -234.3 kJ·mol^{-1}. The value of enthalpy increment of CO_2(g) was taken from literature and is equal to 32 kJ·mol^{-1}[16].
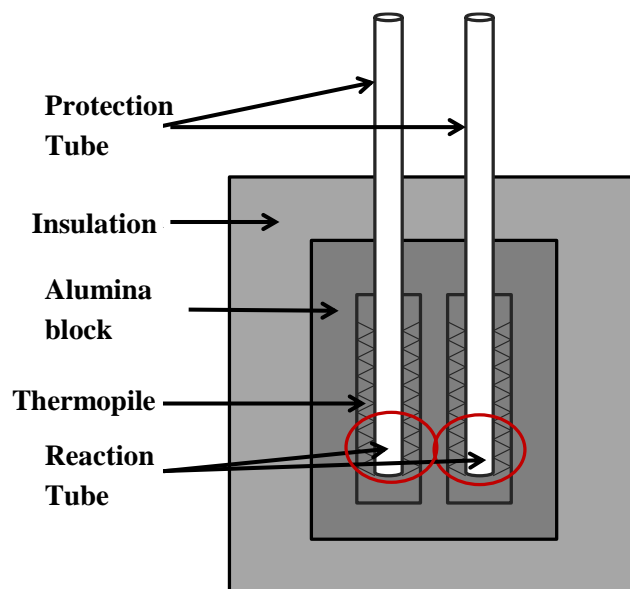

Figure 6. Schematic of high-temperature Calvet-type solution calorimeter (Alexsys-1000, make SETARAM, France).

Table 5. Standard molar enthalpies of dissolution of SrO(s, 298K); sol= molten PbO + B_2O_3 (2:1) solvent at 966 K; $\Delta_{ds}H^o_{298}$(MO)= ΔH_1 + ΔH_2 +ΔH_3.

Reactions	ΔH_i	Ref.
$SrCO_3$(s, 298 K)+sol(T K)= (SrO)sol(T K) + CO_2(g,T K)	ΔH_1	This Work
SrO(s, 298 K) + CO_2(g, 298 K)= $SrCO_3$ (s, 298 K)	ΔH_2	Ref. [16]
CO_2(g, T K)= CO_2(s, 298 K)	ΔH_3	Ref.[16]
SrO(s, 298 K)+sol(T K) = (SrO)$_{sol}$(T K)	$\Delta_{ds}H^o_{298}$	This Work

Enthalpy increments for carbonates are measured at the same experimental temperature and are used for the calculation. The enthalpy of solution of SrO, when added from 298.15 K, $\Delta_{ds}H$(SrO), also known as enthalpy of drop solution, is calculated to be -59.5 kJ·mol^{-1}. The enthalpy of solution of the $Sr_5Nb_4O_{15}$(s) in liquid PbO + B_2O_3 (2:1) solvent at 966 K at infinite dilution was measured for few successive additions and presented in Table 6. In our earlier publication, we have reported the enthalpy of solution of Nb_2O_5 in lead borate solvent for the first time and details is given in ref [17]. During each dissolution experiment, the solvent to solute ratio was maintained so that infinite dilution condition is sustained. The values of enthalpies of drop solution of $Sr_5Nb_4O_{15}$(s) from 298 K cited in Table 6, are random in nature which indicates the absence of composition dependence and significant dilution effect.

The enthalpies of drop solution of SrO and Nb_2O_5, obtained in present experiment and other literature data using lead borate solvent are compared in Table 7.

Thermodynamic cycles were constructed to calculate the enthalpy of formation of $Sr_5Nb_4O_{15}$ from the elements and are presented in Table 8.

Table 6: The molar enthalpy of dissolution of Sr$_5$Nb$_4$O$_{15}$(s) in molten PbO+B$_2$O$_3$ (2:1 molar ratio) solvent maintained at 966.1 ± 0.1 K and P =0.1 MPa; $\Delta_{ds}H_m$ = molar enthalpy of drop solution.

Solute	Mass /mg	$\Delta_{ds}H$ /kJ·mol^{-1}
Sr$_5$Nb$_4$O$_{15}$ (s)	13.03	323.0
Mol. Mass	13.06	326.1
=1049.72 g·mol^{-1}	13.22	324.3
	14.95	321.9
	17.24	329.8
	14.50	325.5
		Mean: 324.8 ± 3.5

Table 7. Comparison of enthalpy of drop-solution ($\Delta_{ds}H$) of SrO and Nb$_2$O$_5$ in lead borate solvent. The error is twice the standard deviation of the mean.

	$\Delta_{ds}H$/kJ·mol^{-1} in (2PbO+B$_2$O$_3$) solvent	
	This study	Literature
SrO	-59.5 ± 1.7 at 966 K	-60.5 ± 2.0 at 975 K [21]
Nb$_2$O$_5$	66.6± 1.9 at 966 K	-

Table 8. Thermodynamic cycles for the standard molar enthalpy of formation ($\Delta_f H^o_m$ at 298 K) of Sr$_5$Nb$_4$O$_{15}$ (s) from elements.

Reactions	ΔH (kJ·mol^{-1})
Sr$_5$Nb$_4$O$_{15}$ (s, 298 K) → 5SrO (dis, 966 K) + 2Nb$_2$O$_5$ (dis, 966 K)	ΔH_1=324(±5)
SrO (s, 298 K) → SrO (dis, 966 K)	ΔH_2 = -58(±2)
Nb$_2$O$_5$ (s, 298 K) → Nb$_2$O$_5$ (dis, 966 K)	ΔH_3= 68(±2)
Sr (s, 298 K) + 0.5O$_2$ (g, 298 K) → SrO (s, 298 K)	ΔH_4 = -592(±1)^a
2Nb (s, 298 K) + 2.5O$_2$ (g, 298 K) → Nb$_2$O$_5$ (s, 298 K)	ΔH_5 = -1899(±2)^a
5Sr (298 K) + 4Nb (298 K) + 7.5O$_2$ (298 K) → Sr$_5$Nb$_4$O$_{15}$ (s,298 K)	$\Delta_f H^0_m$(298 K)
Hence, $\Delta_f H^0_m$(298 K) = − ΔH_1 + 5 ΔH_2 + 2ΔH_3 + 5ΔH_4 + 2ΔH_5	**-7236(±7)**

The $\Delta_f H^0_m$(298.15 K) of the compound from the elements is -7236±7 kJ·mol^{-1}. Enthalpy of formation of the component oxides, SrO(s) and Nb$_2$O$_5$(s) are taken from ref. [16]. The Gibbs energy of formation was calculated using our enthalpy of formation and entropy of formation at 298 K.

$$\Delta_f G^0_{298}(Sr_5Nb_4O_{15}(s)) = \Delta_f H^0_{298} - 298 \times 0.001 \times \Delta_f S^0_{298}$$
$$= - 6808.4 \text{ kJ·mol}^{-1} \quad (14)$$

The standard molar enthalpy of formation of Sr$_5$Nb$_4$O$_{15}$(s) with respect to the constituent oxides (i.e., SrO and Nb$_2$O$_5$) at 298 K is found to -478 kJ·mol^{-1}. This indicates that Sr$_5$Nb$_4$O$_{15}$ (s) is relatively more stable compared to its binary oxides.

4. Thermal Function of the Sr$_5$Nb$_4$O$_{15}$ Compound

The basic function such as $C^o_{p,m}(T)$, {$H^o_m(T)$-H^o_m(298.15 K)} and {$S^o_m(T)$- S^o_m(298.15 K)} as a function of temperature are incorporated in the thermodynamic table as shown in Table 9. The smoothed values of measured heat capacity at regular interval of temperature were used to estimate the standard molar entropy and enthalpy for Sr$_5$Nb$_4$O$_{15}$(s). The standard molar entropy and enthalpy for

Sr$_5$Nb$_4$O$_{15}$ (s) are related to heat capacity as per the relation (15) and (16) respectively.

$$S^0_{TK}(Sr_5Nb_4O_{15}) - S^0_{298\,K}(Sr_5Nb_4O_{15})$$
$$= \int^{TK}_{298K}(C_p^0(Sr_5Nb_4O_{15})/T)\,dT \quad (15)$$

$$\Delta H^0_{TK}(Sr_5Nb_4O_{15}) - \Delta H^0_{298\,K}(Sr_5Nb_4O_{15})$$
$$= \int^{TK}_{298K} C_p^0(Sr_5Nb_4O_{15})\,dT \quad (16)$$

The calculated values of these thermodynamic functions have been presented in Table 9 and have an uncertainty of within ±2–3%. The gradual increase of values of the entropy and enthalpy with temperature, indicate the absence of any magnetic and phase transition of the compound. The standard molar entropy of Sr$_5$Nb$_4$O$_{15}$(s) was taken from the literature [16]. Free energy function (Fef) for compound can be derived using the following Eq. (16):

$$Fef= -[(H^0_T - H^0_{298})/T] + S^0_T \quad (17)$$

The Free energy function (Fef) of the compound also listed in Table 9 as a function of temperature. Uncertainties for thermodynamic functions were calculated as twice the standard deviation (±2σ) of the experimental values.

Table 9. Thermodynamic functions for the compound Sr$_5$Nb$_4$O$_{15}$(s).

T/K	Fitted C^o_p /J·K^{-1}·mol^{-1}	(H^o_T − $H^o_{298.15}$) /kJ·mol^{-1}	(S^o_T − $S^o_{298.15}$) /J·K^{-1}·mol^{-1}	Fef /J·K^{-1}·mol^{-1}
298	477.7	0	0	524.50
300	478.9	1.0	3.19	524.22
400	521.9	56.3	147.45	531.15
500	549.6	116.4	267.06	558.67
600	571.2	180.4	369.23	593.02
700	589.9	247.8	458.71	629.15
800	607.1	318.5	538.62	665.01
900	623.4	392.3	611.08	699.75
1000	639.2	469.1	677.58	733.04

5. Conclusions

Standard enthalpy of formation of Sr$_5$Nb$_4$O$_{15}$(s) is determined employing oxide melt solution calorimeter for the first time and is found to be -7236 ± 8 kJ·mol^{-1}. The enthalpy of formation calculated at 965 K from mass spectrometric is found to be -7075 kJ·mol^{-1}. Both the values are in good agreement with each other. The molar heat capacity of the Sr$_5$Nb$_4$O$_{15}$(s) is measured using DSC. The standard molar heat capacity of Sr$_5$Nb$_4$O$_{15}$(s) derived from the DSC experiment are compared with the values reported by ref.[12]. Smoothed heat capacities values are used for the calculation of the thermodynamic table. The values of standard thermodynamic functions for Sr$_5$Nb$_4$O$_{15}$ at T = 298 K are: $C^o_{p,m}$(298 K) = 477.7 J·K^{-1}·mol^{-1}; $\Delta_f H^o_m$(298 K) = -7236 kJ·mol^{-1}; $\Delta_f G^o_m$ (298 K) = - 6808 kJ·mol^{-1}; *fef* (298 K) = 524.5 J·K^{-1}·mol^{-1}. Therefore, this data are important for assessment of fission product interactions and for modeling of fuel thermodynamics which plays an important role in predicting long term stability of these materials under different reactive conditions. Enthalpy of formation and Gibbs energy formation data for this compound would be

useful for predicting the stability of the compound in different physico-chemical conditions.

Nomenclature

$\Delta_f G^o_m$	Molar Gibbs Energy of formation (kJ·mol^{-1})
$\Delta_f H^0_m$	Molar Enthalpy of formation (kJ·mol^{-1})
$\Delta_{ds} H$	Molar Enthalpy of dissolution (kJ·mol^{-1})
$\{H^o_m(T) - H^o_m(298\ K)\}$	Enthalpy Increment (kJ·mol^{-1})
Fef	Free energy function (J·K^{-1}·mol^{-1})
$C^o_{p,m}$	Molar heat capacity at constant pressure (J·K^{-1}·mol^{-1})
M	Molar mass (g·mol^{-1})
T	Temperature (K)
S	Entropy (J·K^{-1}·mol^{-1})
P	Pressure (Pa)
$\Delta_r H^o$	Enthalpy of reaction (kJ·mol^{-1})
K_{inst}	Instrumental Constant
I^+_i	Ion current in ampere
σ_i	Electron impact ionization cross-section
a_i	Isotopic abundance of the specific ion.
p_i	Partial pressure

References

[1] F. Galasso, L. Katz, "Preparation and Structure of Ba$_5$Ta$_4$O$_{15}$ and Related Compounds," *Acta. Cryst., 14,* 647-651, 1961.

[2] H. Sreemoolanadhan, J. Lsaac, S. Solomon, M.T. Sebastian, K.A. Jose, P. Mohanan, "Dielectric Properties of Ba$_5$Nb$_4$O$_{15}$ Ceramic," *Phys. Status Solidi., 143*, 45-49, 1995.

[3] H. Sreemoolanadhan, M.T. Sebastian, P. Mohanan, "High Permittivity and Low Loss Ceramics in the BaO-SrO-Nb$_2$O$_5$ System," *Mater. Res. Bull., 30,* 653-658, 1995.

[4] G. Zhu, Z. Ci, C. Ma, Y. Shi, Y. Wang, "A Novel Red Emitting Phosphor of Eu^{3+} Doped TTB-type Niobate NaSr$_2$Nb$_5$O$_{15}$ for White Leds,". *Mater. Res. Bull.*, *48,* 1995–1998, 2013.

[5] Y. Miseki, H. Kato, A. Kudo, "Water Splitting into H$_2$ and O$_2$ over Niobate and Titanate Photocatalysts with (111) Plane-type Layered Perovskite Structure," *Energy Environ. Sci.*, *2*, 306–314, 2009.

[6] C.D. Whiston, A.J. Smith, Double Oxides Containing Niobium or Tantalum. II. Systems involving Strontium or Barium; *Acta. Cryst. 23*, 82-85, 1967.

[7] M. Weiden, A. Grauel, J. Norwig, S. Horn, F. Steglich, "Crystalline Structure of the Strontium Niobates Sr$_4$Nb$_2$O$_9$ and Sr$_5$Nb$_4$O$_{15}$," *J. Alloy Compd., 218,* 13-16, 1995.

[8] "The Materials Project. Materials Data on Sr$_5$Nb$_4$O$_{15}$," by Materials Project. United States: N. p., 2020. Web. doi:10.17188/1291746.

[9] I.N. Jawahar, P. Mohanan, M.T. Sebastian, "A$_5$B$_4$O$_{15}$ (A=Ba, Sr, Mg, Ca, Zn; B=Nb, Ta) microwave dielectric ceramics," *Mater. Lett., 57,* 4043-4048, 2003.

[10] J. R. Carruthers and M. Grasso, "Phase Equilibria Relations in the Ternary System BaO- SrO- Nb$_2$O$_5$;" *J. Electrochem. Soc., 117,* 1426-1430, 1970.

[11] Y. Yang, Yu H Jin, "Thermodynamic Calculation of the SrO-Nb$_2$O$_5$ System," *J. Mater. Sci. Technol., 15,* 203-207, 1999.

[12] J. Leitner, I. Sipula, K. Ruzica, D. Sedmidubsky, P. Svoboda, "Heat Capacity, Enthalpy and Entropy of Strontium Niobates Sr$_2$Nb$_{10}$O$_{27}$ and Sr$_5$Nb$_4$O$_{15}$;" *J. Alloys Compd., 481,* 35-39, 2009.

[13] S.K. Rakshit, S.C. Parida, Kristina Lilova, Alexandra Navrotsky, "Thermodynamic studies of CaLaFe$_{11}$O$_{19}$(s)," *J. Solid State Chem., 20,* 68-74, 2013.

[14] T.D. Mark and E. Hille, "Cross section for single and double ionization of carbon dioxide by electron impact from threshold up to 180 eV;" *J. Chem. Phys., 69,* 2492-2498, 1978.

[15] G.W.H. Hohne, W.F. Hemminger, H.J. Flammershein, (2003), "Differential Scanning Calorimetry," second ed., Springer, Berlin.

[16] Barin I., (1995), "Thermochemical Data of Pure Substances," vol. I & II, 3rd ed., VCH Publishers, New York,.

[17] P. Samui, B.M. Singh, H.V. Khadilkar, S.K. Rakshit, S.C. Parida; "Thermodynamic Studies on Ba$_3$SrNb$_2$O$_9$ Employing Calorimeter," *Int. J. Thermodyn., 24,* 50-55, 2021.

[18] M.W. Chase Jr., "JANAF thermochemical tables," fourth ed, Monograph no. 9, J. Phys. Chem. Ref. Data 311-480, 1995.

[19] PCPDFWIN Version 2.2, Joint Committee on Powder Diffraction Standards, JCPDS XRD file No. 00-048-0421.

[20] J. Leitner, M. Nevriva, D. Sedmidubsky, P. Vonka, "Enthalpy of formation of selected mixed oxides in a CaO–SrO–Bi$_2$O$_3$–Nb$_2$O$_5$ system," *J. Alloy Compd., 509,* 4940-4943, 2011.

[21] B. Joseph, A. Navrotsky, D. Joseph, "Energetics of La$_{2-x}$Sr$_x$CuO$_{4-x}$ Solid Solutions ($0.0 < x < 1.0$)," *J. Solid State Chem., 93,* 418-429, 1991.

Research Article

The Bosons of the Conventional Superconductors

*U. Köbler

Research Center Jülich, Institute PGI, D-52425, Jülich, Germany
E-mail: u.koebler@fz-juelich.de

Abstract

For the conventional superconductors it will be shown that not only the superconducting energy gap, $E_{gap}(T=0)$, and the critical field, $B_c(T=0)$, but also the London penetration depth, $\lambda_L(T=0)$, scale in a reasonable approximation with the superconducting transition temperature, T_{SC}, as $\sim T_{SC}$, $\sim T_{SC}^2$ and $\sim T^{-1/2}$, respectively. From these scaling relations the conclusion obtained earlier, using a completely different method, is confirmed that the London penetration depth corresponds to the diameter of the Cooper-pairs. As a consequence, only one layer of Cooper pairs is sufficient to shield an external magnetic field completely. The large diamagnetism of the superconductors is caused by the large orbital area of the Cooper-pairs. From the fact that, in the zero-field ground state, the temperature dependence of the superconducting heat capacity is given above and below T_{SC} by power functions of absolute temperature it follows that the only critical point is T=0. The superconducting transitions of the element superconductors, therefore, are all within the critical range at T=0. As a consequence, above and below T_{SC} there is short-range order only. As we know from Renormalization Group (RG) theory, in the critical range the dynamics is the dynamics of a boson field, exclusively. Evidently, the Cooper-pairs have to be considered as the short-range ordered units created by this boson field. It is reasonable to assume that the relevant bosons in the superconducting state are identical with the bosons giving rise to the universal linear-in-T electronic heat capacity above T_{SC}. Plausibility arguments will be given that these bosons must be electric quadrupole radiation generated by the non-spherical charge distributions in the soft zones between the metal atoms. The radiation field emitted by an electric quadrupole can be assumed to be essentially curled or circular. In the ordered state below T_{SC}, the bosons are condensed in resonating spherical modes which encapsulate the two Cooper-pair electrons and shield their charge perfectly.

Keywords: Cooper-pairs; ordered boson fields; stimulated emission.

1. Introduction

The postulation of Cooper pairs [1] marks a historical breakthrough in our understanding of the phenomenon of superconductivity. However, the detailed nature of the coupling mechanism between the two Cooper-pair electrons is still unclear [2-8]. Further experimental information on the properties of the Cooper-pairs, such as the temperature dependence of their size and their density, therefore, is of vital importance. The present study aims to contribute in a rather phenomenological way to the solution of these problems. A final confirmation of the here advanced ideas must come from field-theoretical studies.

It is evident that at the superconducting transition temperature, T_{SC}, Cooper-pairs get formed and are responsible for the two prominent superconducting properties: a vanishing electrical resistivity and the emergence of a huge diamagnetism (Meissner-effect) [1]. Formation of Cooper-pairs at T_{SC} reminds on the formation of domains at the magnetic ordering temperature. In fact, Cooper-pairs and domains have to be considered as the characteristic ordered units with linear dimensions of much larger than the inter-atomic distance. As a consequence, domains and Cooper-pairs cannot result from atomistic short-range interactions. In order to illustrate the similarities and differences between the magnetic domains and the Cooper-pairs, it is useful to discuss first the better understood magnetic domains.

Quite generally, at virtually all order-disorder phase transitions a boson field orders [9,10]. The visible atomic or magnetic order results from a coupling of the atoms or spins to the ordered boson field. Essential for a long-range and coherent order of a boson field is that the emission characteristics of the individual boson source is axial and that the bosons get generated by stimulated emission. These conditions hold for the bosons that order at the magnetic ordering transition [9]. It could be shown that these bosons are magnetic dipole radiation generated by the precessing spins [11]. We have called these bosons, in honor of J. Goldstone, Goldstone-bosons [12,13]. Due to stimulated emission the bosons get collimated along those crystallographic directions with a high density of the boson sources and, eventually, condense in a single quantum state. In the ordered state of the Goldstone-boson field, all bosons are in a one-dimensional, perfectly coherent and long-range ordered state. This is realized in each magnetic domain. The reduction from a spatially isotropic propagation of the bosons to a few propagation directions is an example of broken symmetry. In fact, stimulated emission seems to be an important origin of the phenomenon of broken symmetry [12].

The ordered boson field has a well-defined, self-organized, spatially limited contour. In the magnetic case this are the well-known domains. The domains result from a self-constriction mechanism of the ordered boson field and define the limits of a region with homogenously ordered spins. They are self-contained units. The ordered spins are, so to say, enclosed in the domain. Moreover, the domains have the functionality of a resonator. Within each domain, bosons and magnons are standing plane waves. The dynamics in the individual domain, therefore, is perfectly one-dimensional. The one-dimensionally ordered structure is a consequence of the axial radiation characteristics of the individual boson source, i.e., the precessing spin. As a result, for many magnets, the observed magnon dispersions are as for the linear spin chain, independent of the assumed locally anisotropic exchange interactions that are not relevant in the critical range above the ordering temperature and for all lower temperatures as well [14,15]. A three-dimensional dynamic symmetry results by a coupling of the one-dimensional boson fields of the domains along x-, y-, and z-axis. The observed critical exponents are defined by the dimensionality of the global boson field [15].

The superconducting transition is particular in that it is a transition into a state with a short range ordered boson field. The ordered units generated by these bosons are the Cooper-pairs. In contrast to the magnetic domains that are weakly fixed to the crystal lattice, the Cooper-pairs can move without any resistance across the metal [16]. The fact that there is no correlation between the positions of the Cooper-pairs conforms to the short-range order in the superconducting state. While the surface of the magnetic domains consists of planes, the shape of the Cooper-pairs must be rather spherical. A resistivity-free propagation mode of the Cooper-pairs is surprising in view of the two-fold electric charge of the Cooper-pair. Evidently, the boson resonator surrounding the two Cooper-pair electrons shields the charge of the two electrons perfectly against all other charges of the metal. There are good reasons to assume that the condensed bosons in the superconducting state are identical with the bosons giving rise to the universal linear-in-T electronic heat capacity above T_{SC}. We will call the bosons of the continuous metallic solid CMS-bosons [17]. At T_{SC}, these bosons change the type of short-range order and assume a definite shape below T_{SC}. It is suggestive to identify the CMS-bosons with electric quadrupole radiation generated by the anisotropic charge distributions in the rather soft zones between the metal atoms. One experimental observation supporting this idea is the strong dependence of T_{SC} upon application of an external pressure [18]. It is evident that application of pressure leads to deformations of the mechanically soft zones between the metal atoms and therefore to changes of the quadrupole moments. This has a direct effect on the generation process of the CMS-bosons, and, as a consequence, on T_{SC}. Note that the ordering transition of a boson field occurs for a sufficiently high density of identical bosons [9].

The Cooper-pairs behave as a dense gas of neutral particles [16]. Possibly, the mobility of the Cooper-pairs is by tunnel effect. In recently performed new analyses of published superconducting heat capacity data of the conventional superconductors, low-temperature crossover events were identified that could be interpreted as Bose-Einstein (B-E) condensation of the Cooper-pairs [16]. From the observed B-E condensation temperature, T_{BE}, it is possible to obtain the density, n, of the Cooper-pairs at T_{BE}

according to $T_{BE} \sim n^{2/3}$ [19]. The observed T_{BE} temperatures turned out to scale, to a good approximation, with the superconducting transition temperature, T_{SC}, as $T_{BE} = 0.135 \cdot T_{SC}$ [16]. As a consequence, the density of the Cooper-pairs at T_{BE} scales with the superconducting transition temperature, T_{SC}, as $n(T \sim 0) \sim T_{SC}^{3/2}$ [16]. Since T_{BE} is much lower than T_{SC}, the density of the Cooper-pairs at T_{BE} can be taken as representative of the density at T=0. Assuming that at all temperatures the Cooper-pairs form a dense-packed gas of bosons with a spin of S=0, their diameter at T~0, $\lambda(T \sim 0)$ is given by $\lambda(T \sim 0) \sim n^{-1/3} \sim T_{SC}^{-1/2}$.

Interestingly, the same scaling relation as for the diameter of the individual Cooper-pair, $\lambda(T \sim 0) \sim T_{SC}^{-1/2}$, holds for the London penetration depth, $\lambda_L(T \sim 0) \sim T_{SC}^{-1/2}$ (see Figure 2 below). The diameter of the Cooper-pair, therefore, corresponds to the London penetration depth. In other words, only one layer of Cooper-pairs, next to the inner surface of the superconductor, is sufficient to shield an applied magnetic field completely. As a consequence, the diamagnetic moment of the individual Cooper-pair, i.e., its cross-section area, is given by the square of the London penetration depth. As the experimental data show, the London penetration depth, λ_L, is divergent at T_{SC} and decreases strongly with decreasing temperature towards a finite value for T→0 (see Figures 5-7 below) [20]. We can assume that the proportionality $\lambda_L \sim \lambda$ holds for all temperatures. As a consequence, the diameter of the individual Cooper-pair decreases with decreasing temperature, in proportionality to the London penetration depth. This allows one to obtain the temperature dependence of the Cooper-pair diameter from measurements of the temperature dependence of the London penetration depth. The decreasing diameter of the Cooper-pairs is indicative of an increasing binding energy between the two Cooper-pair electrons. This is certainly a dynamic, i.e., temperature-dependent effect and has to be ascribed to a constricting force, inherent to the condensed boson shield that surrounds the two Cooper-pair electrons. In fact, there is a reasonable proportionality between the Cooper pair coupling energy, given by the gap energy $E_{gap}(T)$, and the reciprocal London penetration depth $\lambda_L^{-1}(T)$ (compare Figure 4 and Figure 5 below). In other words, the larger the coupling energy, $E_{gap}(T)$, is, the lower is the diameter of the Cooper-pair. The condensed boson shell surrounding the two Cooper-pair electrons has the functionality of a cage that exerts the necessary force, needed to counteract the electrostatic repulsion between the two electronic charges. Due to an increasing constricting force of the boson cage with decreasing temperature, the size of the Cooper pairs decreases with decreasing temperature, in parallel to the London penetration depth [16]. This "electrostriction" has some similarity with the spontaneous magnetostriction in the ordered magnets [21]. In both cases the constricting forces are a dynamic property of the ordered boson field. However, magnetostriction acts on the collective of a nearly constant configuration of dense packed domains and lets the lattice parameter decrease with decreasing temperature [21]. The corresponding electrostriction acts on each of the increasing number of Cooper-pairs and has little effect on the temperature dependence of the lattice parameter [22].

The decreasing size of the Cooper-pairs with decreasing temperature gets compensated by a corresponding increase of their density such that the volume of the superconductor is always completely filled with Cooper-pairs, similar to the volume of the ordered magnets that is completely filled with

domains. A complete filling seems to be specific to a homogeneous phase. The increasing number of electrons, needed for the increasing number of Cooper-pairs, can be assumed to be delivered by the conduction band. The superconducting system thereby gains an increasing mass which is certainly of importance on the superconducting dynamics, i.e., on the temperature dependence of the superconducting heat capacity [10,16]. At the same time, the conduction band gets depleted and the lattice parameter increases [22]. As a consequence, the superconductors resemble a two-phase system with the Cooper-pairs as the condensed phase and the conduction electrons as the vapor phase. The Cooper-pairs correspond, so to say, to the droplets in a vapor-liquid mixture.

Even in the limit $T \rightarrow 0$ where the London penetration depth and the diameter of the Cooper-pairs have a minimum, the orbital diamagnetism of the Cooper-pairs is sufficiently large such that, in the superconductors of the first kind, only one layer of Cooper-pairs at the inner surface of the superconductor shields a magnetic field completely. For the superconductors of the second kind, the low-temperature diameter of the Cooper-pairs, and therefore the orbital diamagnetism seems not to be sufficient to shield an applied magnetic field completely. The applied magnetic field then penetrates the superconductor as vortices.

Very peculiar is that the zero-field heat capacities of the conventional superconductors exhibit no critical behavior at T_{SC} but the Cooper-pair binding energy, $E_{gap}(T)$, and the London penetration depth, $\lambda_L(T)$, show critical behavior at $T=T_{SC}$ (see Figures 4-7 below), as it is familiar for the spontaneous magnetization [21,23] and for the magnon gap in the ordered magnets [21,24]. The typical critical power functions of the argument $|T_{SC}-T|$ are absent in the zero-field heat capacity of the conventional superconductors. Note that $E_{gap}(T)$ and $\lambda_L(T)$ are quantities that are not specific to the dynamics of the ground state of the unperturbed superconductor. Observation of these quantities requires special excitation conditions. As the finite critical range at T_{SC} and at $T=0$ shows, the temperature dependence of $E_{gap}(T)$ and $\lambda_L(T)$ is controlled by a long-range ordered boson-field that, apparently, has a higher dispersion energy than the bosons that are responsible for the dynamics of the superconducting ground state. As a consequence, there seem to exist two boson types in the superconductor. Only one of them can be relevant. The excited state bosons are, evidently, not relevant for the dynamics of the superconducting ground state and appear to be completely absent in zero-field measurements. For the ground state bosons $T=0$ is the only critical point. These bosons are in a short-range ordered state. The complicated temperature dependence of the superconducting zero-field heat capacity is another indication of a complicated excitation spectrum of the superconducting elements [10,16]. Note that there can be an interaction between thermally not occupied excited states and the thermally occupied ground state. This interaction can modify the dynamics of the ground state.

A possible explanation of the existence of two boson types could be that the radiation field emitted by an electric quadrupole is rather complicated. It is possible that this radiation field includes a linear and a curled component. In the superconducting state, the linear component is long-range ordered but not relevant for the dynamics of the ground-state. The heat capacity of this boson field is responsible for the temperature dependence of $E_{gap}(T)$ and $\lambda_L(T)$, in particular for the critical behavior of the two

quantities at T_{SC} in addition to $T=0$. In the ordered state, the curled component gives the Cooper-pairs their spherical shape. Due to the exclusion principle of relevance, the binding mechanism of the two Cooper-pair electrons seems to be decoupled from the dynamics of the Cooper-pairs in the zero-field ground state. The Cooper-pairs are rather stable objects. No critical behavior at T_{SC} is observed not only in the zero-field heat capacity but also for the critical field, B_c [25].

In the first part of this communication, we discuss the relation between the zero-temperature values of the Cooper-pair gap energy, $E_{gap}(T=0)$, of the London penetration depth, $\lambda_L(T=0)$, and of the critical field, $B_c(T=0)$ of the superconducting elements [26]. As is well-known, the Cooper-pair gap energy, $E_{gap}(T=0)$ and the critical field $B_c(T=0)$ scale to a good approximation with the superconducting transition temperature, T_{SC}, as $E_{gap}(T=0) \sim T_{SC}$ [1] and $B_c(T=0) \sim T_{SC}^2$ [25]. For the London penetration-depth the scaling relation will be shown to be $\lambda_L(T=0) \sim T_{SC}^{-1/2}$ [16]. From these scaling relations it follows conclusively that the diamagnetic moment of the Cooper pair, $\mu(T=0)$, is proportional to the square of the London penetration depth, i.e., $\mu(T=0) \sim \lambda_L^2(T=0) \sim T_{SC}^{-1}$. In other words, the Cooper-pairs are closed objects with a diameter that corresponds to the London penetration depth. The strong superconducting diamagnetism results from the large orbital area of the Cooper-pair wave function. The two Cooper-pair electrons are evidently in a spherical symmetric s-state. The antiparallel coupling of the spins of the two Cooper-pair electrons seems to be by the rather weak dipole-dipole interaction. The Cooper-pairs, therefore, receive a net magnetic moment in a rather low applied magnetic field and superconductivity breaks down at the moderate critical field, B_c [25].

In the second part of this work, representative data of the temperature dependence of the Cooper-pair gap energy, $E_{gap}(T)$, and of the reciprocal London penetration depth, $\lambda_L(T)^{-1}$, are analyzed. Typical of the long-range order of the boson field that controls the dynamics of the two quantities is that the complete temperature dependence of $E_{gap}(T)$ and of $\lambda_L(T)^{-1}$ is given by the two critical power functions at $T=0$ and at $T=T_{SC}$. This is as for the spontaneous magnetization of the ordered magnets [21,23]. As the identical critical exponents of $E_{gap}(T)$ and of $\lambda_L(T)^{-1}$ show, the two quantities are proportional to each other. In conformity with the increasing binding energy between the two Cooper-pair electrons as a function of a decreasing temperature, given by $E_{gap}(T)$, the diameter of the Cooper-pair orbital, i.e., $\lambda_L(T)$ shrinks.

2. Properties at T=0

As done by the BCS-theory [1], we make use of the empirical fact that the superconducting elements have similar electronic properties and differ essentially by their transition temperatures, T_{SC}, only. In this way it could plausibly be proven that the gap energy at $T=0$, $E_{gap}(T=0)$ is proportional to T_{SC} [1] and that the critical field $B_c(T=0)$ is proportional to T_{SC}^2 [25]. For the London penetration depth, it turns out that $\lambda_L(T=0)$ is proportional to $T_{SC}^{-1/2}$ (Figure 2) [16]. As a consequence, for a high T_{SC}, the Cooper-pairs are strongly bound and, as a consequence, are small objects with a small diameter given by λ_L.
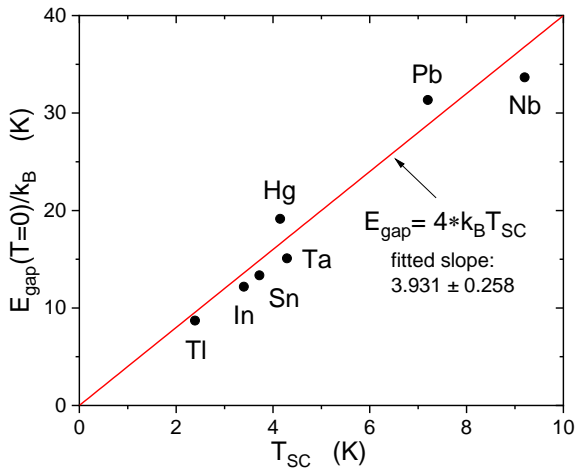
Figure 1. Experimental Cooper-pair gap energies at T~0, $E_{gap}(T=0)$, converted to temperatures for some superconducting elements as a function of the transition temperature, T_{SC} [26]. A linear fit of these data results reasonably into a slope of four, which deviates only slightly from the prediction of the BCS-theory of ~3.528 (see text) [20].
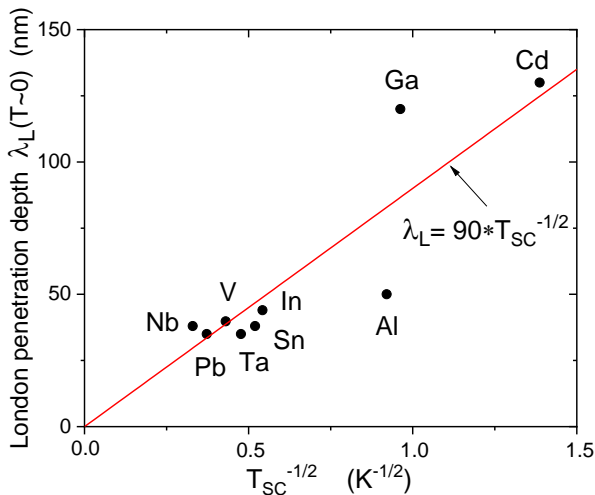

Figure 2. Experimental data of the London penetration depth at T~0, $\lambda_L(T=0)$, of some superconducting elements versus the reciprocal root of the superconducting transition temperature [26].

Figure 1 reproduces the famous proportionality between the gap energy at T=0 and T_{SC}. In Figure 1 the gap energies are converted to temperatures [26]. It can be seen, that $E_{gap}(T=0)/k_B$ is to a good approximation proportional to T_{SC}, as predicted by the BCS-theory [1]. A linear fit of the data in Figure 1 results in a proportionality constant of 3.931 ± 0.258 which is somewhat larger than ~3.528 predicted by the BCS-theory [1,20]. It seems justified to consider the fit result for the proportionally constant as consistent with four, although 3.5 cannot be excluded.

Considering the gap energy as the thermodynamic stability limit of the Cooper-pairs and that T_{SC} defines the temperature scale, one can, formally, consider $E_{gap}(T=0)$ as a multiple of $1/2 \cdot k_B T_{SC}$. Note, however, that this proportionality does not mean a thermal equilibrium. In other words, the individual Cooper-pair has between 7 and 8 degrees of freedom. Since there are certainly three

translational degrees of freedom, the Cooper-pair has between 4 and 5 additional energy degrees of freedom. This could mean that the Cooper-pairs are not perfectly spherical in shape and/or have a number of internal degrees of freedom such as breathing or pump modes. According to the generally low superconducting transition temperatures it is clear that the two electrons of the Cooper pair are not rigidly bound to each other. In fact, as the temperature dependence of $E_{gap}(T)$ shows, the coupling of the two Cooper-pair electrons is a dynamic process.

Another characteristic quantity of the superconductors is the low-temperature minimum of the London penetration depth, $\lambda_L(T=0)$, that gives the distance from the surface of the sample over which an external magnetic field can penetrate into the superconductor. Note that the penetration depth is divergent at T_{SC} and assumes a finite minimum for T→0 (see Figures 5-7 below) [20]. For T=0, the volume of the superconductor (of the first kind) is field-free, except for a thin layer at the surface with a thickness of $\lambda_L(T=0)$. It is evident that this phenomenon, known as Meissner-Ochsenfeld effect [27], is a direct consequence of the strong diamagnetism of the Cooper-pairs owing to their large orbital area. The strong diamagnetism is consistent with the view that the two electrons of the Cooper-pair can move on closed loops. They circulate the stronger, the larger the applied magnetic field is. The diamagnetic moment can be expected to be proportional to the applied magnetic field. Note that in the normal-conducting state there are no Cooper-pairs. Most conventional superconductors are paramagnetic in the normal state. Figure 2 shows experimental data of the London penetration depth at T~0 as a function of the square root of the reciprocal transition temperature, $T_{SC}^{-1/2}$ [26]. From this data representation it follows that, the lower the transition temperature is, the larger is the penetration depth for a magnetic field. Eventually, for T_{SC}→0, the penetration depth, $\lambda_L(T=0)$, diverges and the superconductor does no longer shield the magnetic field. This proves consistently that the strong diamagnetism is restricted to the superconducting state. It is evident that for a low T_{SC}, the two electrons of the Cooper-pair are weakly coupled only and the size of the Cooper-pair orbital is correspondingly large. The London penetration depth then is correspondingly large as well. In other words, the T=0 values of the London penetration depth and of the size of the Cooper pairs increase with decreasing T_{SC}.

Another characteristic quantity of the conventional superconductors is the critical field at T=0, $B_c(T=0)$. As is well-known, $B_c(T=0)$ scales with the square of the transition temperature (Figure 3) [25]. The relation $B_c(T=0)\sim T_{SC}^2$ is satisfactorily confirmed by the data representation of Figure 3 [26].

The three quantities $E_{gap}(T=0)$, $\lambda_L(T=0)$ and $B_c(T=0)$ are certainly not independent of each other. In order to find out a correlation between them we make use of the formal energy equation

$$\mu(T=0)\cdot B_c(T=0)=E_{gap}(T=0) \qquad (1)$$

with $\mu(T=0)$ as diamagnetic moment of the Cooper-pair orbital at T=0 for an applied magnetic field of $B_c(T=0)$. Inserting into equation (1) the two relations:

$$B_c(T=0)\sim T_{SC}^2 \quad \text{(Figure3) and}$$
$$E_{gap}(T=0)\sim T_{SC} \quad \text{(Figure 1)} \qquad (2)$$

it results that $\mu(T=0) \sim T_{SC}^{-1}$. Considering that the London penetration depth is $\lambda_L(T=0) \sim T_{SC}^{-1/2}$ (Figure 2) it follows that

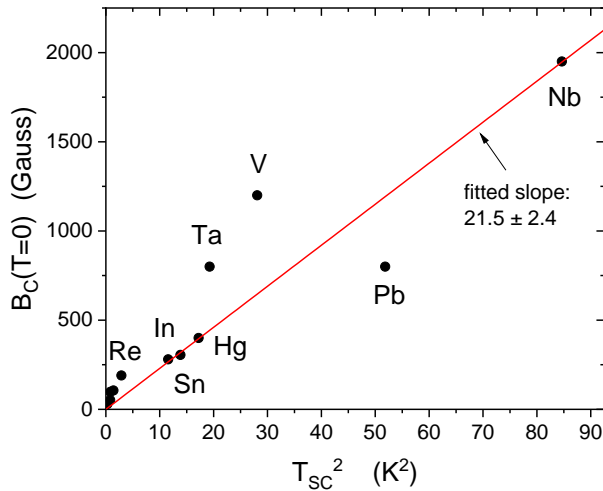$$\mu(T=0) \sim \lambda_L(T=0)^2 \qquad (3)$$

Figure 3. The critical field at $T \sim 0$, $B_c(T=0)$, *as a function of the superconducting transition temperature squared for a selection of superconducting elements* [25,26].

As a consequence, the diamagnetic moment μ of the Cooper-pair is proportional to the square of the London penetration depth. In other words, λ_L^2 gives the cross-section area of the Cooper-pair, and the diameter of the Cooper-pair is proportional to the London penetration depth, λ_L. This result provides a plausible microscopic explanation of the London penetration depth λ_L and supports the real-space, or particle picture of the Cooper-pair. As a consequence, only one layer of diamagnetic Cooper-pairs next to the inner surface of the superconductor is sufficient to shield the external magnetic field completely. The London penetration depth deceases as a function of a decreasing temperature because the Cooper-pair orbital area decreases as a function of a decreasing temperature. For the type I superconductors the minimum of the orbital area of the Cooper-pairs for $T \to 0$ and, as a consequence, the associated small diamagnetic moment is still sufficient to shield the applied magnetic field completely. On the other hand, a complete shielding of a magnetic field for all temperatures by only one layer of Cooper-pairs requires that the decreasing size of the Cooper-pairs, with decreasing temperature, gets compensated by a corresponding increase of their density such that the volume of the sample is always nearly completely filled with Cooper-pairs [16]. For the type II superconductors, either the orbital area or the density of the Cooper-pairs seems not to be sufficiently large to shield the magnetic field completely. The magnetic field then penetrates the superconductor as vortices.

The result expressed by the proportionality (3) agrees with a recent experimental study of the Bose-Einstein (B-E) condensation temperatures, T_{BE}, of the Cooper-pairs of the superconducting elements [16]. Note that Cooper-pairs are bosons with an integer spin of $S=0$ [2]. In spite of their two-fold charge, the Cooper-pairs can move completely freely across the metallic matrix, which is a condition for an electrical resistivity of zero of the superconducting current. This shows that the charges of the two Cooper-pair electrons get completely shielded by the surrounding CMS-boson

cage. As an empirical fact, the thermodynamics of the Cooper-pair gas can be described by the same algorithm as it applies to the dilute alkali-metal atom gases [19]. From the observation of the B-E condensation temperature, T_{BE}, it is possible to evaluate the density of the Cooper-pairs, n, at T_{BE}. For the uniform Bose gas, confined to a three-dimensional box, the dependence of T_{BE} on the density of the gas particles, n, is given by

$$k_B \cdot T_{BE} \approx 3.31 (\hbar^2 n^{2/3}/m) \qquad (4)$$

with $\hbar = h/2\pi$ as Planck constant and $m=2m_e$ as the mass of the Cooper-pair (m_e is the mass of the electron) [19]. Because of the low mass of the electron, the B-E condensation temperatures of the Cooper pairs are five to six orders of magnitude higher than for the alkali-atom condensates. However, in contrast to the dilute alkali-atom condensates the density of the Cooper-pairs is temperature dependent. As we have already argued, the density of the Cooper-pairs increases as a function of a decreasing temperature according to their decreasing size such that for all temperatures the volume of the superconductor is nearly completely filled with Cooper-pairs. In other words, the observed condensation temperature, T_{BE}, corresponds to the Cooper-pair density at T_{BE}. Since the T_{BE} values turned out to be proportional to T_{SC} as $T_{BE} \sim 0.135 \cdot T_{SC}$ [16] the density of the Cooper-pairs at T_{BE} can be taken as representative for the density at $T=0$.

The B-E condensation of the Cooper-pairs gives rise to a crossover event in the heat capacity of the superconductor [10,16]. Inserting the experimental scaling relation $T_{BE} = 0.135 \cdot T_{SC}$ into formula (4), the density of the Cooper pairs at T_{BE}, i.e., at $T \sim 0$, follows as

$$n(T=0) = 0.88 \cdot 10^{15} \cdot T_{SC}^{3/2} \qquad (5)$$

with n in units of cm^{-3} [16].

Another, completely independent estimate of the Cooper-pair density at $T=0$ is possible from the London penetration depth data in Figure 2, assuming that the Cooper pairs form a dense gas of particles with no significant distance between them. Under this condition, the distance between the Cooper-pairs corresponds to their diameter $\lambda_L(T \sim 0)$. The density of the Cooper pairs therefore is given by $n \sim \lambda_L^{-3}$. Using $\lambda_L(T=0) \sim T_{SC}^{-1/2}$ from Figure 2 it follows that $n(T=0) \sim T_{SC}^{3/2}$. As a consequence, the same relation $n(T=0) \sim T_{SC}^{3/2}$ results from two completely different experimental methods. Inserting $\lambda_L = 90 \cdot T_{SC}^{-1/2}$ (in nm) from Figure 2 into $n \sim \lambda_L^{-3}$ it follows that

$$n(T=0) = 1.37 \cdot 10^{15} \cdot T_{SC}^{3/2} \qquad (6)$$

with n in units of cm^{-3}. The pre-factor in equation (6) is larger by a factor of ~ 1.5 compared to the pre-factor in equation (5). This indicates that the assumption of no space at all between the Cooper-pairs is not perfectly correct and that the density of the Cooper-pairs is over-estimated, assuming that their distance corresponds to their diameter. Nevertheless, it seems to be a reasonable approximation that for all temperatures the available space in the superconductor is nearly completely filled with Cooper-pairs.

Using the fitted slopes in Figure 1 and Figure 3, an estimate of the diamagnetic moment of the Cooper pairs at $T=0$ for an applied magnetic field of $B=B_c(T=0)$ can be obtained. According to formula (1) the diamagnetic moment

of the Cooper pairs results as $\mu(T=0)=-2.8 \cdot 10^3 \mu_B/T_{SC}$, with μ_B as Bohr magneton. This surprisingly large diamagnetic moment is consistent with the view that for an applied field of $B_c(T=0)$ the two electrons of the Cooper-pair circulate with a high frequency on a closed loop. However, in view of the enormous diamagnetic moment obtained in this way, we cannot exclude that formula (1) is correct except for an unknown proportionality constant.

We should recall that in 1935 when F. and H. London proposed a theoretical explanation of the Meissner-Ochsenfeld effect [27,28,29], Cooper-pairs were unknown [1-8]. Using the free electron model of the metals, the strongly increasing diamagnetism of the superconductors with decreasing temperature had to be explained by a strong increase of the electron density, n_e, with decreasing temperature. In other words, no specific assumption on the superconducting electronic state was made. There is, however, neither a physical reason, nor some experimental evidence for such a strong temperature dependence of the electron density. It is clear that because of the large orbital diamagnetism of the Cooper-pairs, the shielding of an external magnetic field is much more efficient by Cooper pairs than by a gas of free electrons. According to the London theory, the relation between the density of the free electron gas, n_e, and the London penetration depth λ_L is given by [28,29]:

$$\lambda_L^2 = m_e/\mu_0 e^2 n_e \tag{7}$$

In formula (7), m_e is the mass of the electron, μ_0 is the vacuum permeability and e is the charge of the electron. Inserting $\lambda_L(T=0)=90 \cdot T_{SC}^{-1/2}$ (in nm) according to Figure 2 into formula (7), results for the electron density at T=0:

$$n_e(T=0)=3.48 \cdot 10^{21} \cdot T_{SC} \tag{8}$$

with n_e in cm^{-3}. Note that in contrast to the Cooper-pair density at T=0 that is proportional to $T_{SC}^{3/2}$, according to formula (6), the electron density at T=0 of the London theory is proportional to T_{SC}, according to formula (8). As a conclusion, the historical London theory explains the low penetration depth of a magnetic field for T→0 by an electron density of the assumed free-electron gas that is larger by a factor of ~10^6 compared to a Cooper-pair density that results into the same shielding effect (formula (5)).

In 1935, the importance of bosons for the dynamics of solids was unknown. This new chapter of solid-state physics began only in 1974 when the Renormalization-Group theory appeared [30]. Although RG-theory has restricted to the magnetic degrees of freedom, it became more and more clear that bosons are essential for the dynamics of all other degrees of freedom as well. In particular ordered boson fields are responsible for the generation of Cooper-pairs and magnetic domains.

3. Temperature Dependence of E_{gap} and λ_L

As we have already mentioned, in contrast to the critical field and the zero-field heat capacity which exhibit critical behavior at T=0 only, the Cooper-pair gap energy, $E_{gap}(T)$, and the reciprocal London penetration depth, $\lambda_L(T)^{-1}$, exhibit critical behavior additionally at $T=T_{SC}$, as it is known for the spontaneous magnetization and for the magnon gap of the ordered magnets [23,24,31]. Since we know that the temperature dependence of the two magnetic quantities is controlled by the heat capacity of the long-range ordered

Goldstone-boson field (magnetic dipole radiation), it can be concluded that the temperature dependence of $E_{gap}(T)$ and of $\lambda_L(T)^{-1}$ is controlled also by the heat capacity of a long-range ordered boson field. This boson field is evidently different from the boson field that is responsible for the temperature dependence of the zero-field heat capacity. For these low-energy bosons, T=0 is the only critical point, i.e., these bosons do not order into a long-range ordered state. The bosons that control the temperature dependence of $E_{gap}(T)$ and $\lambda_L(T)^{-1}$ become apparent only under the special excitation conditions necessary for the observation of the two quantities, and, evidently, have high dispersion energies. This shows that the excitation spectra of the superconductors are very complicated [10]. Relevance of excited-state bosons requires a thermal population of the dispersion relation of these bosons. Population of the dispersion relation of excited state-bosons is, however, not a continuous process, according to the Boltzmann-factor, but occurs in the discrete manner of a crossover event. At this crossover, the excited state bosons suddenly become relevant and T_{SC} appears as a second critical temperature. Below this crossover temperature, the excited state bosons seem to be completely absent and $T=T_{SC}$ is not a critical point. Due to the symmetry selection principle of relevance, only one boson type can be relevant [30]. On the other hand, thermal population of the dispersion relation of the excited state bosons that control the temperature dependence of $E_{gap}(T)$ and $\lambda_L(T)^{-1}$ is certainly never given considering that the $E_{gap}(T=0)/k_B$ values are about four times larger than T_{SC} (Figure 1).
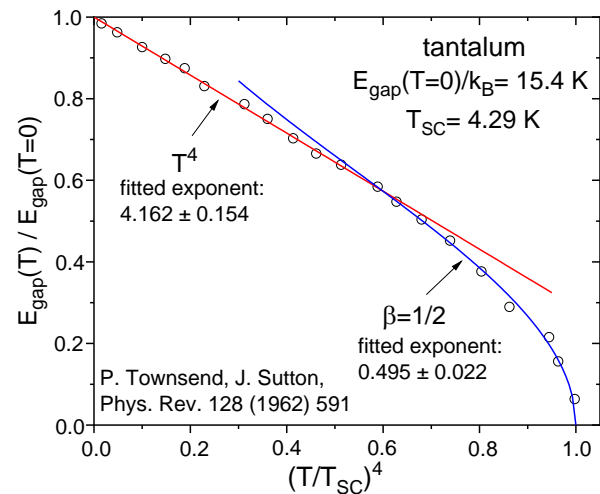

Figure 4. Normalized Cooper-pair gap energy of tantalum as a function of the reduced temperature to a power of four [32]. As for all here investigated superconducting elements, thermal decrease of the gap energy with respect to saturation at T=0 is given by a T^4 power function, followed by a crossover to the critical power function of the argument (T_{SC}-T) with mean field exponent of β=1/2 [21].

As far as $E_{gap}(T)$ data are available, the same type of universal temperature dependence as in Figure 4 [32] is observed for all superconducting elements [21]. Universality holds in the vicinity of the two critical points T=0 and $T=T_{SC}$. At the critical point T=0 the critical power function is a power function of absolute temperature and exhibits the critical exponent of ε=4. The critical power function at $T=T_{SC}$ is a power function of the argument (T_{SC}-T) and exhibits mean field exponent of β=1/2. Formally, this critical

exponent agrees with the BCS-theory [1,20]. However, in contrast to the atomistic BCS-theory, the observed, boson-defined critical power function holds over a finite distance from the critical point [31]. The finite width of the critical range provides clear evidence of boson dynamics. The critical range at T_{SC} is limited by the crossover to the critical power function at $T=0$. Crossover events are analytical changes of the temperature function and are clearly beyond the atomistic models.

As for the spontaneous magnetization of the ordered magnets [21,23], the two critical power functions at $T=T_{SC}$ and at $T=0$ intersect and give a complete description of the temperature dependence of $E_{gap}(T)$. For niobium, the same universal exponents as in the temperature dependence of $E_{gap}(T)$ occur in the temperature dependence of the reciprocal London penetration depth, λ_L^{-1} (Figure 5) [33]. This one can reasonably expect since the temperature dependence of the two quantities is controlled by the same boson type. Observation of the same critical exponents does, however, not mean that the two quantities are perfectly proportional to each other. In fact, as we have seen, for $T\rightarrow 0$ $E_{gap}(T=0)\sim T_{SC}$ (Figure 1) but $\lambda_L^{-1}(T=0)\sim T_{SC}^{1/2}$ (Figure 2). Moreover, the pre-factors of the two universal power functions at $T=0$ and at $T=T_{SC}$, i.e., the critical amplitudes, can be different for the two quantities. The similar temperature dependence of E_{gap} and λ_L^{-1} proves that the larger the gap energy is, i.e., the stronger the two Cooper-pair electrons are coupled, the lower is the diameter of the Cooper-pair orbital and the London penetration depth. Figure 5 shows, as an example, the normalized reciprocal London penetration depth of niobium as a function of the reduced temperature [33]. In other words, λ_L diverges at T_{SC} with a critical exponent of $\beta=1/2$.

For chemically and structurally more complicated superconducting compounds, the critical exponent at T_{SC} seems to remain $\beta=1/2$. This exponent is typical of an isotropic behavior as it can be expected for cubic, or weakly non-cubic materials. In structurally strongly anisotropic systems, the symmetry, i.e., the dimensionality of the excited state boson field can be lower at the critical point $T=0$. The exponent ε of the T^ε function then can assume a rational value different from $\varepsilon=4$. In this case, a symmetry crossover coincides with the common crossover between the two critical power functions at $T=0$ and at $T=T_{SC}$. The observed exponent of $\varepsilon\neq 4$ is characteristic of the specific low-temperature symmetry of the excited state boson field. As we know from magnetism, a crossover to a lower symmetry class at $T=0$ compared to T_{SC} can be caused by a sufficiently strong spontaneous lattice distortion as a function of a decreasing temperature [21]. The material then cannot be classified by only one symmetry class alone. In other words, each critical point, either $T=0$ or $T=T_c$ can have its own dynamic symmetry. Although spontaneous lattice distortions increase continuously with decreasing temperature, the boson-defined dynamics reacts in the discrete manner of a crossover event when the distortion has increased beyond the threshold to become relevant. Finite distortions that remain below this threshold are not relevant and have no effect on the boson-controlled thermodynamic observables, i.e., on the critical exponents. As an example of a low symmetry class at $T=0$, Figure 6 shows the normalized reciprocal London penetration depth of the two-dimensional organic salt κ-(BEDT-TTF)$_2$Cu(NCS)$_2$ as a function of the reduced temperature [34]. The meaning of the exponent of $\varepsilon=5/2$ is difficult to specify as long as this exponent is not reproduced by many other similar materials.
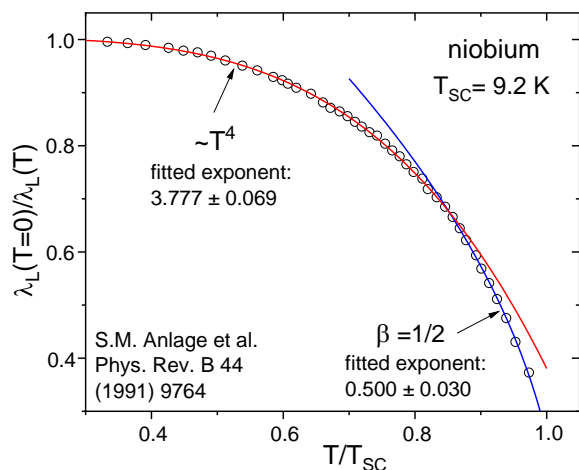

Figure 5. Normalized reciprocal London penetration depth of niobium as a function of the reduced temperature [33]. The same critical exponents as for $E_{gap}(T)$ in Figure 4 are observed at $T=0$ and at $T=T_{SC}$.
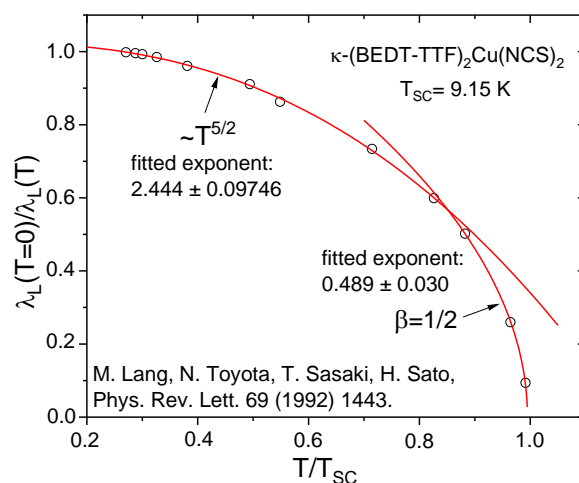

Figure 6. Normalized reciprocal London penetration depth of the strongly anisotropic organic salt κ-(BEDT-TTF)$_2$Cu(NCS)$_2$ as a function of the reduced temperature [34]. The exponent of $\varepsilon=5/2$ of the critical power function at $T=0$, T^ε, is indicative of a low-symmetry class.

For hexagonal MgB$_2$, investigated in [35], a critical exponent of $\varepsilon=2$ can be identified in the reciprocal London penetration depth (Figure 7). According to the unusual intersection of the two critical power functions in Figure 7, compared to Figure 5 and Figure 6, the symmetry of the excited state boson field must be considerably lower at $T=0$ compared to the symmetry at $T=T_{SC}$. Quite generally, when the symmetry at the critical point $T=0$ is much lower than the symmetry at $T=T_{SC}$, the crossover between the critical power function at $T=T_{SC}$ and at $T=0$, can assume a rather anomalous appearance. It is evident that more systematic investigations are necessary for an understanding of the different observed exponents ε.
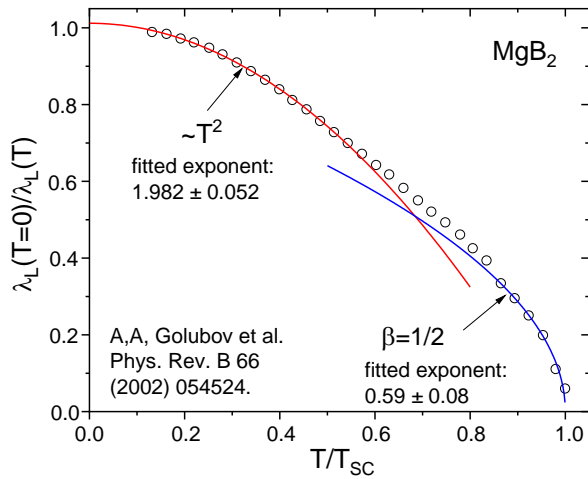
Figure 7. Normalized reciprocal London penetration depth of a MgB$_2$ *thin film sample as a function of the reduced temperature* [35].

4. Concluding Remarks

It seems to be now clear that at phase-transitions into a long-range and coherently ordered state, a boson field orders [9]. The visible atomic or magnetic order results from a coupling of atoms or spins to the ordered boson field. As we have mentioned, the superconducting transition is exceptional, in that the relevant bosons enter a short-range ordered state only. Nevertheless, comparison with the better understood long-range ordered boson field in the magnetic systems, is most revealing [9]. Characteristic of a transition into a long-range ordered boson field is the finite width of the critical range and the observed rational critical exponents [36,37,38]. The observed perfect collinear order of the spins results from a surprisingly strong coupling of the spins to the perfectly ordered boson field. The locally anisotropic near-neighbor interactions would never result into a perfect coherent, long-range order. If the anisotropic local exchange interactions would be the relevant excitations, a spin-glass like order would result. This is realized in Ising magnets only [11]. Note that in Ising magnets, Goldstone-bosons get not generated because Ising spins do not precess. The dynamics therefore is atomistic, i.e., due to the local exchange interactions. In other words, the order realized by ordered boson fields is the highest possible one and provides an entropy argument for the dominance of the bosons. The long-range ordered objects generated by the ordered Goldstone-boson field are the domains. Domains are typical of the ordered magnets [39] and of the ordered ferroelectrics [40]. The mosaic blocks, occurring in practically all single crystals, have also to be viewed as domains, generated by the bosons that order at the melting transition [38]. These bosons are, however, completely unexplored. The bosons that order at the magnetic ordering temperature, i.e., the Goldstone-bosons, are magnetic dipole radiation, generated by the precessing spins [11]. The bosons of the ferroelectric materials are evidently electric dipole radiation [40]. Although the individual domain is a stable unit, the domain configurations are not very stable and can easily be manipulated by suitable external means. As is well known, upon ferromagnetic saturation the whole sample gets transformed into the mono-domain state. The dynamic symmetry then is one-dimensional [41]. In other words, a dimensionality crossover occurs upon ferromagnetic

saturation [41]. Since the linear dimensions of the domains are much larger than the inter-atomic distance, it is evident that the domains do not result from atomistic near-neighbor interactions. The domain is, so to say, a universal, self-contained geometrical unit. The size and shape of the individual domain, therefore, must result from the ballistically propagating bosons. The finite dimension of each domain is indicative of a self-constriction mechanism of the ordered boson field. Self-constriction has to be considered as a dynamic particularity of the ordered boson fields and seems to be one origin of the spontaneous magnetostriction [21]. The domains are resonators, self-organized by the ordered boson field. In each domain, bosons and magnons are standing one-dimensional waves. As a consequence, in many magnets the magnon dispersions are as for the linear spin chain, irrespective of the locally anisotropic exchange interactions that are not relevant in the sense of the RG-theory [15,23]. Condition for a one-dimensional long-range order of the boson field is that the emission characteristics of the individual boson source is axial and that the dominant generation process of the bosons is by stimulated emission. This holds for the magnetic and for the electric dipole radiation. Due to stimulated emission, the number of bosons propagating along those crystallographic directions with a high density of the boson sources gets enhanced [42,43]. This can be viewed as a self-collimation mechanism of the bosons. Eventually, for a sufficiently sharp collimation, the critical boson density for the spontaneous onset of stimulated will be reached and the boson field orders perfectly one-dimensional [9,42,43]. Now all bosons are condensed in the same quantum state. This is realized in each domain. The ordered boson field resembles the beam of a LASER. A three-dimensional global boson field results by a coupling between the one-dimensional boson fields of the domains along x-, y- and z-axis. In other words, the dimensionality of the global boson field is given by the number of inequivalently oriented domains. The observed critical exponents are defined by the global boson field.

The superconducting transition is particular in that the relevant bosons undergo a transition into a short-range ordered state. In contrast to the long-range ordered magnets, there are no domains observed in the superconducting state. Moreover, the typical critical power functions of the argument |T$_{SC}$-T|, as they occur at the magnetic ordering transition, are absent in the zero-field heat capacity of the superconductors [10,13]. Instead, universal power functions of absolute temperature are observed above and below T$_{SC}$ [10,16]. As a consequence, the superconducting transitions are all within the critical range of the critical point T=0. As we know from RG-theory [30], the dynamics in the critical range is exclusively due to bosons. Characteristic of a critical range is short-range order. This means, at T$_{SC}$ the type of short-range order of the relevant bosons changes. Evidently, the short-range ordered units of the superconducting state are the Cooper-pairs. The radiation field emitted by the sources of the relevant bosons, therefore, cannot be axial. It is quite clear, that the bosons that order at T$_{SC}$ are the same as the bosons above T$_{SC}$ [18]. We have called the bosons of the continuous metallic solid that give rise to the universal linear-in-T heat capacity above T$_{SC}$, CMS-bosons [17]. It is suggestive to identify these bosons with electric quadrupole radiation generated by the inhomogeneous charge distributions in the soft zones between the metal atoms. Although the radiation field generated by an electric

quadrupole is theoretically unexplained, it evidently contains a component that is essentially circular or spherical in shape. Due to stimulated emission many identical quanta of the spherical waves can superimpose whereby a sharp spherical shell is generated that encapsulates the two Cooper-pair electrons. This is as for the magnetic domains that encapsulate a region with coherently ordered spins. The shape and volume of the magnetic domains (Cooper-pairs) is defined by the ordered Goldstone-boson field (ordered CMS-boson field). The short-range ordered Cooper-pairs correspond, so to say, to the domains in the long-range ordered magnets. The CMS-boson shell, surrounding the two Cooper-pair electrons, shields the charge of the two Cooper-pair electrons perfectly and allows for a free mobility of the Cooper-pairs. This is a condition for a resistivity of zero of the superconducting current. In contrast to the magnetic domains that are fixed to each other and to the crystal lattice, the spherical Cooper-pairs can move freely across the metal. They behave as a dense gas of neutral particles [16]. Consistent with the short-range order in the superconducting state is that there is no correlation between the positions of the Cooper-pairs. In contrast to the ordered magnets, for which the dynamic dimensionality is defined by the number of inequivalently oriented domains, the conventional (cubic) superconductors are isotropic system. The CMS-boson shell exerts the necessary constricting force to counteract the repulsion between the charges of the two Cooper-pair electrons. This constriction is an inherent dynamic, i.e., temperature dependent property of the ordered boson field, and is similar to the spontaneous magnetostriction in the ordered magnets [21]. Since the constriction gets stronger with decreasing temperature, the diameter of the Cooper-pairs shrinks with decreasing temperature. The corresponding binding energy between the two Cooper-pair electrons is given by the gap energy $E_{gap}(T)$ that increases with decreasing temperature. $E_{gap}(T)$ has much similarity with the magnon gap in the ordered magnets that is a measure of the stability of the spin order due to the interaction with the ordered Goldstone-boson field (magnetic dipole radiation) [44]. The decreasing diameter of the Cooper-pairs with increasing $E_{gap}(T)$ agrees with the temperature dependence of the London penetration depth for an applied magnetic field. This allows one to obtain the temperature dependence of the diameter of the Cooper-pairs from measurements of the temperature dependence of the London penetration depth. The strong superconducting diamagnetism results from the large orbital cross section of the Cooper-pairs. Since the London penetration depth agrees with the diameter of the individual Cooper-pair, it results that only one layer of Cooper-pairs next to the inner surface of the superconductor is sufficient to shield an applied magnetic field completely. The fact that, for all temperatures, a magnetic field is expelled out of the superconductor shows that the decreasing size of the Cooper-pairs gets compensated by a corresponding increase of their density such that the volume of the superconductor is always nearly completely filled with Cooper pairs [16]. This is as for the volume of the ordered magnets that is completely filled with domains. It can be assumed that the increasing number of electrons needed for the increasing number of Cooper-pairs is delivered by the conduction band. The superconductor, therefore, resembles a two-phase system with the Cooper-pairs as the condensed phase and the conduction-band electrons as the vapor phase. With the increasing number of Cooper-pairs with decreasing temperature the

superconducting systems receives an increasing mass which is certainly of influence on the dynamics, i.e., on the temperature dependence of the heat capacity of the zero-field ground state.

Concluding it has to be remarked that the just sketched scenarios need more detailed investigations, in particular field-theoretical studies, for a final approval. Many of the statements and ideas advanced in this rather phenomenological work are heuristic guides only, intended to stimulate further research activities. It cannot be excluded that with the continuing progress of our understanding of the dynamics in solids, one or the other of the here presented ideas will need a considerable correction. Nevertheless, the dominant role of bosons for the dynamics of solids is now a firmly established experimental fact. Essential for this dominance seems to be that the bosons get generated by stimulated emission. Due to stimulated emission the bosons can order, i.e., they condense all in the same or a few quantum states, whereby extremely high, local electromagnetic fields get generated. These high fields affect the microscopic near-neighbor interactions and determine the dynamics in the ordered state, instead of the non-relevant near-neighbor interactions.

Nomenclature
λ_L, London penetration depth (nm)
E_{gap}, Cooper-pair energy gap (meV)
T_{SC}, superconducting transition temperature (K)
λ, diameter of the Cooper-pair
T_{BE}, Bose-Einstein condensation temperature
μ_B, Bohr-magneton (Vsm)
μ, diamagnetic moment of the Cooper-pair (Vsm)
B_c, critical magnetic field (Gauss)
n, spatial density of the Cooper-pairs (cm^{-3})
n_e, conduction-band electron density (cm^{-3})
m_e, mass of the electron (Kgr)
β, critical exponent at T_{SC}
ε, critical exponent at T=0
e, charge of the electron (C)
μ_0, vacuum permeability (Vs/Am)

References:

[1] J. Bardeen, L.N. Cooper, J.R. Schrieffer, "Theory of Superconductivity", *Phys. Rev.* vol. 108, pp. 1175-1204, 1957.

[2] A.M. Kadin, "Spatial Structure of the Cooper Pair" *Supercond. And Novel Magnetism*, vol. 20, pp. 285-282, 2007.

[3] N. Andrenacci, M. Capezzali, H. Beck, "Internal structure of fluctuating Cooper pairs", *Eur. Phys. J. B*, vol. 53, pp. 417-432, 2006.

[4] W.V. Pogosov, "Applicability of Bardeen-Cooper-Schrieffer theory to small-sized superconductors: Role of Cooper-pair binding energy", *Solid State Commun.* vol. 207, pp. 1-4, 2015.

[5] T. Örd, K. Rägo, A. Vargunin, G. Litak, "Strong temperature effect on the size of the Cooper-pairs in a two-band superconductor" *Eur. Phys. J . B*, 91:2, pp. 1-6, 2018.

[6] N. Ahmad, S.H. Naqib, "Estimation of Cooper pair density and its relation to the critical current density in

Y(Ca)BCO high-T_c cuprate superconductors" *Results in Physics*, vol. 17, pp.103054, 1-6, 2020.

[7] F.D. Neto, M.A. Neto, O.D. Rodriguez Salmon, "Cooper-pair size and binding energy for unconventional superconducting systems", *Physica C:Supercond. and its Appl.* 549 pp. 159-163, 2018.

[8] T. Böhm et al., "Microscopic origin of Cooper pairing in the iron-based superconductor $Ba_{1-x}K_xFe_2As_2$", *Quantum Materials*, 3:48, pp. 1-6, 2018.

[9] U. Köbler, "On the precise value of the magnetic ordering temperature", *J. Magn. Magn. Mater.* 546, pp. 168839, 1-6, 2022.

[10] U. Köbler, "New Explanation of the Excitation Spectra of Conventional Superconductors *J. of Low Temp. Phys.* https://doi.org/10.1007/s10909-022-02886-7.

[11] A. Hoser, U. Köbler, "Boson Fields in Ordered Magnets", *Acta Phys. Pol.* A, vol. 127, pp. 350-352, 2015.

[12] J. Goldstone, A. Salam, S. Weinberg, "Broken Symmetries", *Phys. Rev.* vol 127, pp. 965-970, 1962.

[13] U. Köbler, "Universality in the temperature dependence of the heat capacity of magnetic solids", *Int. J. of Thermo.* vol. 23, pp.147-174, 2020.

[14] A. Hoser, U. Köbler, "Linear spin chains in paramagnetic and in ordered bulk magnets", *Physica* B, vol. 551, pp.83-88, 2018.

[15] U. Köbler, "Bosonic and magnonic magnon dispersions", *J. Magn. Magn. Mater.* vol. 502, pp. 166533, 1-18, 2020.

[16] U. Köbler, "Bose-Einstein Condensation of Cooper-Pairs in the Conventional Superconductors" *Int. J. of Thermo.* 24, pp. 238-246, 2021.

[17] U. Köbler, "On the Thermal Conductivity of Metals and of Insulators", *Int. J. of Thermo.*, vol. 20, pp. 210-218, 2017.

[18] C. Probst, J. Wittig, "Superconductivity of bcc Barium under Pressure", *Phys. Rev. Lett.* Vol. 39, pp.1161-1163, 1977.

[19] C.J. Pethick, H. Smith: "Bose-Einstein condensation in dilute gases", Cambridge Univ. Press, 2008.

[20] B. Mühlschlegel, "Die thermodynamischen Funktionen des Supraleiters", *Z. Physik*, vol. 155, pp. 313-327, 1959.

[21] U. Köbler, A. Hoser: *Experimental Studies of Boson Fields in Solids*, World Scientific, Singapore, 2018.

[22] G.K. White, "Thermal Expansion at Low Temperatures IV. Normal and Superconducting Lead", *Phil. Mag.* Vol. 7, pp. 271-278, 1962.

[23] U. Köbler, "One-Dimensional Boson Fields in the Critical Range of EuS and EuO", *Acta Phys. Pol.* A, vol. 128, pp. 398-407, 2015.

[24] O.W. Dietrich, "Critical magnetic fluctuations in MnF_2", *J. Phys. C: Solid State Phys.* vol. 2, pp. 2022-2036, 1969.

[25] B.B. Goodman, E. Mendoza, "The Critical Magnetic Field of Aluminium, Gallium and Zinc", *Philosophical Magazine* vol. 42, pp. 594-602, 1951.

[26] R. Kleiner, W. Buckel: *Superconductivity: an introduction*, Wiley-VCH, Weinheim, 2016.

[27] W. Meissner, R. Ochsenfeld, "Ein neuer Effekt bei Eintritt der Supraleitfähigkeit" *Naturwissenschaften*, vol. 21, pp. 787-788, 1933.

[28] F. London, H. London, "Supraleitung und Diamagnetismus", *Physica*, vol. 2, pp. 341-354, 1935.

[29] M. v. Laue, F. u. H. London, "Zur Theorie der Supraleitung", *Z. Physik*, vol. 96, pp. 359-364, 1935.

[30] K.G. Wilson, J. Kogut, "The renormalization group and the ε expansion", *Phys. Rep.* vol. 12C, pp. 75-199, 1974.

[31] U. Köbler, "Crossover phenomena in the critical range near magnetic ordering transition", *J. Magn. Magn. Mater.* Vol. 453, pp. 17-29, 2018.

[32] P. Townsend, J. Sutton, "Investigation by Electron Tunneling of the Superconducting Energy Gaps in Nb, Ta, Sn, and Pb", *Phys. Rev.* vol. 128, pp. 591-595, 1962.

[33] S.M. Anlage, B.W. Langley, G. Deutscher, J. Halbritter, M.R. Beasley, "Measurements of the temperature dependence of the magnetic penetration depth in $Yba_2Cu_3O_{7-\delta}$ superconducting thin films", *Phys. Rev.* B, vol. 44, pp. 9764-9767, 1991.

[34] M. Lang, N. Toyota, T. Sasaki, H. Sato, "Magnetic Penetration Depth of κ-$(BEDT-TTF)_2Cu(NCS)_2$: Strong Evidence for Conventional Cooper Pairing" *Phys. Rev. Lett.* vol. 69, pp. 1443-1446, 1992.

[35] A.A. Golubov, A. Brinkman, O.V. Dolgov, J. Kortus, O. Jepsen, "Multiband model for penetration depth in MgB_2", *Phys. Rev.* B vol. 66, pp. 054524, 1-5, 2002.

[36] R.K. Pathria: *Statistical Mechanics*, 2nd ed., Butterworth-Heinemann, Oxford, 1996.

[37] P. Heller, "Experimental investigations of critical phenomena", *Rep. Prog. Phys.* vol. 30, pp. 731-826, 1967.

[38] U. Köbler, V. Bodryakov, "On the melting process of solids", *Int. J. of Thermo.* vol. 18, pp. 200-204, 2015.

[39] A. Hubert, R. Schäfer: *Magnetic Domains,* Springer, Berlin, 2000.

[40] E. Fatuzzo, W.J. Merz: *Ferroelectricity*, North-Holland, Amsterdam, 1967.

[41] U. Köbler, A. Hoser, C. Thomas: "Dimensionality crossover upon magnetic saturation of Fe, Ni and Co", *J. Magn. Magn. Mater.* vol. 321, pp. 1202-1208, 2009.

[42] U. Köbler, "Sound waves and phonons in crystalline solids", *J. Chem. Thermo.*, to be published.

[43] U. Köbler, "Magnetic ordering by boson fields", *Eur. Phys. J. B.*, to be published.

[44] U. Köbler, "Thermal decay of magnons in MnF_2", *J. Magn. Magn. Mater.* vol. 551, pp. 169129, 1-9, 2022.

Research Article

Time-Fractional Cattaneo-Type Thermoelastic Interior-Boundary Value Problem Within A Rigid Ball

[1]G. Dhameja , [2]L. Khalsa , [3]*V. Varghese

[1,2,3] Department of Mathematics, M.G. College, Armori, Gadchiroli, India
E-mail: [1]dhameja.geeta0311@gmail.com, [2]lalsinghkhalsa@yahoo.com, [3]*vino7997@gmail.com

Abstract

The paper discusses the solution of an interior-boundary value problem of one-dimensional time-fractional Cattaneo-type heat conduction and its stress fields for a rigid ball. The interior value problem describes the dependence of the boundary conditions within the ball's inner plane at any instant with a prescribed temperature state, in contrast to the exterior value problem, which relates the known surface temperature to boundary conditions. A single-phase-lag equation with Caputo fractional derivatives is proposed to model the heat equation in a medium subjected to time-dependent physical boundary conditions. The application of the finite spherical Hankel and Laplace transform technique to heat conduction is discussed. The influence of the fractional-order parameter and the relaxation time is examined on the temperature fields and their related stresses. The findings show that the slower the thermal wave, the bigger the fractional-order setting, and the higher the period of relaxation, the slower the heat flux propagates.

Keywords: Fractional Cattaneo-type equation; fractional calculus; non-Fourier heat conduction; ball; thermal stress; integral transform.

1. Introduction

Many papers deal with the temperature and thermal stress fields due to body heating in the theory of thermal stress. The determination of either heat flux or temperature at interior points is deduced from the known temperature at the surface. In contrast, there is a subset of cases in which the temperature distribution at some interior points is known. It is required to determine either temperature or heat flux on the surface, commonly named interior value problems (or so-called inverse temperature field problems). In order to find the unknown functions that characterize the boundary conditions, one assumes that (i) a kind of the boundary conditions are known, (ii) initial conditions are known, (iii) other boundary conditions - if any exist - are known, (iv) specific mechanical or thermal internal responses inside the object are known. When it comes to determining the transient temperature or heat flux distribution at a surface where temperature or heat flux measurements are impossible or problematic, then inverse temperature field problems will have a practical and useful application. Such situations have been documented several times in literature; therefore, few of them are quoted here.

Stolz [1] suggested the first solutions for the inverse heat problems with integral equations and numerical methods. Necsulescu [2], Woodbury [3], Özışık [4] and Beck [5] have developed several methods of interior-boundary value heat conduction problems for various forms of boundary conditions. Torsten et al. [6] solved the linear inverse heat conduction problem to reconstruct unknown heat flux at the boundary for two- and three-dimensional problems. Lu and Tervola [7] developed an empirical approach to heat conduction in a composite slab when subjected to periodic temperature changes. Khobragade et al. [8] investigated an inverse transient thermoelastic problem in which we need to determine the unknown temperature, displacement and stress function on the outer curved surface of a thin annular disc when the interior heat flux is known using integral transform techniques. Woodfield et al. [8] solved the inverse heat conduction problems analytically using the Laplace transform when it has a given far-field boundary state. Pourgholi and Rostamian [9] used the Tikhonov regularization approach to provide a numerical solution to the one-dimensional inverse heat conduction problems. Danaila and Chira [10] proposed a solution to the inverse one-dimensional heat conduction problem; they intend to estimate the unsteady boundary state on the right side using two techniques: first, to combine the gradient approach with an adjunct issue for the estimate of gradient function, and second, to regularize Tikhonov for hyperbolization of the equation of heat conduction. Ivanchov and Kinash [11] found the inverse problem in a rectangle, the heat conduction equation with an unknown coefficient, as a function of time and space variables using the Green function. Chen et al. [12] used the one-dimensional problem of inverse heat conduction to measure the surface temperature; they used a nonlinear form of calculation with an integral equation. Chang et al. [13] split them into two main solving groups in their study paper on the computing approaches used for inverse heat conduction problems: mesh techniques and meshless algorithms.

Recently, the fractional-order concept has been put in use to obtain better performance of the system. The Laplace

transform was used by Kukla and Siedlecka [14] to solve fractional heat conduction in a two-layer slab. Meanwhile, technological development and innovation in research helped bring about a revolution by applying heat relaxation time to the non-equilibrium heat conduction system [15-18]. Cattaneo [19] and Vernotte [20] have summed the heat relaxation time to a partial heat flux time derivative. In the meantime, Compte and Metzler [21] focused on four different generalizations of the Cattaneo telegraph equations, each of which was accompanied by a different scheme: continuous-time random walks, nonlocal transport theory, and delayed flux-force relation. According to Povstenko [22], the time-fractional Cattaneo heat conduction equation derived from the Fourier law's time-non-local generalization using multiple kernels is a function Mittag-Leffler form's related thermal stress theory. Mishra and Rai [23] obtained the fractional single-phase heat conductivity function by applying the Taylor series's fractional formula to the single-phase heat conductivity function. The mathematical solutions of the fractional Cattaneo-Vernotte heat conduction problem with Neumann boundary conditions have recently been obtained in a semi-infinite medium by a few researchers [24-29]. Nevertheless, the interior-boundary value problem of time-fractional Cattaneo-type heat conduction with the physical Robin-type boundary state was less studied, based on the fractional model Cattaneo-Vernotte. Hence, this paper investigates the analytical solution for Cattaneo's time-fractional heat conduction in a finite one-dimensional ball under Robin-type conditions and analyzes the heat conduction mechanism, which differs from the fractional-order parameters.

The outline of the paper consists of five parts. In part 2, the basic set of equations for the mathematical modelling of the single-phase-lag heat conduction equation of the fractional Cattaneo-type model is stated. Then, a way of obtaining the exact solutions of time-fractional Cattaneo heat conduction analysis for such a problem is briefly presented. The final parts contain an analysis of the outcomes and a discussion concerning the particular case. Conclusive findings are summed up in the last detail.

2. Mathematical Model
2.1 Formulation Of Fractional Cattaneo Equation

The classical Fourier's law of heat conduction [30]

$$q(t) = -k \nabla T(t) \tag{1}$$

in which $q(t)$ is the heat flux vector represents heat flow per unit time per unit area of the isothermal surface, t is the time, and k is the thermal conductivity of the material, ∇ is the spatial gradient operator, and T is the temperature gradient, and it is a vector normal to the surface, respectively. Since the heat flux points to decreasing temperature, the minus sign is involved in making the heat flow a positive quantity. When the heat flux is in W/m³, and the temperature gradient is in °C/m, the thermal conductivity has W/(m°C).

Introduction of single-phase-lag to evade discrepancy between the mathematical model [19,20] and the experimental observations [31], and this extension turns the parabolic into a hyperbolic equation

$$q(t) + \zeta \frac{\partial q(t)}{\partial t} = -k \nabla T(t) \tag{2}$$

Here the flux relaxes with some given characteristic time constant ζ is the phase lag of the heat flux or so-called relaxation time. Consequently, the propagation velocity is finite. As a limiting case $\zeta \to 0$, one recovers Fourier's law with an infinitely fast propagation. The Laplace transform allows us to rewrite Eq. (2) as a time-non-local constitutive equation with the exponential kernel [22] as

$$q(t) = -\frac{k}{\zeta} \int_0^t \exp\left(-\frac{t-\tau}{\zeta}\right) \nabla T(\tau) \, d\tau \tag{3}$$

Combining Eq. (1) with the conservation law of energy [32], leads to

$$-\nabla \cdot q(t) + Q = \rho C_v \frac{\partial T(t)}{\partial t} \tag{4}$$

leads to the single-phase-lag heat conduction equation as

$$\frac{\partial^2 T(t)}{\partial t^2} + \frac{1}{\zeta} \frac{\partial T(t)}{\partial t} = \frac{\kappa}{\zeta}\left(\Delta T(t) + \frac{Q}{k}\right) \tag{5}$$

where thermal diffusivity is $\kappa = k / \rho C_v$, k being the conductivity of the material, ρ is the density of the material, C_v is the specific heat capacity, Q represents the uniform heat generation inside the material, and the square root of the ratio κ / ζ defines the finite speed within the medium, respectively.

Recently, a kind of generalization of Eq. (2) and (4) consisting of replacing the classical integer-order derivative with fractional order can be referred to in literature [21,22] and the reference therein. Next, we consider the generalization of Eq. (2) in the form

$$\frac{\partial q(t)}{\partial t} + \zeta \frac{\partial^{\alpha-1} q(t)}{\partial t^{\alpha-1}} = -k \nabla T(t), \, 0 < \alpha \le 1 \tag{6}$$

in which the fractional Caputo derivative of order α with a lower limit zero

$$\frac{\partial^\alpha f(t)}{\partial t^\alpha} = {}_0^C D_t^\alpha f(t) = \begin{cases} \frac{1}{\Gamma(m-\alpha)} \int_0^t (t-\gamma)^{m-\alpha-1} \frac{\partial^m f(\gamma)}{\partial \gamma^m} d\gamma, \\ m-1 < \alpha < m, \\ \frac{\partial^m f(t)}{\partial t^m}, \alpha = m, \, m \in N \end{cases} \tag{7}$$

whereas the Riemann-Liouville fractional derivative is taken as

$$D_{RL}^\alpha f(t) = \frac{\partial^m}{\partial t^m}\left\lfloor \frac{1}{\Gamma(m-\alpha)} \int_0^t (t-\gamma)^{m-\alpha-1} f(\gamma) d\gamma \right\rfloor, \tag{8}$$
$$m-1 < \alpha < m$$

The law of heat conduction proposed by Gurtin and Pipkin [33], which leads to general time-nonlocal dependence, was later modified by Povstenko [22] as

$$q(t) = -k \int_0^t K(t-\tau) \nabla T(\tau) \, d\tau \tag{9}$$

where a general heat flux history model depends on the relaxation kernel $K(t)$.

By simple calculations, Compte and Metzler [4] have shown that the generalized Cattaneo law, obtained from the following relationship

$$\frac{\partial q(t)}{\partial t} + \zeta \frac{\partial^{\alpha-1} q(t)}{\partial t^{\alpha-1}} = -k \left(\frac{\partial}{\partial t} + \zeta \frac{\partial^{\alpha-1}}{\partial t^{\alpha-1}} \right) \int_0^t K(t-\tau) \nabla T(\tau) d\tau \quad (10)$$

By using Leibniz's formula for the differentiation of an integral, one obtains

$$\frac{\partial q(t)}{\partial t} + \zeta \frac{\partial^{\alpha-1} q(t)}{\partial t^{\alpha-1}} = -K(0)\nabla T(t)$$
$$- \int_0^t \left[\frac{\partial}{\partial t} K(t-\tau) + \zeta \frac{\partial^{\alpha-1}}{\partial t^{\alpha-1}} K(t-\tau) \right] \nabla T(\tau) d\tau \quad (11)$$

Now compared with Eq. (6), it appears clear that we must have $K(0) = k$ and

$$\frac{\partial}{\partial t} K(t) + \zeta \frac{\partial^{\alpha-1}}{\partial t^{\alpha-1}} K(t) = 0 \quad (12)$$

By solving Eq. (12), one can obtain the relaxation function in the Laplace domain as

$$K^*(s) = \frac{k}{\zeta} \left(\frac{s^{-1}}{s^{\alpha-2} + 1/\zeta} \right) \quad (13)$$

The expression in (14) can be inverted in terms of a generalized Mittag-Leffler function (see [34]) to yield

$$K(t) = \frac{k}{\zeta} t^{\alpha-4} E_{\alpha-2,\alpha-1} \left(-\frac{1}{\zeta} t^{\alpha-2} \right) \quad (14)$$

Multiplying with vector ∇ to Eq. (6), and then using Eq. (4), results in the generalized Cattaneo equation [22]

$$\frac{\partial^2 T(r,t)}{\partial t^2} + \frac{1}{\tau} \frac{\partial^\alpha T(r,t)}{\partial t^\alpha} = \frac{\kappa}{\tau} \left(\Delta T(r,t) + \frac{Q}{k} \right) \quad (15)$$

It was also observed that only a few authors had paid attention to the fourth equation. Here, the authors believe that this gap could lead to generalization, taking into account the generation of internal heat sources within the body.

2.2 Solution Time-Fractional Cattaneo Heat Conduction
Figure 1 shows a schematic sketch for a ball in the spherical coordinate axes r, θ, z is used to describe a time-fractional thermoelastic analysis. The temperature profile is assumed to be a radial coordinate's transient function independent of the tangential and azimuthal coordinates.
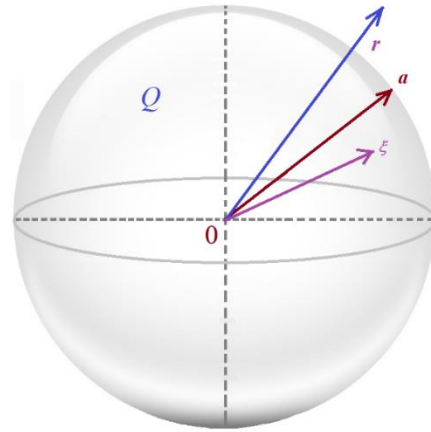

Figure 1. Profile of a spherical metal ball.

We assume that the temperature at every instant is given by

$$T(r,t) = \int_0^t f(t-\gamma)\theta(r,\gamma) d\gamma \quad (16)$$

where $\theta(r,t)$ is the basic solution to the following problem:

$$\frac{\partial^2 \theta}{\partial t^2} + \frac{1}{\tau} \frac{\partial^\alpha \theta}{\partial t^\alpha} = \frac{\kappa}{\tau} \left[\frac{1}{r^2} \frac{\partial}{\partial r} \left(r^2 \frac{\partial \theta}{\partial r} \right) \right] + \frac{\kappa}{\tau} \frac{Q}{k},$$
$$0 \le r \le a,\ 0 < t < \infty,\ 0 < \alpha \le 1 \quad (17)$$

subjected to zero initial and ambient conditions

$$\theta(r,t=0) = 0,\ \frac{\partial}{\partial t}\theta(r,t=0) = 0,\ 0 \le r \le a, 0 < \alpha \le 1 \quad (18)$$

under the physical Robin boundary condition [36-38], which is a linear combination of temperature and its normal derivative along the radial direction

$$\theta(r=\xi,t) + \zeta D_{RL}^{1-\alpha} \frac{\partial \theta}{\partial r}(r=\xi,t) = q_s(t), 0 < \xi < a,\ 0 < \alpha \le 1 \quad (19)$$

and the assumed bounded condition at the origin as

$$\lim_{r \to 0} \theta(r,t) \ne \theta_\infty \quad (20)$$

with the fact that the temperature at the ball surface, say $\theta(r=a,t) = \Theta(t)$, is unknown. Here the notation θ_∞ represents the far-field temperature, $D_{RL}^{1-\alpha}$ is the Riemann Liouville fractional derivative of the fractional-order $1-\alpha$, $q_s(t) = q(r=0,t) = (\partial_t + \zeta D_{RL}^{1-\alpha}) f(t)$, $f(t) = q_0 \delta(t)$ is the sectional prescribed heat supply, $\delta(\ )$ is the Dirac delta function and q_0 is a constant associated with delta term, respectively.

We present the function $\theta(r,t)$ in the first phase of solving this problem in the superposition of steady-state and transient solution

$$\theta(r,t) = \theta_s(r) + \theta_t(r,t) \quad (21)$$

The function $\theta_s(r)$ satisfies the steady-state differential equation

$$\frac{1}{r^2}\frac{\partial}{\partial r}\left(r^2\frac{\partial\theta_s}{\partial r}\right)+\frac{\kappa}{\tau}\frac{Q}{k}=0 \tag{22}$$

subjected to non-homogeneous boundary conditions as given in Eq. (19). Solving Eq. (22) leads

$$\theta_s(r)=-\frac{\kappa}{\tau}\frac{Q}{k}\int_0^r\left(\frac{1}{r^2}\int_0^r r^2 dr\right)dr+C_2 \tag{23}$$

in which the constant C_2 is obtained within the Laplace domain as

$$C_2=\Psi(t)\left(q_0+\frac{\kappa}{\tau}\frac{Q}{6k}\xi^2\right)+\zeta\frac{\kappa}{\tau}\frac{Q}{3k}\xi \tag{24}$$

where

$$\Psi(t)=\begin{cases}\dfrac{t^{-\alpha}}{\Gamma(1-\alpha)},\ 0<\alpha<1,\\[2mm]\delta(t),\ \alpha=1\end{cases}$$

Similarly, the function $\theta_t(r,t)$ satisfies the non-homogeneous differential equation

$$\frac{\partial^2\theta_t}{\partial t^2}+\frac{1}{\tau}\frac{\partial^\alpha\theta_t}{\partial t^\alpha}=\frac{\kappa}{\tau}\left[\frac{1}{r^2}\frac{\partial}{\partial r}\left(r^2\frac{\partial\theta_t}{\partial r}\right)\right] \tag{25}$$

subjected to homogenous boundary conditions given as

$$\theta_t(r,t=0)=0,\ \frac{\partial\theta_t}{\partial t}(r,t=0)=0 \tag{26}$$

$$\theta_t(r=\xi,t)+\zeta D_{RL}^{1-\alpha}\frac{\partial\theta_t}{\partial r}(r=\xi,t)=0 \tag{27}$$

Applying the Laplace transform with respect to variable t leads to

$$\left(s^2+\frac{1}{\tau}s^\alpha\right)\bar{\theta}_t=\frac{\kappa}{\tau}\left[\frac{1}{r^2}\frac{\partial}{\partial r}\left(r^2\frac{\partial\bar{\theta}_t}{\partial r}\right)\right] \tag{28}$$

$$\bar{\theta}_t(r=\xi,t)+\zeta s^{1-\alpha}\frac{\partial\bar{\theta}_t}{\partial r}(r=\xi,t)=0 \tag{29}$$

Multiplying $J_0(r\,k_i)\,r^2$ to Eq. (28) and integrating with regards to r from O to a. Now on account of the operational property (refer to Appendix A) and inserting the boundary condition (29), one obtains

$$\bar{\bar{\theta}}_t(k_i,s)=\frac{1}{s^2+(1/\tau)s^\alpha+k_i^2} \tag{30}$$

Taking the Laplace inversion integral [39] of Eq. (30), one obtains

$$\bar{\theta}_t(k_i,t)=\frac{1}{2\pi i}\int_{c-i\infty}^{c+i\infty}\frac{\exp(st)}{s^2+(1/\tau)s^\alpha+k_i^2}ds \tag{31}$$

where c is greater than the real part of the integrand's singularities.

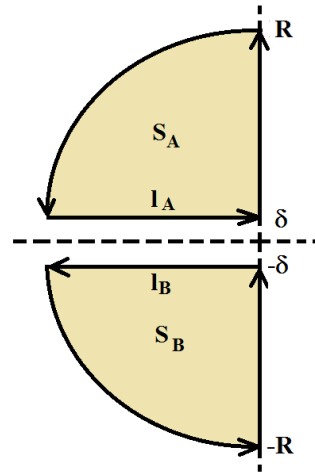The integration path for $t\geq0$ inside the principal branch of $s^\alpha(-\pi<\arg s<\pi)$ is depicted in Figure 2.

Figure 2 Integration path

Let $\delta\to0$ and $R\to\infty$. Since $\cos(.)\leq0$ if $\pi/2\leq|.|<\pi$ and $\exp(st)/g(s)=o(1/R^2)$ if $R\to\infty$ the integral vanishes on the circular arcs with $o(1/R)$. Then $g(s)=s^2+(1/\tau)s^\alpha+k_i^2$ has exactly two zeros $s_{A/B}=-\mu\pm i\vartheta$ on the principal branch, which are simple, conjugate complex and placed in the open left half-plane. To solve Eq. (30), using the residue theorem lead to

$$\bar{\theta}_t(t)=\operatorname{Re}S_A\left(\frac{\exp(st)}{g(s)}\right)+\operatorname{Re}S_B\left(\frac{\exp(st)}{g(s)}\right)\\-\frac{1}{2\pi i}\lim_{\substack{R\to\infty\\\delta\to0}}\left[\int_{l_1}\frac{\exp(st)}{g(s)}dt+\int_{l_2}\frac{\exp(st)}{g(s)}dt\right] \tag{32}$$

Firstly consider $\bar{\theta}_1(t)$ as the sum of the first two terms of Eq. (32) and taking $\hat{a}=\operatorname{Re}[g'(s_A)]$ and $\hat{b}=\operatorname{Im}[g'(s_A)]$, one gets

$$\bar{\theta}_1(t)=\frac{2\exp(-\mu t)}{\hat{a}^2+\hat{b}^2}[\hat{a}\cos(\vartheta t)+\hat{b}\sin(\vartheta t)] \tag{33}$$

Now consider $\bar{\theta}_2(t)$ as the last terms of Eq. (32), along $l_{A/B}:s=p\exp(\pm i\pi)\pm i\delta,\ p\in[0,\infty]$. If $\delta\to0$ then $s^2\to p^2$, $s^\alpha\to p^\alpha\exp(\pm i\pi\alpha)$ $=p^\alpha[\cos(\pi\alpha)\pm i\sin(\pi\alpha)],\ ds\to dp$ and, one obtains

$$\bar{\theta}_2(t)=-\frac{1}{\pi}\operatorname{Im}\left[\int_0^\infty\frac{\exp(-pt)\,dp}{p^2+(1/\tau)\,p^\alpha[\cos(\pi\alpha)\pm i\sin(\pi\alpha)]+k_i^2}\right] \tag{34}$$

Removing the imaginary number in the denominator by its conjugate, one gets

$$\bar{\theta}_2(t)=\frac{\sin(\pi\alpha)}{\pi\tau}\left[\int_0^\infty\frac{p^\alpha\exp(-pt)\,dp}{[p^2+(1/\tau)\,p^\alpha(\cos(\pi\alpha)+k_i^2]^2+[(1/\tau)\,p^\alpha\sin(\pi\alpha)]^2}\right] \tag{35}$$

Taking the sum of residues as $\bar{\theta}_s(t) = \bar{\theta}_1(t) + \bar{\theta}_2(t)$, one obtains

$$\bar{\theta}_t(k_i,t) = \frac{2\exp(-\mu t)}{\hat{a}^2 + \hat{b}^2}[\hat{a}\cos(\vartheta t) + \hat{b}\sin(\vartheta t)] + \frac{\sin(\pi\alpha)}{\pi\tau}$$

$$\left[\int_0^\infty \frac{p^\alpha \exp(-pt)\,dp}{[p^2 + (1/\tau)\,p^\alpha(\cos(\pi\alpha) + k_i^2]^2 + [(1/\tau)\,p^\alpha \sin(\pi\alpha)]^2}\right] \tag{37}$$

Applying the inversion theorem (refer to Appendix A), one obtains

$$\theta_t(r,t) = \left(\frac{4}{\pi\xi^2}\right)\sum_{i=1}^\infty \frac{k_i^2}{h^2 + k_i^2} \frac{J_0(rk_i)}{[J'_{1/2}(\alpha_i)]^2}\bar{\theta}(k_i,t) \tag{38}$$

Taking the temperature as $\theta(r,t) = \theta_s(r) + \theta_t(r,t)$, one obtains

$$\theta(r,t) = -\frac{\kappa}{\tau}\frac{Q}{k}\int_0^r\left(\frac{1}{r^2}\int_0^r r^2 dr\right)dr + \left(\frac{4}{\pi\xi^2}\right)\sum_{i=1}^\infty \frac{k_i^2}{h^2 + k_i^2}\frac{J_0(rk_i)}{[J'_{1/2}(\alpha_i)]^2}$$
$$\times \bar{\theta}(k_i,t) + \Psi(t)\left(q_0 + \frac{\kappa}{\tau}\frac{Q}{6k}\xi^2\right) + \zeta\frac{\kappa}{\tau}\frac{Q}{3k}\xi \tag{39}$$

and unknown temperature function on the outer curved surface is given by

$$\theta(a,t) = -\frac{\kappa}{\tau}\frac{Q}{k}\left[\int_0^a\left(\frac{1}{r^2}\int_0^r r^2 dr\right)dr\right]$$
$$+ \left(\frac{4}{\pi\xi^2}\right)\sum_{i=1}^\infty \frac{k_i^2}{h^2 + k_i^2}\frac{J_0(ak_i)}{[J'_{1/2}(\alpha_i)]^2}\bar{\theta}(k_i,t) \tag{40}$$
$$+ \psi(t)\left(q_0 + \frac{\kappa}{\tau}\frac{Q}{6k}\xi^2\right) + \zeta\frac{\kappa}{\tau}\frac{Q}{3k}\xi$$

Substituting Eq. (40) into $\theta(r=a,t) = \Theta(t)$, one can get the unknown temperature $T(r=a,t) = \int_0^t f(t-\gamma)\Theta(\gamma)\,d\gamma$ at the ball surface.

2.3 Displacement And Stress Field Solution

Let $u_r = u_r(r,t)$ be a component of displacement and expressed [40] as

$$u_r(r,t) = \alpha_t\left(\frac{1+\upsilon}{1-\upsilon}\right)\frac{1}{r^2}\int_0^r T(r,t)r^2 dr$$
$$+ 2\alpha_t\left(\frac{1-2\upsilon}{1-\upsilon}\right)\frac{r}{a^3}\int_0^a T(r,t)r^2 dr \tag{41}$$

that satisfies the displacement equation

$$\frac{d}{dr}\left[\frac{1}{r^2}\frac{d}{dr}(r^2 u_r)\right] = K\frac{dT}{dr} \tag{42}$$

in which $K = [(1+\upsilon)/(1-\upsilon)]\alpha_t$ is the restraint coefficient, α_t and υ denote the coefficient of linear thermal expansion and Poisson's ratio, respectively.

Let $\sigma_{rr}, \sigma_{\theta\theta}, \sigma_{\varphi\varphi}$ be the components of stress and expressed [40] as

$$\sigma_{rr}(r,t) = \frac{\alpha_t E}{1-\upsilon}\left[\frac{2}{a^3}\int_0^a T(r,t)r^2 dr - \frac{1}{r^3}\int_0^r T(r,t)r^2 dr\right]$$

$$\sigma_{\theta\theta}(r,t) = \sigma_{\varphi\varphi}(r,t) = \tag{43}$$

$$\frac{\alpha_t E}{1-\upsilon}\left[\frac{2}{a^3}\int_0^a T(r,t)r^2 dr - \frac{1}{r^3}\int_0^r T(r,t)r^2 dr - T(r,t)\right]$$

in which traction-free boundary conditions are $\sigma_{rr}(r=a,t) = 0$.

Substituting $T(r=a,t)$ into Eqs. (41) and (43), one can obtain the ball surface's unknown displacement and thermal stresses.

3. Numerical Results, Discussion And Remarks

For the sake of simplicity of numerical computations, we introduce the following nondimensional parameters as

$$\bar{r} = r/a, \bar{t} = t\kappa/a^2, \bar{T} = T/T_0, \bar{u}_i = u_i / KT_0 a \, (i=r),$$
$$\bar{\sigma}_{ii} = \sigma_{ii} / E\alpha_t T_0 \, (i=r,\theta,\varphi) \tag{44}$$

with physical parameters for the solid ball as $a = 2m$ and the surrounding temperature as $T_0 = 150°C$. Substituting the value of Eq. (44) in Eqs. (39), (41) and (43), one obtains the expressions for the temperature, displacement and thermal stresses for our numerical discussion.

Table 1. Thermo-mechanical properties: Aluminum.

Dimension	Value
Modulus of Elasticity, E	70 GPa
Poisson's ratio	0.35
Thermal Expansion Coefficient, α_t	$23 \times 10^{-6}/{}^0C$
Thermal diffusivity, κ	84.18×10^{-6} m^{2}s^{-1}
Thermal conductivity, λ	204.2Wm^{-1}K^{-1}

The numerical computations have been carried out for the Aluminum (pure) material with the thermo-mechanical properties as given in Table 1. The $k_i = \alpha_i/a = 2.61736$, 5.51894, 8.65373, 11.7915, 14.9309, 18.0711, 21.2116, 24.3525, 27.4935, 30.6346, 33.7758, 36.9171, 40.0584, 43.1998, 46.3412, 49.4826are the positive and real roots of the transcendental equation $k_i J'_n(ak_i) + hJ_n(ak_i) = (\alpha_i/a)J'_n(\alpha_i) + hJ_n(\alpha_i) = 0$.

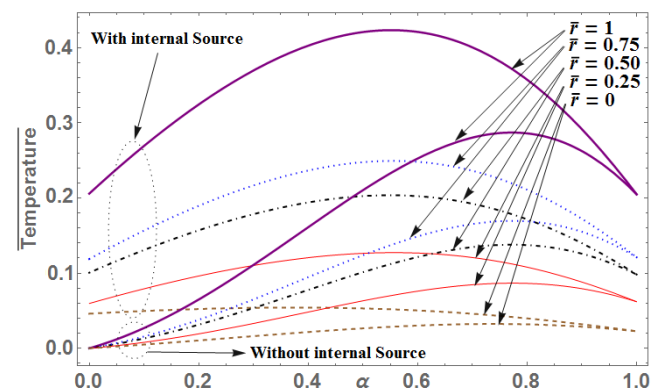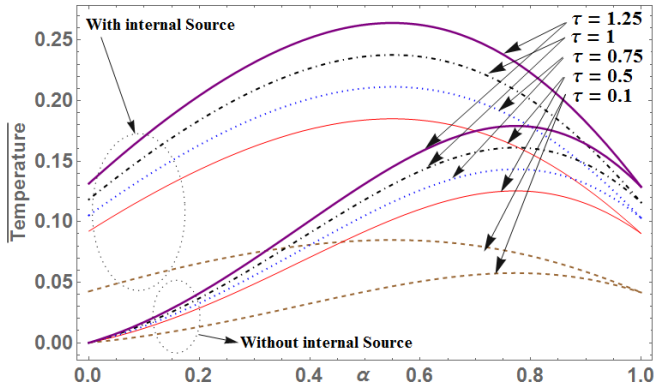*Figure 3. Temperature distribution along α for different values of $\bar{r}$ ($\tau = 1$, $t = 0.6$).*

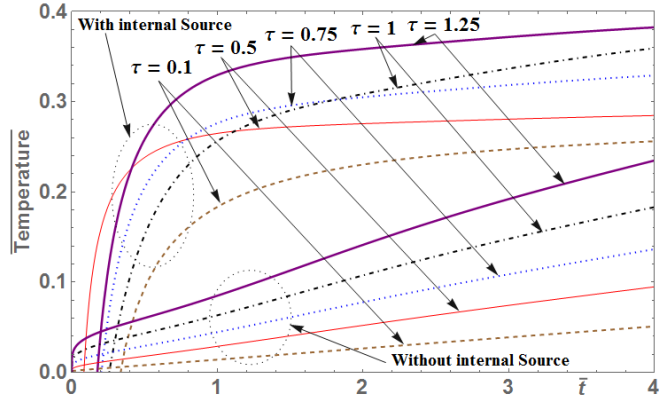*Figure 4. Temperature profile along α for different values of τ ($\bar{r} = 0.8$, $t = 0.6$).*
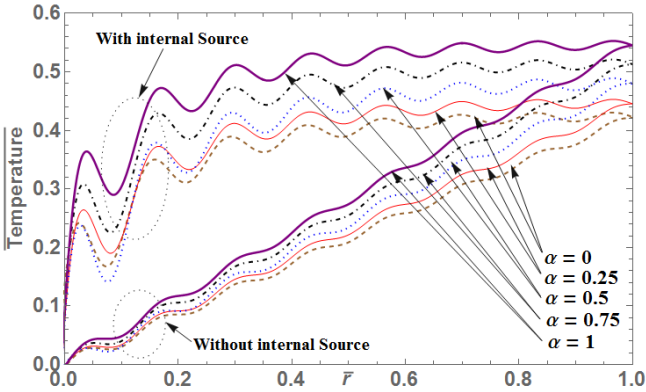

Figure 5. Temperature along $\bar{r}$ for different values of α ($\tau = 0.75$, $t = 1$).
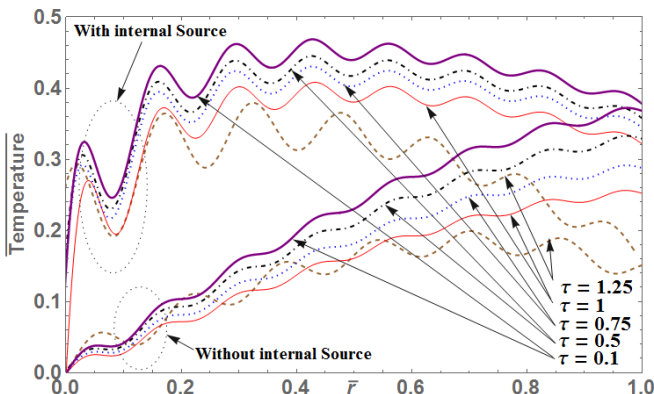

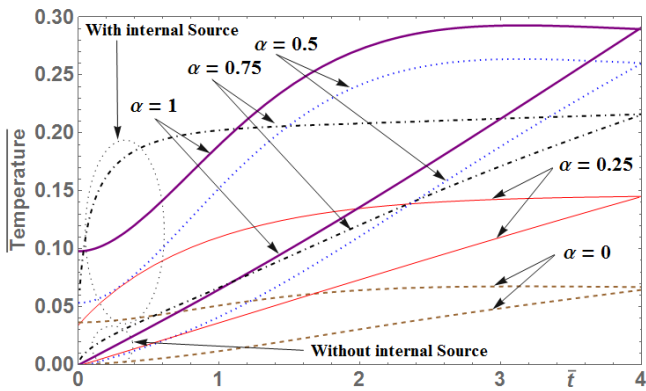*Figure 6. Temperature variation along $\bar{r}$ for various values of τ ($\alpha = 0.8$, $t = 1$).*

Figure 7. Temperature distribution along $\bar{t}$ for different values of α ($\tau = 1$, $t = 0.6$).

Figure 8. Temperature profile along $\bar{t}$ for different values of τ ($\alpha = 0.8$, $\bar{r} = 1$).

Figures 3-14 illustrate the numerical results in the graphical form for temperature distribution, displacement profile and variation in stress distribution in a spherical ball under the physical Robin boundary condition. Figures 3-4 denote the temperature distribution against the fractional order α for the various values of $\bar{r}$ and τ, both with and without an internal heat source. It can be noticed in both the figures that under the absence of a heat source, the temperature is zero at the initial stages, starts gradually increasing, attains maxima at a different value of $\bar{r}$ and τ, and it finally decreases asymptotically. On the other hand, the temperature has a specific value at the initial stages under a heat source and behaves the same as it did without a heat source. The gradual increase in the temperature for both, with or without a heat source, for a particular value α may be due to the body's geometry's ability to hold the heat.

Figures 5-6 represent the temperature value along dimensionless radial direction for different values of α and τ, for both with and without a heat source. The hike in the sinusoid pattern may be due to the internal heat generation accumulation, but it gets flattened at the ball's outer core. Figures 7-8 depict the variation in the temperature distribution over time $\bar{t}$ for different values of α and τ, with and without an internal heat source. From the figure, it is clearly understood that the temperature value increases linearly with the increase in time in the absence of an internal heat source and surrounding temperature, which defines the close correlation between time and temperature. In contrast, the presence of heat generation as well as surrounding heat generates a gradual increase curve for the value of temperature and attains uniformity after some time. Figure 9 gives a variation of dimensionless displacement $\bar{u}_r$ along the radial direction for different values α with and without a heat source. The effect of the temperature distribution in the presence of internal heat generation causes a dramatic change in displacement compared to the change observed in the absence of a heat source. It can be easily seen that no displacement is observed initially, but along the radial direction, it increases and then becomes stagnant at a particular value of $\bar{r}$ due to the effect of temperature distribution on the ball.
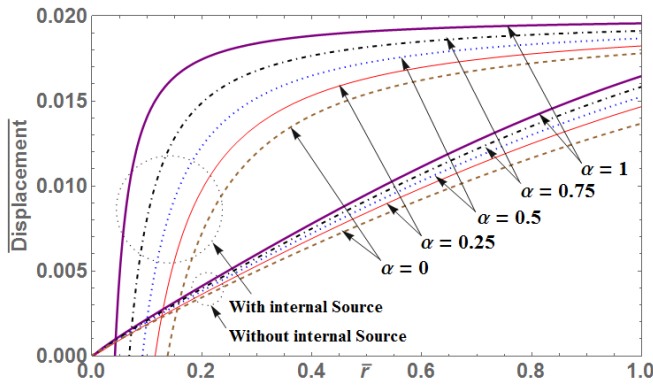
Figure 9. Variation of displacement $\bar{u}_r$ along the $\bar{r}$ direction for different α.
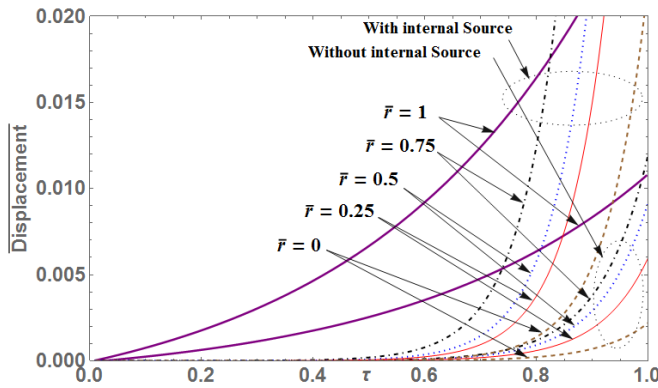

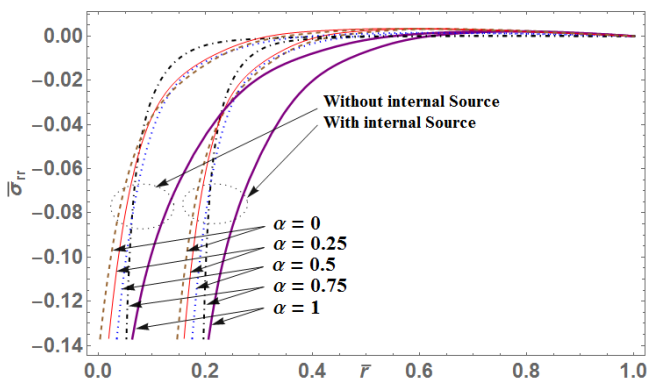Figure 10. Displacement distribution $\bar{u}_r$ along the τ direction for different $\bar{r}$.

Figure 11. $\bar{\sigma}_{rr}$ along $\bar{r}$ for different values of α ($\tau = 1$, $t = 1$).
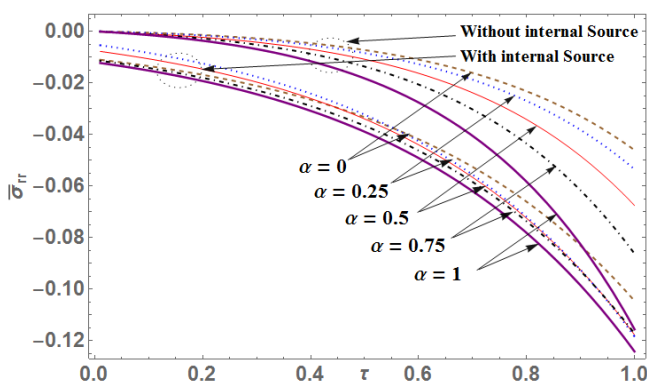

Figure 12. $\bar{\sigma}_{rr}$ profile along τ for various values of α ($\bar{r} = 0.4$, $t = 0.6$).
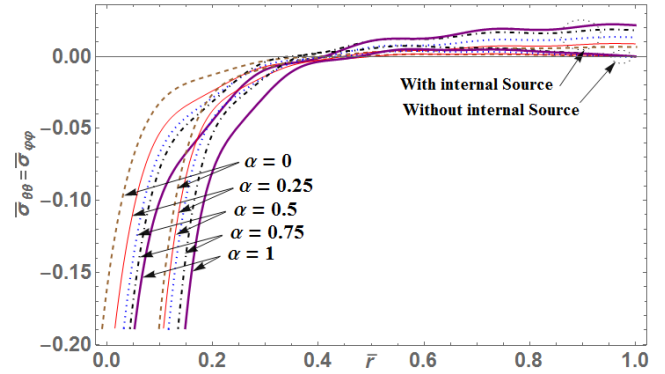

Figure 13. $\bar{\sigma}_{\theta\theta} = \bar{\sigma}_{\varphi\varphi}$ along $\bar{r}$ for different values of α ($\tau = 0.75$, $t = 1$).
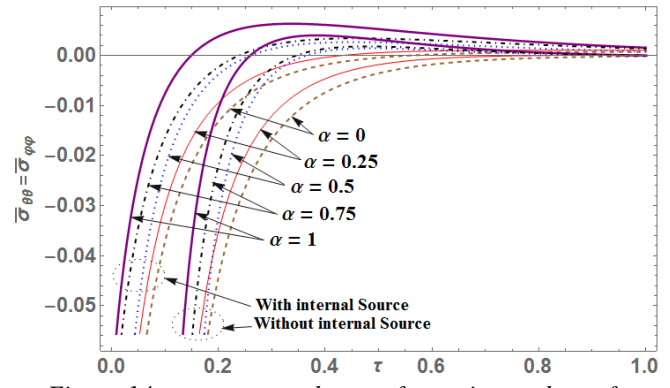

Figure 14. $\bar{\sigma}_{\theta\theta} = \bar{\sigma}_{\varphi\varphi}$ along τ for various values of α ($\bar{r} = 0.6$, $t = 0.8$).

Figure 10 shows the variation in the displacement distribution $\bar{u}_r$ along the τ direction for different values of $\bar{r}$ both availability or absence of an internal heat source. One can observe the change taking place in the displacement with an increase in the relaxation time. Initially, the displacement is none and slowly increases asymptotically due to the effect of the temperature distribution. Figure 11 depicts the relation between the radial stresses along the radial direction for the different values of α when $t = \tau = 1$ in both when internal heat sources are present or absent. In both cases, the difference in the stresses can be readily noticeable. The nature of the stresses is such that it starts accumulating stability at the ball's outer end with a gradual increase that can be seen from low initiation. Figure 12 gives variation in radial stresses along relaxation time for various values of α for both, with and without a heat source. The gradual decreasing nature in the plot can be observed at zero relaxation time no, or a negligible amount of stresses are found, which decreases as the relaxation time increases, ultimately defining the importance of relation time. Figures 13-14 show the relation between $\bar{\sigma}_{\theta\theta} = \bar{\sigma}_{\varphi\varphi}$ along $\bar{r}$ and τ for different values of α. The graph's nature is the same in both figures, with and without a heat source. The stresses' values are very low initially and increase slowly at the outer end due to the accumulation of the surrounding temperature.

4. Deduction And Validation Of The Results

This section corresponds to the deduction of results obtained above regarding the classical uncoupled thermoelasticity model and classical Cattaneo-Vernotte thermoelasticity theory for a homogeneous sphere.

(i)   Taking $\tau = 0$ and $\alpha = 1$ in Eq. (7), the equation reduces to the classical Fourier heat conduction model [30].

(ii)   Taking $\alpha = 1$ in Eq. (7), the equation results in the classical Cattaneo-Vernotte heat conduction model [19,20].

The present deduced thermoelastic solutions agree with the key derived by Ghonge and Ghadle [41] for an isotropic, homogeneous, elastic sphere. This work combines a fractional-order constitutive model with the standard continuity equation. However, recent investigations [47,48] show the coexistence of the non-Fourier constitutive model and non-trivial continuity equation based on the Boltzmann transport theory. The results illustrate that the constitutive model and continuity equation are not independent of each other, which is not considered in this work.

4. Conclusion

In this problem, the fractional Cattaneo model is derived for studying the thermoelastic response of a rigid ball that is internally impacted by an assigned temperature. At the same time, heat supply is a source in the energy equation. The theory of integral transformation is used to obtain the analytical solution for the fractional Cattaneo and classical Fourier models. The temperature distribution dependence and its thermoelastic response on the fractional-order parameter and relaxation time are studied for different times and positions. It is observed that the fractional Cattaneo model gives continuous temperature and thermal stress variation irrespective of the fractional-order parameter. It is also detected that the heat flux flows from higher temperatures to lower for the fractional Cattaneo and classical Fourier models.

Nomenclature
α_t *linear coefficient of thermal expansion ($/^0C$)*
κ *thermal diffusivity ($m^2 s^{-1}$)*
λ *thermal conductivity (W/m.K)*
Greek symbols
μ *Lame's constants (GPa)*
ν *Poisson's ratio*
ρ *density (kg/m3)*
u_{ij} *displacement potential function*
σ_{ij} *components of stress tensor*
σ_{rr} *radial stress (Pa)*
$\sigma_{\theta\theta}$ *circumferential stress (Pa)*

Appendix
The Transformation And Its Essential Property
Here, the Fourier-Bessel series and Hankel transform [42] to spherical coordinates [43] are extended, which is more suitable to third-kind boundary conditions. Assuming a finite interval $0 < r < a$ in the spherical coordinate led to the spherical-Bessel series representation of a function $f(r)$, which can be stated as

$$f(r) = \sum_{i=1}^{\infty} c_i \, J_n(r\,k_i) \qquad (A.1)$$

where c_i are the coefficients to be determined and $J_n(r\,k_i)$ is a spherical Bessel function of order n. The eigenvalues $k_i = \alpha_i / a$ are defined by the solutions of

$$k_i J_n'(ak_i) + h J_n(ak_i) = (\alpha_i / a) J_n'(\alpha_i) + h J_n(\alpha_i) = 0 \qquad (A.2)$$

in which α_i is an ith root of the spherical Bessel function, and the prime denotes the differentiation of the Bessel function. Multiplying Eq. (A.1) by $J_n(r\,k_j)$, integrating both sides of the result from 0 to a, and using the orthogonal property of Bessel functions, then taking $n = 0$, one obtains

$$\int_0^a f(r) J_0(r\,k_i)\, r^2 dr = \frac{c_i \, \pi}{2k_i} \int_0^a [J_{1/2}(r\,k_i)]^2 \, r \, dr \qquad (A.3)$$

Following the procedure of Chen [43], one obtains the series coefficients as

$$c_i = \frac{4}{\pi a^2} \frac{k_i}{[J_{1/2}'(\alpha_i)]^2} \int_0^a f(r) J_0(r\,k_i)\, r^2 dr \qquad (A.4)$$

Substituting the value of c_i into Eq. (1) gives

$$f(r) = \left(\frac{4}{\pi a^2}\right) \sum_{i=1}^{\infty} \frac{k_i}{[J_{1/2}'(\alpha_i)]^2} \int_0^a f(r) J_0(rk_i) r^2 dr \qquad (A.5)$$

Thus, the zero-order finite Hankel transform and its inverse are defined as

$$\bar{f}(k_i) = \int_0^a f(r) J_0(r\,k_i)\, r^2 dr \qquad (A.6)$$

$$f(r) = \left(\frac{4}{\pi a^2}\right) \sum_{i=1}^{\infty} \frac{k_i^2 \bar{f}(k_i)}{h^2 + k_i^2} \frac{J_0(r\,k_i)}{[J_{1/2}'(\alpha_i)]^2} \qquad (A.7)$$

and the only property which will be made use

$$\mathfrak{A}_0 \left\{ \frac{\partial^2 f}{\partial r^2} + \frac{2}{r} \frac{\partial f}{\partial r} \right\} = -k_i^2 \bar{f} + a J_0(ak_i) \left[\frac{\partial f}{\partial r} + hf \right]_{r=a} \qquad (A.8)$$

References:

[1] G. Stolz, "Numerical solutions to an inverse problem of heat conduction for simple shapes," *J. Heat Transfer*, 82, 20-25, 1960. DOI: 10.1115/1.3679871.

[2] D. Necsulescu (2009) *Advanced Mechatronics: Monitoring and Control of Spatially Distributed Systems*, Singapore: World Scientific Company.

[3] K. Woodbury (2003) *Inverse Engineering Handbook*, Boca Raton: CRC Press.

[4] M. Ozisik and H. Orlande (2000) *Inverse Heat Transfer: Fundamentals and Applications*, New York ; Taylor & Francis.

[5] J. Beck, B. Blackwell and JR Charles (1985) *Inverse Heat Conduction: Ill-posed Problems*. New York; John Willey & Sons.

[6] L. Torsten, A. Mhamdi, and W. Marquardt, "Design, formulation, and solution of multidimensional inverse heat conduction problems," *Numer. Heat Tr-B Fund.*, 47, 111 - 133, 2005. DOI: 10.1080/10407790590883351.

[7] X. Lu and P. Tervola, "Transient heat conduction in the composite slab-analytical method," *J Phys Math Gen*, 38, 81-96, 2005. DOI: 10.1088/0305-4470/38/1/005.

[8] K. W. Khobragade, V. Varghese and N. W. Khobragade, "An inverse transient thermoelastic problem of a thin annular disc," *Appl. Math. E-Notes*, 6, 17-25, 2006.

[9] P. L. Woodfield, M. Monde, and Y. Mitsutake, "Improved analytical solution for inverse heat conduction problems on thermally thick and semi-infinite solids," *Int. J. Heat Mass Transfer*, 49, 2864-2876, 2006. DOI: 10.1016/j.ijheatmasstransfer.2006.01.050.

[10] R. Pourgholi, and M. Rostamian, "A numerical technique for solving IHCPs using Tikhonov Regularization Method," *Appl. Math. Model*, 34, 2102-2110, 2010. DOI: 10.1016/j.apm.2009.10.022.

[11] S. Danaila, and A. Chira, "Mathematical and numerical modeling of inverse heat conduction problem," *INCAS BULLETIN*, 6, 23–39, 2014. DOI: 10.13111/2066-8201.2014.6.4.3.

[12] M. Ivanchov and N. Kinash, "Inverse problem for the heat-conduction equation in a rectangular domain," *Ukr. Math. J.*, 69, 2018.DOI: 10.1007/s11253-018-1476-1.

[13] H. Chen, I. Jay, J. Frankel, and M. Keyhani, "Nonlinear inverse heat conduction problem of surface temperature estimation by calibration integral equation method," *Numer. Heat Tr-B Fund.*, 73, 263–291, 2018. DOI: 10.1080/10407790.2018.1464316.

[14] C. Chang, C. Liu, and C. Wang, "Review of computational schemes in inverse heat conduction problems," *Smart Sci.*, 6, 94–103, 2018. DOI: 10.1080/23080477.2017.1408987.

[15] S. Kukla and U. Siedlecka, "Laplace transform solution of the problem of time-fractional heat conduction in a two-Layer slab," *J. Appl. Comput. Mech.*, 14, 105-113, 2015.DOI: 10.17512/jamcm.2015.4.10.

[16] E. Hoashi, T. Yokomine, A. Shimizu, and T. Kunugi, "Numerical analysis of wave-type heat transfer propagating in a thin foil irradiated by short-pulsed laser," *Int. J. Heat Mass Transf.*, 46, 4083–4095, 2003. DOI: 10.1016/S0017-9310(03)00225-4.

[17] X. Ai and B. Q. Li, "Numerical simulation of thermal wave propagation during laser processing of thin films," *J. Electron. Mater.*, 34, 583–591, 2005. DOI: 10.1007/s11664-005-0069-6.

[18] T. T. Lam and E. Fong, "Application of solution structure theorem to non-Fourier heat conduction problems: Analytical approach," *Int. J. Heat Mass Transf.*, 54, 4796–4806, 2011. DOI: 10.1016/j.ijheatmasstransfer.2011.06.028.

[19] T. T. Lam, "A unified solution of several heat conduction models," *Int. J. Heat Mass Transf.*, 56, 653–666, 2013. DOI: 10.1016/j.ijheatmasstransfer.2012.08.055.

[20] C. Cattaneo, "Sur uneForme de I'equation de la Chaleur Eliminant le Paradoxed'une Propagation Instantanee'," *ComptesRendus de l'Académie des Sciences*, 247, 431-433, 1958.

[21] P. Vernotte, "Les paradoxes de la théorie continue de l'équation de la chaleur," *C. R. Acad. Sci. Paris*, 246, 3154-3155, 1958.

[22] A. Compte and R. Metzier, "The generalized Cattaneo equation for the description of anomalous transport processes," *J. Phys. A: Math. Gen.*, 30, 7277-7289, 1997.

[23] Y. Z. Povstenko, "Fractional Cattaneo-type equations and generalized thermoela-sticity," *J. Therm. Stresses*, 34, 97-114, 2011. DOI: 10.1080/01495739.2010.511931

[24] T. N. Mishra and K. N. Rai, "Numerical solution of FSPL heat conduction equation for analysis of thermal propagation," *Appl. Math. Comput.*, 273, 1006–1017, 2016. DOI: 10.1016/j.amc.2015.10.082.

[25] H.-T. Qi, H.-Y. Xu, and X.-W. Guo, "The Cattaneo-type time fractional heat conduction equation for laser heating," *Comput. Math. Appl.*, 66, 824–831, 2013. DOI: 10.1016/j.camwa.2012.11.021.

[26] H. T. Qi, H. Y. Xu and X. W. Guo, "The Cattaneo-type time fractional heat conduction equation for laser heating," *Comput. Math. Appl.*, 66, 824–831, 2013. DOI: 10.1016/j.camwa.2012.11.021

[27] H. T. Qi, and X.W. Guo, "Transient fractional heat conduction with generalized Cattaneo model," *Int. J. Heat Mass Transfer*, 76, 535–539, 2014. DOI: 10.1016/j.ijheatmasstransfer.2013.12.086.

[28] H. Y. Xu, H. T. Qi, and X. Y. Jiang, "Fractional Cattaneo heat equation in a semi-infinite medium," *Chin. Phys. B*, 22, 014401, 2013. DOI: 10.1088/1674-1056/22/1/014401

[29] G. Y. Xu, J. B. Wang, and Z. Han, "Study on the transient temperature field based on the fractional heat conduction equation for laser heating," *Appl. Math. Mech.*, 36, 844–849, 2015.

[30] H. R. Ghazizadeh, M. Maerefat, and A. Azimi, "Explicit and implicit finite difference schemes for fractional Cattaneo equation," *J. Comput. Phys.*, 229, 7042–7057, 2010. DOI: 10.1016/j.jcp.2010.05.039.

[31] M. N. Özisik (1993) *Heat Conduction*, John Wiley & Sons, New York.

[32] D. Y. Tzou, "Thermal shock phenomena under high rate response in solids," *Ann. Rev. Heat Transf.*, 4, 111–185, 1992. DOI: 10.1615/AnnualRevHeatTransfer.v4.50

[33] M. E. Gurtin and A. C. Pipkin, "A general theory of heat conduction with finite wave speeds," *Arch. Rational Mech. Anal.*, 31, 113–126, 1968. DOI: 10.1007/BF00281373

[34] A. Compte, A. Metzler, and J. Camacho, "Biased continuous time random walks between parallel plates," *Phys. Rev. E*, 56, No. 2, 1445-1454, 1997.

[35] M. N. Özisik, D. Y. Tzou, "On the wave theory in heat conduction," *J. Heat Transf.*, 116, 526–535, 1994.DOI: 10.1115/1.2910903

[36] S. Kaliski, "Wave equations of thermoelasticity," *Bull. Acad. Polon. Sci. Ser. Sci. Techn.*, 13, 253-260, 1965.

[37] H. W. Lord and Y. Shulman, "A generalized dynamical theory of thermoelasticity," *J. Mech. Phys. Solids*, 15, 299-309, 1967.

[38] I. Podlubny (1999) *Fractional Differential Equations*, Academic Press, New York.

[39] Y. Povstenko, "Axisymmetric solutions to fractional diffusion-wave equation in a cylinder under Robin boundary condition," *Eur. Phys. J. Spec. Top.*, 222, 1767–1777, 2013. DOI: 10.1140/epjst/e2013-01962-4.

[40] Y. Z. Povstenko, "Axisymmetric Solutions to Time-Fractional Heat Conduction Equation in a Half-Space under Robin Boundary Conditions," *Int. J. Differ. Equ.*, 2012, 1–13, 2012. DOI: 10.1155/2012/154085.

[41] Y. Povstenko, "Fundamental solutions to the fractional heat conduction equation in a ball under Robin boundary condition," *Open Math.*, 12, 2014. DOI: 10.2478/s11533-013-0368-8.

[42] H. Beyer and S. Kempfle, "Definition of physically consistent damping laws with fractional derivatives," *ZAMM - J. Appl. Math. Mech.*, 75, 623–635, 1995. DOI: 10.1002/zamm.19950750820.

[43] N. Noda, R. B. Hetnarski, and Y. Tanigawa (2003) *Thermal stresses*, *2nd Ed.*, Taylor and Francis, New York, 2003.

[44] B.E. Ghonge and K.P. Ghadle, "An inverse transient thermoelastic problem of solid sphere," *Bulletin of Pure and Applied Sciences*, 29, 1-9, 2010.

[45] I. N. Snedden (1972) *The Use of Integral Transforms*, McGraw-Hill Book Co., New York.

[46] I. H. Chen, "Modified Fourier- Bessel series and finite spherical Hankel transform," *Int. J. Math. Educ. Sci. Technol.*, 13, No. 3, 281-283, 1982. DOI: 10.1080/0020739820130307

[47] S. N. Li, B.Y. Cao, "Fractional Boltzmann transport equation for anomalous heat transport and divergent thermal conductivity," *Int. J. Heat Mass Transf.*, 137, 84-89, 2019.

[48] S. N. Li, B.Y. Cao, "Fractional-order heat conduction models from generalized Boltzmann transport equation," *Philos. Trans. R. Soc. A*, 378, 20190280, 2020.

Research Article

Thermodynamic Properties of Ethanol + Pyridine, Ethanol + Benzene, and Pyridine + Benzene Mixtures at Temperature 298.15 K and Under Atmospheric Pressure

[1,2]A. Zeqiraj [ID], [2]A. Gjevori [ID], [2]A. Llozana [ID], [3]N. Syla [ID], [4]*F. Aliaj [ID]

[1] University of Mitrovica, Department of Materials and Metallurgy, PIM-Trepça, 40000 Mitrovica, Kosovo
[2] Polytechnic University of Tirana, Department of Physical Engineering, Mother Theresa Square No. 4, Tirana, 1000 Albania
[3,4] University of Prishtina, Department of Physics, Eqrem Çabej Str. 51, 10000 Prishtina, Kosovo
E-mail: [4]*fisnik.aliaj@uni-pr.edu

Abstract

Experimental densities, viscosities, refractive indices, and sound speeds at temperature 298.15 K and atmospheric pressure are reported for the binary liquid mixtures of ethanol + benzene, ethanol + pyridine, and benzene + pyridine. From these experimental data, various thermodynamic excess and deviation properties were calculated and fitted by the Redlich-Kister polynomial to determine the adjustable coefficients and the standard deviations. The number of Redlich-Kister coefficients for significantly representing each thermodynamic property was optimized by applying the F-test. The variation of thermodynamic excess and deviation properties with composition has been interpreted in terms of molecular interactions between components of the mixture and structural effects. Furthermore, several theoretical and semi-empirical models were used to predict the refractive indices and sound speeds of the investigated mixtures. The predicting ability of each model was ascertained in terms of mean absolute percentage deviation between experimental and calculated data.

Keywords: Redlich-Kister polynomials; thermodynamic properties; binary mixtures; refractive index; sound speed; F-test.

1. Introduction

The work described in this paper belongs to a systematic study program concerning the measurement and mathematical description of various thermodynamic properties of binary and ternary liquid mixtures containing important compounds [1-3]. The study of thermodynamic properties of binary mixtures of alkanols with aromatics is of great importance both from a practical and theoretical point of view. For example, an increase in the conversion of refined coal and oil yield is observed when raw mined coal is thermally pretreated with a mixture of benzene and ethanol [4]. A mixture of benzene with ethanol is also widely used to extract volatiles in the pulp and paper industry and diesel exhaust particulates [5]. On the other hand, applying pyridine as a fuel additive has improved the coking resistance of SOFCs with Ni cermet anode operating on ethanol fuels [6]. Thorough knowledge of liquid mixtures' thermodynamic properties is also essential for the design and setup of separation processes and process equipment. It will contribute to the fundamental understanding of complex molecular interactions between mixtures' components and, thus, a better understanding of liquid state theory [7-10].

Here we report experimental densities, sound speeds, viscosities, and refractive indices of binary mixtures ethanol + pyridine, ethanol + benzene, and pyridine + benzene at 298.15 K and under atmospheric pressure of 950 hPa. The related thermodynamic properties – excess molar volume, excess Gibbs free energy of activation for viscous flow, isentropic compressibility deviations, and refractive index deviations – have been calculated from the experimental data and interpreted in terms of molecular interactions between components of the mixture and structural effects.

The studied thermodynamic properties were fitted by Redlich-Kister polynomials [11], which is one of the most popular expressions for the mathematical representation of excess thermodynamic properties of binary liquid mixtures. Additionally, various theoretical and semi-empirical models were used to predict the refractive indices [12-17] and sound speeds [18-22] of the investigated liquids mixtures. The predicting ability of each model was ascertained in terms of mean absolute percentage deviation between experimental and calculated data.

A review of literature revealed that some thermodynamic properties of the investigated mixtures had been reported [5, 8, 9, 23-25]. However, this work is the first to report a combined study of density, sound speed, viscosity, and refractive index (and their derived thermodynamic excess and deviation properties) for three organic liquids and their binary mixtures of practical importance in various chemical and industrial processes.

*Corresponding Author

2. Materials and Methods

2.1 Materials

Ethanol (Carlo Erba) was supplied with purity ≥99.8%, benzene (Lach-Ner) with ≥99.8%, and pyridine (Sigma-Aldrich) with ≥99.5%. Densities (kg· m^{-3}), sound speeds (m· s^{-1}), viscosities (mPa· s), and refractive indices of pure liquids are within 0.05%, 0.08%, 0.8%, and 0.008%, respectively, with the corresponding literature values [8, 10, 26-32]. Since the agreement with the literature is very good, all the chemicals were used without further purification.

2.2 Methods

Mixtures were prepared by syringing known masses of the pure liquids into airtight stoppered amber glass bottles. Preferential evaporation during the preparation of mixtures was minimized by always charging the higher-boiling component first. Precautions were also taken to avoid losses by evaporation during manipulation. A KERN & Sohn ABS220-4N type electronic balance with a precision of ±0.1 mg was used for mass measurements. Conversion from mass to molar quantities was based on IUPAC's relative atomic mass Table of 2011 [33]. The uncertainty in the mole fraction of the studied mixtures was estimated to be better than ±0.0001. All mixtures were prepared just before use for measurements of density (ρ), speed of sound (c), viscosity (η), and refractive index (n) at temperature 298.15 K and ambient pressure of ~95.0 kPa.

This work used a pycnometer made of borosilicate glass to determine the densities of pure liquids and liquid mixtures. The pycnometer volume was calibrated at 298.15 K with in-house triple distilled and bubble-free water. Utmost care was taken while filling the pycnometer with sample liquid such that no air bubbles were trapped in the bulb or capillary of the pycnometer. The pycnometer with sample liquid was immersed for 30 minutes in a water bath maintained at 298.15 ± 0.04 K to minimize temperature fluctuations. After temperature equilibration, the pycnometer was dried with filter paper before recording its mass in an electronic balance. The density of the sample liquid was then calculated using the values of its mass and volume. The reported densities represent averages over three measurements.

A variable path single-crystal ultrasonic interferometer operating at 2 MHz (Mittal model SE-02) was used to measure sound speed (c). In-house triple-distilled and bubble-free water was used to check the performance of the interferometer. The speed of sound for water at 298.15 K was 1497 ± 1 m·s^{-1}, which agrees very well with values reported in the literature [30, 32]. Thermal control of the sample liquids was performed by circulating water from a bath maintained at 298.15 ± 0.04 K through the inner walls of the measuring cell of the interferometer. The reported sound speeds are average values taken over ten measurements.

The dynamic viscosities were determined with calibrated Cannon-Fenske capillary viscometer. Much effort was put into ensuring that the capillary was vertical while mounting the viscometer in a water bath controlled at 298.15 ± 0.04 K. The viscometer with the sample liquid was kept for 30 minutes in the water bath before making the flow-time measurements. A digital stopwatch with a readability of 0.01 s was used for flow-time measurements. Measurements were repeated at least five times, and average values were considered in all calculations.

Refractive indices of pure liquids and binary mixtures were measured with an Abbe refractometer operated with a low-pressure sodium vapor lamp (λ = 589 nm). The refractometer was thermostatically controlled at 298.15 ± 0.04 K. Regular calibration checks were performed with in-house triple distilled water to ensure the accuracy of the measurements. At least three independent measurements were performed for each sample, and the average value was considered in all calculations.

The combined expanded uncertainties at a 95% confidence level for ρ, c, η, and n measurements are 0.2 kg·m^{-3}, 2 m·s^{-1}, 0.003 mPa·s, and 0.0002, respectively. The corresponding uncertainties were calculated following the NIST guidelines for evaluating and expressing uncertainties of measurement results [34].

3. Results and Discussion

The measured physical properties (ρ, c, η, and n) at temperature 298.15 K and ambient pressure ~95.0 kPa of the studied mixtures appear in Tables 1 to 3. The experimental results reveal that in the mixtures of pyridine or benzene with ethanol, the density, sound speed, and refractive index decrease with the mole fraction of ethanol (x_1). A second-order degree polynomial on x_1 can satisfactorily represent these properties. On contrary, dynamic viscosity data show a minimum around x_1 = 0.35 and 0.10 for ethanol (1) + pyridine (2) and ethanol (1) + benzene (2) mixtures, respectively. For the pyridine (1) + benzene (2) system, the ρ, c, and η data exhibit a nearly linear relationship with composition, while the n data show a second-order degree variation.

The excess molar volumes, V^E, excess Gibbs free energies of activation for viscous flow, G^{*E}, refractive index deviations, Δn, and isentropic compressibility deviations, $\Delta\kappa_S$, were derived from ρ, c, η, and n values by using the following equations [2, 9, 10, 35]:

$$V^E = \sum_{i=1}^2 x_i M_i (\rho^{-1} - \rho_i^{-1}), \tag{1}$$

$$G^{*E} = RT\big[\ln(\eta V_m) - \sum_{i=1}^2 x_i \ln(\eta_i V_{m,i})\big], \tag{2}$$

$$\Delta\kappa_S = \kappa_S - \sum_{i=1}^2 \varphi_i \kappa_{S,i}, \tag{3}$$

$$\Delta n = n - \sum_{i=1}^2 \varphi_i n_i, \tag{4}$$

$$\varphi_i = \left(\frac{x_i M_i \rho_i^{-1}}{\sum_j x_j M_j \rho_j^{-1}}\right). \tag{5}$$

where $\kappa_S = \rho^{-1} c^{-2}$ is the isentropic compressibility of the mixture; x_i, M_i, ρ_i, η_i, $\kappa_{S,i} = \rho_i^{-1} c_i^{-2}$, n_i, and φ_i, are the mole fraction, molar mass, density, dynamic viscosity, isentropic compressibility, refractive index, and volume fraction of pure component i, respectively. R is the universal gas constant. Other symbols have the usual meaning. The combined expanded uncertainties at a 95% confidence level are $U_c(V^E) = 0.006$ cm^3·mol^{-1}, $U_c(G^{*E}) = 11$ J·mol^{-1}, $U_c(\Delta\kappa_s) = 1.6$ TPa^{-1}, and $U_c(\Delta n) = 0.0002$. The V^E, G^{E*}, Δn, and $\Delta\kappa_S$ results of the studied mixtures are graphically shown in Figures 1, 2, 3, and 4, respectively. The literature values are also shown [5, 8, 23-25, 36, 37] for comparison purposes.

We can observe that the V^E results of this work for ethanol + benzene agree well with those reported by Han et al. [8] and Šerbanović et al. [5] over the entire composition range. A small discrepancy is observed between the V^E of Garrett and Pollock [23] and the results of this work for pyridine + benzene at the middle mole fraction region. The data of Findlay and Copp [25] present good agreement for

ethanol + pyridine over the entire composition range. However, the results of Singh et al. [36] are lower in the middle fraction region, probably because of the higher measurement temperature. From Figure 2 it can be seen that for ethanol + benzene the G^{*E} of this work agrees well with those reported by Kouris and Panayiotou [37] over the whole composition range. We can observe from Figure 3 that our $\Delta\kappa_S$ data for ethanol + benzene show good agreement up to ~0.7 mole fraction of ethanol but deviate with those of Gonzales-Olmos et al. [24] at higher compositions.

Because of the different natures of benzene, pyridine, and ethanol—in terms of polarity and geometrical shape—the resulting values of thermodynamic properties of their mixtures will reflect the opposite contributions that are dominant in certain regions of the concentrations. When these compounds are mixed, then the observed changes in thermodynamic properties are clearly due to: (*i*) stretching and breaking of H bonded structures in pure ethanol, (*ii*) N•••HO interactions between the lone pair of electrons of N in pyridine and the OH group of ethanol, (*iii*) π•••HO interactions between the π electrons of the aromatic rings (of pyridine and benzene) and the OH group of ethanol, (*iv*) π•••H interactions between the partial positive charge of H – in the position *para* with N - of pyridine with π electrons of aromatic rings, (*v*) geometrical interstitial accommodation of molecules into each other's structure due to differences in size and shape of the component molecules of the mixtures; (*vi*) in all cases weak London dispersion interactions are also present [5, 9, 38].

When considering V^E and $\Delta\kappa_S$, then it is known that contributions (*i*) and (*vi*) give positive values, while (*ii*) - (*v*) contribute negatively to the values of V^E and $\Delta\kappa_S$ [35, 38, 39]. Having in mind the various contributions operating in the studied systems, then the positive values of $\Delta\kappa_S$ and V^E in the benzene-rich region of the ethanol + benzene system (Figures 1 and 3) can be attributed mainly to the disruption of the H-bonded ethanol structures as the ethanol molecules are added to a large amount of benzene. The negative $\Delta\kappa_S$ and V^E values in the ethanol-rich region indicate that complex formation occurred through π···HO bonding between the π-electron cloud of the aromatic ring of benzene and the hydroxyl group of ethanol. A further negative contribution may occur from the interstitial accommodation of benzene molecules into the remaining H-bonded ethanol structure [35]. The negative V^E and $\Delta\kappa_S$ values for the ethanol + pyridine system can be attributed mainly to the formation of complexes by strong cross-associated N···HO interactions. Contributions (*iii*) and (*v*) may also play a role. Similar results are also obtained by Anwar et al. [38] for binary mixtures of pyridine with alkanols (C_6-C_{10}) and by Kijevčanin et al. [39] for mixtures of pyridine with 1-propanol and 1,2-propanediol.

Figure 2 shows that excess Gibbs free energy of activation for viscous flow G^{*E} is negative for mixtures involving ethanol but is positive for the system pyridine + benzene. Positive G^{*E} is generally observed in systems with strong specific interactions between mixture components. In contrast, negative values can be seen in binary mixtures where weak dispersion forces are primarily responsible for interaction but may also occur where components are known to interact more strongly [40, 41], as in our case of the ethanol + pyridine system. Similar results are observed for binary mixtures of alkanols with pyridine [35, 38] and N-methyl pyrrolidine [42].

Table 1. Densities ρ, speeds of sound c, dynamic viscosities η, and refractive indices n of ethanol (1) + pyridine (2) mixtures at 298.15 K and ~95.0 kPa.

x_1	ρ (kg·m^{-3})	c (m·s^{-1})	η (mPa·s)	n
0.0000	978.3	1417	0.879	1.5071
0.0229	975.2	1414	0.873	1.5047
0.0498	971.6	1410	0.866	1.5019
0.1000	964.7	1402	0.856	1.4966
0.1493	957.8	1394	0.850	1.4911
0.2000	950.6	1385	0.846	1.4854
0.2488	943.5	1376	0.843	1.4797
0.2999	935.7	1366	0.842	1.4735
0.3552	926.9	1355	0.841	1.4666
0.4000	919.4	1345	0.841	1.4608
0.5000	901.7	1321	0.848	1.4471
0.6000	882.5	1294	0.866	1.4324
0.7000	861.6	1264	0.897	1.4165
0.7454	851.5	1249	0.915	1.4089
0.8000	838.7	1229	0.940	1.3993
0.8349	830.0	1216	0.956	1.3929
0.9000	813.1	1190	0.992	1.3804
0.9258	806.2	1179	1.012	1.3753
0.9500	799.6	1168	1.032	1.3703
0.9778	791.7	1155	1.059	1.3644
1.0000	785.1	1145	1.082	1.3594

Table 2. Densities ρ, speeds of sound c, dynamic viscosities η, and refractive indices n of pyridine (1) + benzene (2) mixtures at 298.15 K and ~95.0 kPa.

x_1	ρ (kg·m^{-3})	c (m·s^{-1})	η (mPa·s)	n
0.0522	972.6	1411	0.865	1.5067
0.1000	967.4	1406	0.852	1.5063
0.1439	962.7	1402	0.841	1.5060
0.1999	956.8	1395	0.827	1.5056
0.2601	950.5	1389	0.810	1.5052
0.3001	946.3	1385	0.800	1.5049
0.3504	941.1	1379	0.786	1.5045
0.4001	935.9	1374	0.772	1.5042
0.4492	930.8	1368	0.759	1.5038
0.5001	925.5	1363	0.745	1.5034
0.5502	920.3	1357	0.731	1.5030
0.6000	915.1	1351	0.717	1.5025
0.6439	910.6	1346	0.705	1.5021
0.7000	904.8	1339	0.689	1.5015
0.7691	897.6	1330	0.669	1.5007
0.8000	894.4	1326	0.660	1.5004
0.8495	889.3	1319	0.646	1.4998
0.9000	884.0	1313	0.630	1.4991
0.9601	877.7	1305	0.613	1.4982
1.0000	873.4	1299	0.602	1.4976

Table 3. Densities ρ, speeds of sound c, dynamic viscosities η, and refractive indices n of ethanol (1) + benzene (2) mixtures at 298.15 K and ~95.0 kPa.

x_1	ρ (kg·m^{-3})	c (m·s^{-1})	η (mPa·s)	n
0.0227	871.8	1292	0.592	1.4954
0.0500	869.9	1285	0.584	1.4928
0.1000	866.6	1275	0.577	1.4878
0.1557	863.0	1265	0.581	1.4821
0.1999	860.0	1258	0.587	1.4774
0.2508	856.6	1251	0.594	1.4719
0.2998	853.2	1244	0.602	1.4664
0.3451	850.0	1238	0.614	1.4612
0.3998	846.0	1232	0.632	1.4546
0.4561	841.7	1225	0.651	1.4475
0.4998	838.2	1220	0.669	1.4418
0.5509	834.0	1214	0.694	1.4349
0.5998	829.7	1208	0.722	1.4280
0.6404	826.1	1203	0.746	1.4221
0.7000	820.4	1196	0.785	1.4130
0.7511	815.2	1189	0.825	1.4049
0.8000	810.0	1182	0.866	1.3968
0.8599	803.2	1173	0.920	1.3863
0.9000	798.4	1166	0.962	1.3790
0.9500	792.0	1156	1.025	1.3694
0.9778	788.2	1150	1.059	1.3639

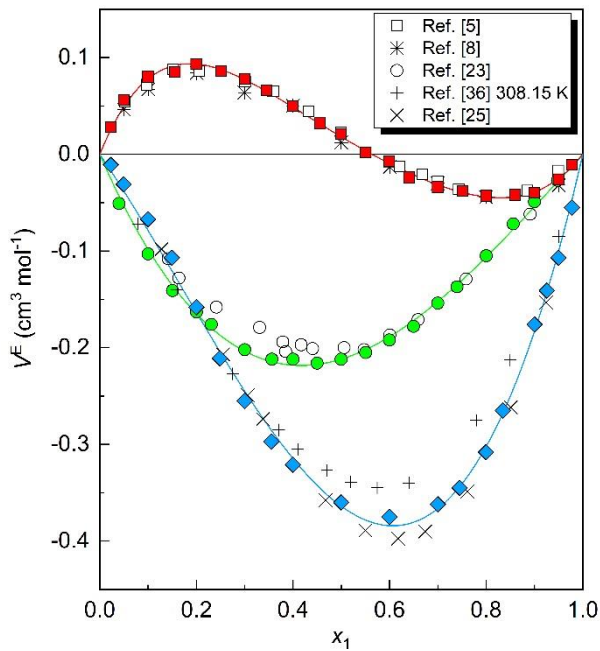*Figure 1. Excess molar volumes, V^E, for the □ ethanol (1) + benzene (2), □ pyridine (1) + benzene (2), and ♦ ethanol (1) + pyridine (2) binary mixtures. Solid lines are the results calculated from the Redlich-Kister polynomial [11]. (Figure is in color in the online version of the paper).*

Figure 3. Isentropic compressibility deviation, $\Delta \kappa_S$, for the □ ethanol (1) + benzene (2), □ pyridine (1) + benzene (2), and ♦ ethanol (1) + pyridine (2) binary mixtures. Solid lines are the results calculated from the Redlich-Kister polynomial [11]. (Figure is in color in the online version of the paper).

Figure 2. Excess Gibbs free energy of activation for viscous flow, G^{*E}, for the □ ethanol (1) + benzene (2), □ pyridine (1) + benzene (2), and ♦ ethanol (1) + pyridine (2) binary mixtures. Solid lines are the results calculated from the Redlich-Kister polynomial [11]. (Figure is in color in the online version of the paper).
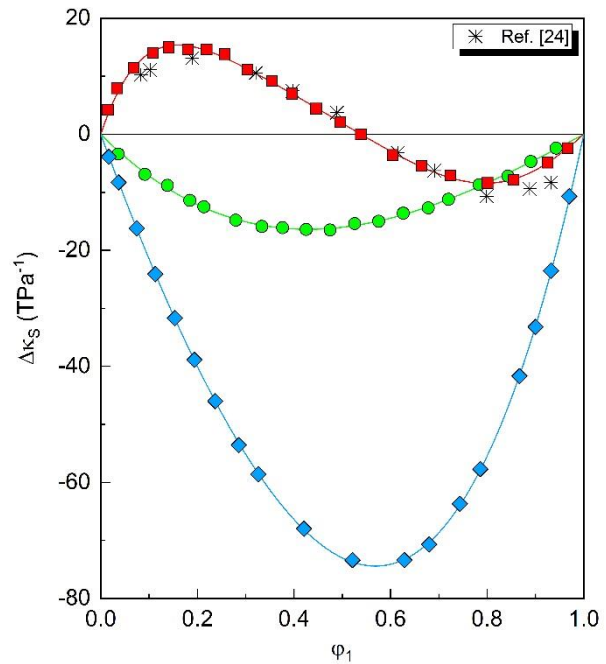

Figure 4. Refractive index deviation, Δn, for the □ ethanol (1) + benzene (2), □ pyridine (1) + benzene (2), and ♦ ethanol (1) + pyridine (2) binary mixtures. Solid lines are the results calculated from the Redlich-Kister polynomial [11]. (Figure is in color in the online version of the paper).
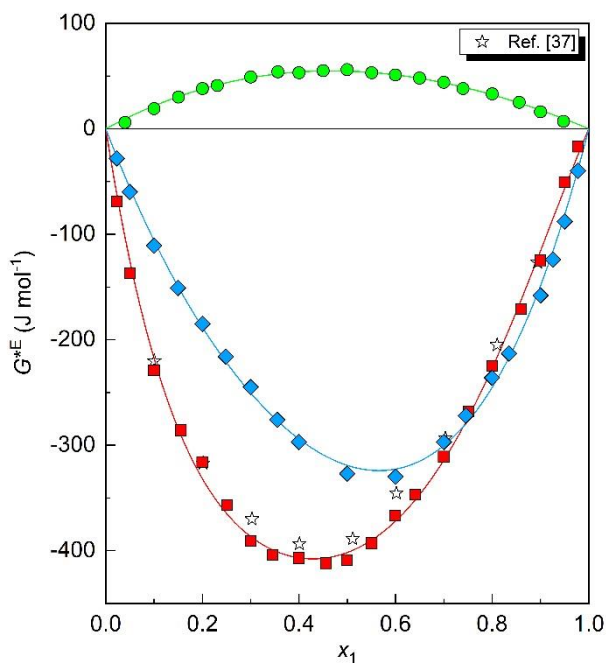
The variations of Δn with the volume fraction of the first component in the mixture are shown in Figure 4. The Δn shows negative dependence for the system ethanol (1) + benzene (2) but is positive for ethanol (1) + pyridine (2) and pyridine (1) + benzene (2). The data seem to support the finding that Δn tends to increase as the strength of interaction between the components of the mixture increases, thereby showing an opposite trend to that of V^E values. This negative correlation of Δn with V^E is a widely valid rule [3, 7, 38, 43], and it may be used as a quick check on the consistency of the data pertaining to V^E [43].

Table 4. Adjustable coefficients B_j and standard deviations of the fitting σ for mathematical representation with Redlich-

Kister polynomial, Eqn. (6), of excess molar volumes V^E (cm³·mol⁻¹), isentropic compressibility deviations $\Delta\kappa_S$ (TPa⁻¹), deviations in refractive indices Δn, and excess Gibbs free energy of activation for viscous flow G^{*E} (J·mol⁻¹) at 298.15 K.

Property Y	B_1	B_2	B_3	B_4	B_5	$\sigma(Y)$
ethanol + pyridine						
V^E	-1.456	0.723				0.008
$\Delta\kappa_s$	-292.0	80.4	-17.6			0.2
Δn	0.0091	-0.0021	0.0017	-0.0028		0.00003
G^{*E}	-1276	297	-218			6
ethanol + benzene						
V^E	0.073	0.592	0.226	0.342		0.003
$\Delta\kappa_s$	7.6	98.4	8.5	64.4	73.5	0.4
Δn	-0.0044	-0.0016				0.00003
G^{*E}	-1607	-339	-386	-577		8
pyridine + benzene						
V^E	-0.847	-0.306				0.004
$\Delta\kappa_s$	-64.1	-19.4				0.3
Δn	0.0050	0.0028				0.00004
G^{*E}	219	28				1

3.1 Correlation of V^E, $\Delta\kappa_S$, G^{*E} and Δn

The thermodynamic excess and deviation properties (V^E, $\Delta\kappa_S$, $G^{*E,}$ and Δn) of the studied mixtures were correlated by polynomials due to Redlich and Kister [11]:

$$Y = X_1 X_2 \sum_{j=0}^{k} B_j (X_2 - X_1)^j, \tag{6}$$

where k is the polynomial order optimized by applying the *F*-test [44] at a 0.01 significance level. The polynomial coefficients B_j were fitted by the unweighted least squares method and are recorded in Table 4 along with the standard deviations. $X = x$ (mole fraction) when fitting $Y = V^E$ and G^{*E}; $X = \phi$ (volume fraction) for $Y = \Delta\kappa_S$ and Δn. The subscripts 1 and 2 refer to the first and second components in the corresponding binary mixture.

The solid lines in Figures 1 to 4 refer to the values calculated with Eq. (6) using the corresponding coefficients B_j in Table 4. We can observe a good agreement between the experimental data and the solid lines generated with an optimal number of coefficients. Generally, the number of fitting coefficients depends on the shape of data across the graph, the number of data points, the experimental data quality, and the significance level [35]. E.g., more parameters were needed to significantly fit the $\Delta\kappa_S$ and V^E data of the ethanol + benzene system as they exhibited sine-like behavior. When data show a parabolic-like dependence, fewer parameters are needed to fit them significantly.

3.2 Predictive Models for n and c

Information on refractive index and speed of sound is essential for designing and optimizing multi-component liquid mixtures. The invaluable information provided by these properties has considerably increased the interest in applying different models for predicting them. In this work, Lorentz and Lorenz (L-L) [12], Eykman (EYK) [13], Oster (OST) [14], Dale and Gladstone (D-G) [13, 15, 17], and Newton (NEW) [16] mixing rules were used to predict the refractive indices of the studied systems:

Lorentz-Lorenz (L-L):
$$\frac{n^2-1}{n^2+2} = \sum_{i=1}^{2} \phi_i \frac{n_i^2-1}{n_i^2+2} \tag{7}$$

Eykman (EYK):
$$\frac{n^2-1}{n+0.4} = \sum_{i=1}^{2} \phi_i \frac{n_i^2-1}{n_i+0.4} \tag{8}$$

Oster (OST):
$$\frac{(n^2-1)(2n^2+1)}{n^2} = \sum_{i=1}^{2} \phi_i \frac{(n_i^2-1)(2n_i^2+1)}{n_i^2} \tag{9}$$

Dale-Gladstone (D-G):
$$n - 1 = \sum_{i=1}^{2} \phi_i (n-1) \tag{10}$$

Newton (NEW):
$$n^2 - 1 = \sum_{i=1}^{2} \phi_i (n_i^2 - 1) \tag{11}$$

In Eqs. (7)-(11), n and n_i are the refractive indices of the liquid mixture and pure component i, respectively; ϕ_i is the volume fraction of component i in the mixture.

For predicting sound speeds, the relations of Nomoto (NOM) [18], van Dael (VAN) [19], Ernst et al. (ERN) [20], Junjie (JUN) [21], and Rao [22] were used. The formulae pertaining to these relations, which were subjected to proper rearrangement, are given in the following:

Nomoto's relation:
$$V^{id} c^{1/3} = \sum_{i=1}^{2} x_i V_i c_i^{1/3} \quad \therefore \quad c = \left[(V^{id})^{-1} \sum_{i=1}^{2} x_i V_i c_i^{1/3} \right]^3 \tag{12}$$

where c is the speed of sound in the mixture, $V^{id} = \sum_{i=1}^{2} x_i V_i$; x_i, V_i, and c_i, are the mole fractions, molar volumes, and sound speeds of component i in the mixture.

van Dael's ideal mixing relation:
$$(M c^2)^{-1} = \sum_{i=1}^{2} x_i (M_i c_i^2)^{-1} \quad \therefore \quad c = [M \sum_{i=1}^{2} x_i (M_i c_i^2)^{-1}]^{-1/2} \tag{13}$$

where c and M are the speed of sound and molar mass, respectively, of liquid mixture; x_i, M_i, and c_i, are the mole fractions, molar masses, and sound speeds of component i in the mixture.

Ernst et al. relation:
$$(c)^{-1} = \sum_{i=1}^{2} \phi_i (c_i)^{-1} \quad \therefore \quad c = [\sum_{i=1}^{2} \phi_i (c_i)^{-1}]^{-1} \tag{14}$$

where c is the speed of sound of liquid mixture; ϕ_i, and c_i, are the volume fractions and speeds of sound, respectively, of component i in the mixture.

Junjie's relation:
$$\left(V^{id} M^{-1/2} c^{-1} \right)^2 = \sum_{i=1}^{2} x_i \left(V_i M_i^{-1/2} c_i^{-1} \right)^2 \quad \therefore \quad c = \left[(V^{id})^{-2} M \sum_{i=1}^{2} x_i \left(V_i M_i^{-1/2} c_i^{-1} \right)^2 \right]^{-1/2} \tag{15}$$

where c and M are the speed of sound and molar mass, respectively, of the liquid mixture, and $V^{id} = \sum_{i=1}^{2} x_i V_i$; x_i, M_i, V_i, and c_i, are the mole fractions, molar masses, molar volumes, and sound speeds of component i in the mixture.

Rao's relation:
$$\rho^{-1} c^{1/3} = \sum_{i=1}^{2} x_i \rho_i^{-1} c_i^{1/3} \quad \therefore \quad c = \left[\rho \sum_{i=1}^{2} x_i \rho_i^{-1} c_i^{1/3} \right]^3 \tag{16}$$

where c and ρ are the speed of sound and density, respectively, of liquid mixture; x_i, ρ_i, and c_i, are the mole fractions, density, and sound speeds, respectively, of components i in the mixture.

The ability of the models to predict refractive indices and sound speeds of investigated systems was tested by calculating the mean absolute percentage deviation (MAPD) [45] between experimental and predicted values. The MAPD results are summarized in Tables 5 and 6 for refractive indices and speeds of sound, respectively.

Table 5. Mean absolute percentage deviation (MAPD) for the Lorentz–Lorenz (L–L), Eykman (EYK), Newton (NEW), Oster (OST), and Dale–Gladstone (D–G) mixing rules for ethanol + pyridine, pyridine + benzene, and ethanol + benzene mixtures at 298.15 K

System	L-L	EYK	NEW	D-G	OST
ethanol + pyridine	0.172	0.118	0.019	0.094	0.051
pyridine + benzene	0.059	0.059	0.058	0.058	0.058
ethanol + benzene	0.026	0.026	0.123	0.049	0.091

Table 6. Mean absolute percentage deviation (MAPD) for the Nomoto (NOM), Van Dael (VAN), Ernst et al. (ERN), Rao, and Junjie (JUN) relations for ethanol + pyridine, pyridine + benzene, and ethanol + benzene mixtures at 298.15 K

System	NOM	VAN	ERN	Rao	JUN
ethanol + pyridine	1.05	6.26	2.43	3.39	2.78
pyridine + benzene	0.43	0.45	0.36	0.15	0.86
ethanol + benzene	0.90	3.45	0.45	2.50	0.49

Table 5 shows that all the mixing rules performed well for the systems under study. The NEW mixing rule shows the best agreement with experimental values for the ethanol + pyridine system but the worst agreement for ethanol + benzene. The observed deviations are expected and can be accounted for, to some degree, if the excess volume is taken into consideration in the various mixing rules [7, 46]. Based on MAPD data, the predicting ability of the mixing rules follows this sequence: EYK ≈ L-L > D-G > OST > NEW for ethanol + benzene; NEW > OST > D-G > EYK > L-L for ethanol + pyridine. All the mixing rules obviously performed equally well for the pyridine + benzene system.

From a perusal of Table 6, it is obvious that some relations did not present good agreement with experimental data. The VAN relation resulted in the highest disagreement with experimental data for ethanol + pyridine, whereas the Rao relation showed the best performance for pyridine + benzene. Based on the results of Table 6, the predicting ability of the speed of sound relations follows the sequence: NOM > ERN > JUN > Rao > VAN for ethanol + pyridine; Rao > ERN > NOM > VAN > JUN for pyridine + benzene; ERN > JUN > NOM > Rao > VAN for ethanol + benzene.

4. Conclusions

This paper reports a combined experimental study of density, sound speed, viscosity, and refractive index (and their derived thermodynamic excess and deviation properties V^E, G^{E*}, Δn, and $\Delta\kappa_S$) for pure liquids - ethanol, benzene, and pyridine - and their binary mixtures essential for various chemical and industrial processes.

Redlich-Kister polynomial provided a statistically significant mathematical representation of V^E, G^{E*}, Δn, and $\Delta\kappa_S$ data with an optimal number of coefficients and standard deviations comparable to or better than experimental uncertainties.

The composition dependence of thermodynamic excess and deviation properties has been successfully interpreted in terms of molecular interactions between components of the mixture and structural effects.

The application of various models for predicting the refractive indices and sound speeds showed that the considered refractive index models worked well for all investigated systems. In contrast, some speed of sound models did not present good agreement with experimental data.

Nomenclature

ρ – density of the mixture (kg·m^{-3})
c – sound speed of the mixture (m·s^{-1})
n – refractive index of the mixture
η - dynamic viscosity of the mixture (10^{-3} Pa·s)
ρ_j – density of the component i (g·cm^{-3})
c_i – sound speed of the component i (m·s^{-1})
n_i – refractive index of the component i
η_i – dynamic viscosity of the component i (10^{-3} Pa·s)
x_i – mole fraction of component i
φ_i – volume fraction of component i
V^E – excess molar volume (cm^3·mol^{-1})
G^{*E} – excess Gibbs free energy of activation for viscous flow (J·mol^{-1})
$\Delta\kappa_S$ – deviation i isentropic compressibility (10^{12} Pa^{-1})
Δn – deviation in refractive index
ERN – Ernst et al. speed of sound predictive relation
EYK – Eykman refractive index mixing rule
D-G – Dale and Gladstone refractive index mixing rule
JUN – Junjie speed of sound predictive model
L-L – Lorentz-Lorenz refractive index mixing rule
MAPD – Mean Absolute Percentage Deviation
NEW – Newton refractive index mixing rule
NOM – Nomoto speed of sound predictive relation
OST – Oster refractive index mixing rule
VAN – Van Dael speed of sound predictive relation

References:

[1] T. Arbneshi, A. Qerimi, A. Zeqiraj, N. Syla, and F. Rr. Aliaj, " Densities and Sound Speeds of Ternary Mixtures Methyl *tert*-Butyl Ether + Toluene + n -Hexane (or Cyclohexane) and Their Binary Subsystems at a Temperature of 298.15 K and under Ambient Pressure ," *J. Chem. Eng. Data*, 2022, doi: 10.1021/ACS.JCED.2C00093.

[2] F. Aliaj, N. Syla, A. Kurtishaj, Nj. Elezaj, Z. Tolaj, T. Arbneshi, and A. Zeqiraj, "Densities, Refractive Indices, and Derived Properties of Binary Mixtures of Ethanol with Benzene and Pyridine at Various Temperatures Under Atmospheric Pressure," *Int. J. Thermophys.*, 41, 2020.

[3] F. Aliaj, A. Bytyqi-Damoni, and N. Syla, "Density and refractive index study of the ternary system benzene-ethanol-hexane," in *AIP Conference Proceedings*, vol. 1722, 2016.

[4] R. N. Miller, US patent no. 4617105, 1986

[5] S. P. Šerbanović, M. Lj. Kijevčanin, I. R. Radović, and B. D. Djordjević, "Effect of temperature on the excess molar volumes of some alcohol+aromatic mixtures and modelling by cubic EOS mixing rules," *Fluid Phase Equilib.*, 239, 69–82, 2006.

[6] W. Wang, F. Wang, R. Ran, H.J. Park, D.W. Jung, Ch. Kwak, Z. Shao, "Coking suppression in solid oxide fuel cells operating on ethanol by applying pyridine as fuel additive," *J. Power Sources* 265, 20-29, 2014

[7] H.-W. Chen and C.-H. Tu, "Densities, Viscosities, and Refractive Indices for Binary Ternary Mixtures of Acetone, Ethanol, and 2,2,4-Trimethylpentane," *J. Chem. Eng. Data*, 50, 1262–1269, 2005.

[8] K.-J. Han, J.-H. Oh, and S.-J. Park, "Densities and Refractive Indices of the Ternary System Ethyl tert-Butyl Ether (ETBE) + Ethanol + Benzene and its Binary Sub-systems at 298.15 K," *J. Ind. Eng. Chem.*, 13, 360–366, 2007.

[9] G. P. Dubey, M. Sharma, and N. Dubey, "Study of densities, viscosities, and speeds of sound of binary liquid mixtures of butan-1-ol with n-alkanes (C6, C8, and C10) at T = (298.15, 303.15, and 308.15) K," *J. Chem. Thermodyn.*, 40, 2, 309–320, 2008.

[10] H. J. Noh, S. J. Park, and S. J. In, "Excess molar volumes and deviations of refractive indices at 298.15 K for binary and ternary mixtures with pyridine or aniline or quinoline," *J. Ind. Eng. Chem.*, 17, 200–206, 2010.

[11] O. Redlich and A. T. Kister, "Algebraic Representation of Thermodynamic Properties and the Classification of Solutions," *Ind. Eng. Chem.*, 40, 345–348, 1948.

[12] H. A. Lorentz, *The Theory of Electrons and Its Applications to the Phenomena of Light and Radiant Heat, 2nd Ed.* Leipzig: B. G. Teubner, 1916.

[13] J. F. Eykman, "Recherches réfractométriques (suite)," *Recueil des Travaux Chimiques des Pays-Bas*, 14, 185–202, 1895.

[14] G. Oster, "The Scattering of Light and its Applications to Chemistry," C*hem. Rev.*, 43, 319-365, 1948.

[15] T. P. Dale and J. H. Gladstone, "On the influence of temperature on the refraction of light," *Philos. Trans. R. Soc. Lond.*, 148, 887–894, 1858.

[16] W. Heller, "The determination of refractive indices of colloidal particles by means of a new mixture rule or from measurements of light scattering," *Phy. Rev.*, 68, 1945.

[17] W. Heller, "Remarks on refractive index mixture rules," *J. Phys. Chem.*, 69, 1123-1129, 1965.

[18] O. Nomoto, "Empirical Formula for Sound Velocity in Liquid Mixtures," *J. Physical Soc. Japan*, 13, 1528–1532, 1958.

[19] W. van Dael, "Thermodynamic Properties and the Velocity of Sound," in *Experimental Thermodynamics Volume II*, Boston, MA: Springer, 1968.

[20] S. Ernst, J. Glinski, and Jezowska-Trzebiatowska, "Dependence of the ultrasound velocity on association of liquids," *Acta Phys. Pol. A*, 55, 501–516, 1979.

[21] Z. Junjie, *J. Univ. Sci. Technol. China*, 14, p. 298, 1984.

[22] M. R. Rao, "Velocity of Sound in Liquids and Chemical Constitution," *J. Chem. Phys.*, 9, 682–685, 1941.

[23] P. R. Garrett and J. M. Pollock, "Thermodynamic properties of mixtures of benzene with pyridines 4. Excess volumes of benzene and toluene with pyridine and the methyl pyridines," *J. Chem. Thermodyn.*, 9, 1045–1049, 1977.

[24] R. Gonzalez-Olmos, M. Iglesias, and S. Mattedi, "Influence of temperature on thermodynamics of ethanol + hydrocarbon gasoline additives," *Phys. Chem. Liquids*, 48, 337-384, 2010.

[25] T. J. Findlay and J. L. Copp, "Thermodynamics of binary systems containing amines. Part 5.—Alcohols and pyridine," *Trans. Faraday Soc.*, 65, 1463–1469, 1969.

[26] A. Borun, M. Zurada, and A. Bald, "Densities and excess molar volumes for mixtures of methanol with other alcohols at temperatures (288.15–313.15 K)," *J. Therm. Anal. Calorim.*, 100, 707–715, 2010.

[27] A. Blanco, A. García-Abuín, D. Gómez-Díaz, and J. M. Navaza, "Density, Speed of Sound, Viscosity, Refractive Index, and Excess Volume of N-Methyl-2-pyrrolidone (NMP) + Water + Ethanol from T = (293.15 to 323.15) K," *J. Chem. Eng. Data*, 57, 1009–1014, 2012.

[28] M. S. Bakshi and G. Kaur, "Thermodynamic Behavior of Mixtures. 4. Mixtures of Methanol with Pyridine and N, N-Dimethylformamide at 25 °C," *J. Chem. Eng. Data*, 42, 298–300, 1997.

[29] M. Tjahjono and M. Garland, "On the determination of partial molar volumes, partial molar refractions, mean electronic polarizabilities and effective molecular radii from dilute multi-component data alone using response surface models," *J. Solution Chem.*, 36, 221-236, 2007.

[30] D. R Lide, *CRC Handbook of Chemistry and Physics*, 84th Ed., Boca Raton: CRC Press, 2003.

[31] J. A. Al-Kandary, A. S. Al-Jimaz, and A.-H. M. Abdul-Latif, "Viscosities, Densities, and Speeds of Sound of Binary Mixtures of Benzene, Toluene, o-Xylene, m-Xylene, p-Xylene, and Mesitylene with Anisole at (288.15, 293.15, 298.15, and 303.15) K," *J. Chem. Eng. Data*, 51, 2074–2082, 2006.

[32] B. González, A. Domínguez, and J. Tojo, "Dynamic Viscosities, Densities, and Speed of Sound and Derived Properties of the Binary Systems Acetic Acid with Water, Methanol, Ethanol, Ethyl Acetate and Methyl Acetate at T = (293.15, 298.15, and 303.15) K at Atmospheric Pressure," *J. Chem. Eng. Data*, 49, 1590–1596, 2004.

[33] M. E. Wieser et al., "Atomic weights of the elements 2011 (IUPAC Technical Reports)," *Pure Appl. Chem.*, 85, 1047–1078, 2013.

[34] B. N. Taylor and C. E. Kuyatt, "NIST Technical Note 1297 1994 Edition, Guidelines for Evaluating and Expressing the Uncertainty of NIST Measurement Results," *National Institute of Standards and Technology*, 1994.

[35] F. Aliaj, A. Gjevori, N. Syla, N. Elezaj, B. Ziberi, and B. Dalipi, "Physical Properties of the Binary Mixtures of Ethanol + Benzene and Ethanol + Pyridine at Five Temperatures under Atmospheric Pressure," *Acta Phys. Pol. A*, 137, 465–472, 2020.

[36] P. P. Singh, B. R. Sharma, and P. C. Chopra, "Excess volumes of (pyridine+an n-alkanol) and (α-picoline+an n-alkanol)," *J. Chem. Thermodyn.*, 12, 1193–1194, 1980.

[37] S. Kouris and C. Panayiotou, "Dynamic viscosity of mixtures of benzene, ethanol, and n-heptane at 298.15 K," *J. Chem. Eng. Data*, 34, 200–203, 1989.

[38] A. Ali, M. Tariq, F. Nabi, and Shahjahan, "Density, Viscosity, Refractive Index, and Speed of Sound in Binary Mixtures of Pyridine and 1-Alkanols (C6 , C7 , C8 , C10) at 303.15 K," *Chin. J. Chem.*, 26, 2009–2015, 2008.

[39] M. L. Kijevčanin, E. M. Živković, B. D. Djordjević, I. R. Radović, J. Jovanović, and S. P. Šerbanović, "Experimental determination and modeling of excess molar volumes, viscosities and refractive indices of the binary systems (pyridine+1-propanol, +1,2-propanediol, +1,3-propanediol, and +glycerol). New UNIFAC-VISCO parameters determination," *J. Chem. Thermodyn.*, 56, 49–56, 2013.

[40] R. J. Fort and W. R. Moore, "Viscosities of binary liquid mixtures," *Trans. Faraday Soc.*, 62, 1112-1119, 1966.

[41] S. Oswal and M. v. Rathnam, "Viscosity data of binary mixtures: ethyl acetate + cyclohexane, + benzene, + toluene, + ethylbenzene + carbon tetrachloride, and + chloroform at 303.15 K," *Can. J. Chem.*, 62, 2851–2853, 1984.

[42] B. García, R. Alcalde, S. Aparicio, and J. M. Leal, "The N-methylpyrrolidone–(C1–C10) alkan-1-ols solvent systems," *Phys. Chem. Chem. Phys.*, 4, 1170–1177, 2002.

[43] P. Brocos, Á. Piñeiro, R. Bravo, and A. Amigo, "Refractive indices, molar volumes and molar refractions of binary liquid mixtures: concepts and correlations," *Phys. Chem. Chem. Phys.*, 5, 550–557, 2003.

[44] P. R. Bevington, D. K. Robinson, *Data Reduction and Error Analysis for the Physical Sciences*, 3rd Ed. New York: McGraw-Hill, 2003.

[45] J. E. Hanke and D. Wichern, *Business Forecasting*, 9th Ed. Essex: Pearson, 2014.

[46] R. Mehra, "Application of refractive index mixing rules in binary systems of hexadecane and heptadecane with n-alkanols at different temperatures," *Proceedings of the Indian Acad. Sci.: Chemical Sciences*, 115, 147-154, 2003.